A COMPUTATIONAL INVESTIGATION INTO THE THIRD-ORDER NONLINEAR OPTICAL PROPERTIES OF CYANINE-LIKE POLYMETHINES FOR ALL-OPTICAL SWITCHING APPLICATIONS

A Dissertation
Presented to
The Academic Faculty

by

Stephen B. Shiring

In Partial Fulfillment
of the Requirements for the Degree
Doctor of Philosophy in the
School of Chemistry and Biochemistry

Georgia Institute of Technology
August 2017

A COMPUTATIONAL INVESTIGATION INTO THE THIRD-ORDER NONLINEAR OPTICAL PROPERTIES OF CYANINE-LIKE POLYMETHINES FOR ALL-OPTICAL SWITCHING APPLICATIONS

Approved by:

Dr. Jean-Luc Brédas, Advisor
School of Chemistry and Biochemistry
Georgia Institute of Technology

Dr. Joseph W. Perry
School of Chemistry and Biochemistry
Georgia Institute of Technology

Dr. C. David Sherrill
School of Chemistry and Biochemistry
Georgia Institute of Technology

Dr. Bernard Kippelen
School of Electrical and Computer Engineering
Georgia Institute of Technology

Dr. Seth R. Marder
School of Chemistry and Biochemistry
Georgia Institute of Technology

Date Approved: May 15, 2017

To my parents
for always supporting me in my endeavors
and providing me with the skills to succeed.

ACKNOWLEDGEMENTS

I have been fortunate to have been surrounded by many distinguished academics during my graduate career who helped me to grow and to learn as a scientist. Chief among those is my advisor, Professor Jean-Luc Brédas; I am in sincere gratitude to him for permitting me to join his research group and for his continual support and encouragement at every step of the way, no matter what part of the globe we were in. My undergraduate professors said to be prepared for anything in graduate school, but I never anticipated having the opportunity to study at a university in and experience a culture as exotic as in Saudi Arabia.

I would like to thank my committee members. To Professor C. David Sherrill, for his encouragement and willingness to become somewhat of a quasi-advisor. To Professor Seth Marder, for his support, guidance, and insightful questions and discussions. And to Professors Joseph Perry and Bernard Kippelen, for their continual support and advice. I am also indebted to the experimentalists I was able to collaborate with: Dr. Steve Barlow, Dr. Iryna Davydenko, Dr. San-Hui Chi, and Dr. Bilal Kaafarani.

I would also like to thank Brédators past and present for their friendship and willingness to share their scientific knowledge and assistance. To Dr. Paul Winget, for teaching me the finer art of computational chemistry, his support in my work and ideas, and for his technical support. To Professor Chad Risko, for stressing clarity and simplicity in my scientific writing and to always having an open ear for discussing science and life issues. To Dr. Gjergji Sini for always having helpful comments and for many interesting conversations. To Dr. Veaceslav Coropceanu, for sharing with me how to approach a problem and his continual support. And especially to Dr. Rebecca Gieseking, to whom I am very grateful

for her guidance and help, for being an inspiring role model, and continuing to share her scientific knowledge.

I will cherish the many strong friendships developed here at Tech, which made the past five years enjoyable, adventurous, and bearable: Mathew and Kali Cooper, Rylan Wolfe, Dr. Hailey Bureau, Aida Demissie, Aaron McKee, Smitha Janardan, Dr. Alex Hyla, Brandon Bakr, and Jen Beveridge (who would have thought that nearly 10 years after that first day of the first HC class we would be here?). And to those friends who were trailblazers to KAUST and made it a welcoming place: Dr. Sean Ryno and his family, Dr. Khanh Do, and Dr. Mahesh Kumar Ravva.

I would like to express my deepest gratitude to my family, particularly my parents Stephen and Tamara, and my sisters, Samantha and Elizabeth, for their continual love, support, and encouragement to always achieve my fullest potential. To my uncle Tony Valasek, for many good conversations, and my aunt Barbara Valasek, for the many adventures in Atlanta. To my friends back home, who are always willing to make time to see each other when we are all back in town. To the Kellermans (BK, Sherry, and Dakota), for making Georgia feel like a home and always offering an escape from Atlanta. And to Ashleigh, for always being there (even when separated by an ocean and a sea) and making me smile; love you LA!

And finally to Excalibur, Bernadette, Fred, and Oliver: for showing me that you never pass up a treat or snack, no matter what.

TABLE OF CONTENTS

LIST OF TABLES

LIST OF FIGURES

LIST OF SYMBOLS AND ABBREVIATIONS

AOS	All-Optical Switching
BLA	Bond Length Alternation
BOA	Bond Order Alternation
CI	Configuration Interaction
CT	Charge Transfer
DFT	Density Functional Theory
FOM	Figure of Merit (of a material for use in an AOS device)
GGA	Generalized Gradient Approach
HF	Hartree-Fock
HOMO	Highest Occupied Molecular Orbital
Im	Imaginary
INDO	Intermediate Neglect of Differential Overlap
MD	Molecular Dynamics
LDA	Local Density Approximation
LUMO	Lowest Unoccupied Molecular Orbital
MD	Molecular Dynamics
MO	Molecular Orbital
MRDCI	Multi-Reference Determinant Configuration Interaction
NBO	Natural Bond Order
NLO	Nonlinear Optics/Optical
NTO	Natural Transition Orbital
OPA	One-Photon Absorption
Re	Real
SCF	Self-Consistent Field
SAC-CI	Symmetry Adapted Cluster-Configuration Interaction
SAPT	Symmetry Adapted Perturbation Theory
SCI	Singles Configuration Interaction
SDCI	Singles-Doubles Configuration Interaction
SOS	Sum-Over-States
TD-DFT	Time-Dependent DFT
TPA	Two-Photon Absorption
ZINDO	Zerner's Intermediate Neglect of Differential Overlap

SUMMARY

Cyanine-like polymethines have recently attracted renewed attention for their potential as materials to realize all-optical switching applications by demonstrating large real and small imaginary parts of the third-order polarizability at telecommunications wavelengths. In this dissertation, we employ a variety of computational methodologies to investigate the structure-property relationships of promising cyanine-like polymethines. We begin with an overview of the field of nonlinear optics and place cyanine-like polymethines within that context before discussing the remaining challenges confronting their use in all-optical switching devices. We then briefly review the electronic-structure and molecular-dynamics methods used throughout this work.

We communicate the main results of this dissertation in Chapters 3 – 6. Chapter 3 focuses on how the interplay between cyanine and counterion steric bulk affects their packing in the bulk. In Chapter 4, we investigate the evolution of the non-covalent interactions between a streptocyanine and counterion as a function of counterion position along the cyanine backbone. Zwitterionic cyanines designed to eliminate the need of an untethered counterion are the focus of Chapter 5, in which we provide design principles. We study the origin of the third-order polarizability of mixed-stack binary charger transfer complexes in Chapter 6. We conclude in Chapter 7 with a synopsis and a look towards future directions.

CHAPTER 1

INTRODUCTION

1.1. The Case for All-Optical Switching

The Internet has, without a doubt, revolutionized the way that society communicates, obtains information, conducts business, and consumes media. A report compiled by Sandvine, a network policy control company, showed that in 2016 the average North American household had over seven Internet-connected devices active each day, and that the predominant use of these devices is to stream real-time entertainment from online providers such as Netflix.[1] This rapid integration and usage of Internet-connected devices into everyday life has led to an increase in the demand for data transmission, with estimates approaching a staggering 194 exabytes per month of global Internet traffic by 2020, nearly 80% of which will be video-based traffic.[2] It is anticipated that next-generation transmission devices will need to operate at speeds of one order of magnitude faster than current opto-electrical switches in order to meet this expected demand.[3-4]

In current switching devices, optical signals transmitted over optical fibers must be converted from the optical domain to the electrical domain for processing and then converted back to the optical domain for transmission, a process that is costly in terms of both time and energy consumption.[5-7] This conversion step can be eliminated by performing the processing entirely in the optical domain with an all-optical switching (AOS) device. An AOS device, in which one optical beam is modulated by a second optical beam, has the potential to realize the required order-of-magnitude higher switching speeds,

exceeding 1 terabit/s.[8-10] An example of an AOS device is a Mach-Zehnder interferometer, in which the device splits an input signal into two arms and exploits the difference in path lengths to recombine the signal either in phase or out of phase at the end of the device. Instead of relying on a difference between physical path lengths, a third-order nonlinear optical (NLO) material can be incorporated into arms of equal path length as shown in Figure 1.1. When a control signal is introduced to one arm, the refractive index of the NLO material is changed, resulting in a difference in input signal speed propagation between the two arms. For a difference in speed which results in a phase difference of π between each arm, the input signals recombine destructively. The signals recombine constructively when there is no control signal, as the path lengths of both arms are identical.

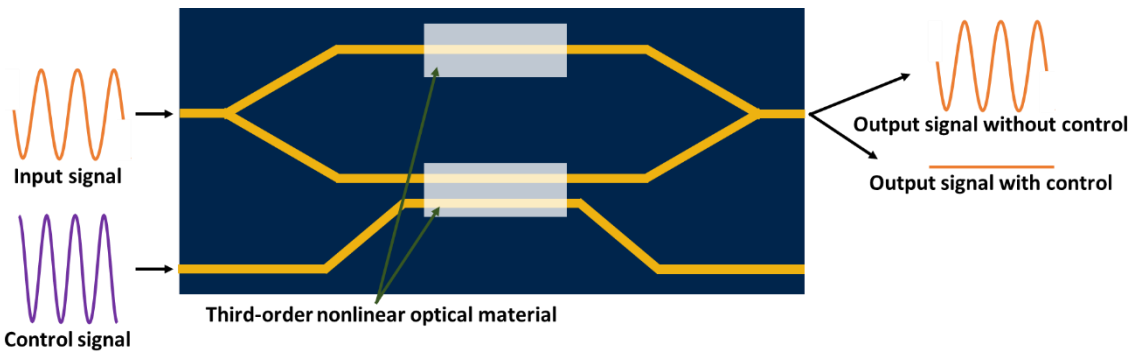

Figure 1.1: Cartoon of a Mach-Zehnder interferometer demonstrating AOS using a third-order nonlinear optical material. Adapted from Hales *et al.*[27] and Gieseking *et al.*[48]

The nonlinear refractive index of a material depends on its third-order electrical susceptibility ($\chi^{(3)}$) that, in an organic molecular semiconductor, is directly related to the molecular third-order polarizability, γ. Upon application of an intense light source, the real part of the third-order polarizability ($\mathrm{Re}(\gamma)$) determines the change in refractive index,

while the imaginary part ($\mathrm{Im}(\gamma)$) defines the two-photon absorption cross-section.[11-12] A material must satisfy a number of requirements to be suitable for use in an AOS device, including a large magnitude of $\mathrm{Re}(\gamma)$ and minimal optical losses due to one-photon absorption (OPA) and two-photon absorption (TPA).[13] These requirements lead to defining a figure-of-merit (FOM) based on the ratio $|\mathrm{Re}(\gamma)|/\mathrm{Im}(\gamma)$, which for a suitable material must exceed *ca.* 12 at telecommunications wavelengths (1300 – 1550 nm).[14-15]

1.2. The Molecular Third-Order Polarizability

The application of an external electric field $\vec{F}(\omega)$ to a molecule induces a displacement of electron density from the nuclei and creates an induced dipole moment, $\vec{\mu}^{ind}(\omega)$. Under the electric-dipole approximation (*i.e.*, the magnetic component of an electromagnetic field is neglected), the total molecular polarization can be written as:

$$\vec{\mu} = \vec{\mu}_0 + \vec{\mu}^{ind}(\omega) \tag{1.1}$$

where $\vec{\mu}_0$ is the permanent molecular dipole moment (defined here as the ground-state dipole moment, $\vec{\mu}_g$) in the absence of an electric field and ω is the frequency of the applied electric field. $\vec{\mu}^{ind}(\omega)$ can be expressed using a Taylor series expansion as:

$$\begin{aligned}\vec{\mu}^{ind}(\omega) = \frac{1}{1!}\alpha_{ij}(\omega)\cdot\vec{F_j}(\omega) + \frac{1}{2!}\beta_{ijk}\cdot\vec{F_j}(\omega)\cdot\overrightarrow{F_k}(\omega) \\ + \frac{1}{3!}\gamma_{ijkl}\cdot\vec{F_j}(\omega)\cdot\overrightarrow{F_k}(\omega)\cdot\vec{F_l}(\omega) + \cdots\end{aligned} \tag{1.2}$$

where the subscripts i, j, k, and l denote the molecular fixed axes (*x*, *y*, or *z*); α_{ij}, β_{ijk}, and γ_{ijkl} are the first-order (linear), second-order, and third-order polarizabilities, respectively;

and $\vec{F_j}(\omega)$ is the j^{th} component of the electric field. We note that the n^{th} polarizability is a tensor of rank (n+1); γ_{ijkl} is thus a fourth-rank tensor with 81 components.

There are many different methods available to theoretically calculate the molecular polarizabilities, such as the finite-field method, coupled oscillator technique, or sum-over-states (SOS) approach.[16-18] The SOS approach is an attractive method to use because it allows one to gain chemical insight into the molecular structure and NLO response, and because of this it will be employed within this Thesis.[19] The SOS expressions allow one to assess which electronic excited states are important to the NLO response through an understanding of the ground-state and lowest several excited-state energies, transition dipole moments, and state dipole moments. The SOS expression for γ_{ijkl}, which derived from perturbation theory, relates a perturbation on the order of n+1 in the electric field to the molecular polarizability on the order n, is:

$$
\begin{aligned}
&\gamma_{ijkl}(\omega_p;\omega_q,\omega_r,\omega_s)\\
&=\frac{1}{\hbar^3}\sum P_{123}\\
&\times\left\{\sum_{x,y,z}{}'\left(\frac{\mu_{gx}^{i}\bar{\mu}_{xy}^{j}\bar{\mu}_{yz}^{k}\mu_{zg}^{l}}{(\omega_{gx}-i\Gamma_{gx}-\omega_p)(\omega_{gy}-i\Gamma_{gy}-\omega_r-\omega_s)(\omega_{gz}-i\Gamma_{gz}-\omega_s)}\right.\right.\\
&+\frac{\mu_{gx}^{j}\bar{\mu}_{xy}^{i}\bar{\mu}_{yz}^{k}\mu_{zg}^{l}}{(\omega_{gx}+i\Gamma_{gx}+\omega_q)(\omega_{gy}-i\Gamma_{gy}-\omega_r-\omega_s)(\omega_{gz}-i\Gamma_{gz}-\omega_s)}\\
&+\frac{\mu_{gx}^{j}\bar{\mu}_{xy}^{k}\bar{\mu}_{yz}^{i}\mu_{zg}^{l}}{(\omega_{gx}+i\Gamma_{gx}+\omega_q)(\omega_{gy}+i\Gamma_{gy}+\omega_q+\omega_r)(\omega_{gz}-i\Gamma_{gz}-\omega_s)}\\
&\left.+\frac{\mu_{gx}^{j}\bar{\mu}_{xy}^{k}\bar{\mu}_{yz}^{l}\mu_{zg}^{i}}{(\omega_{gx}+i\Gamma_{gx}+\omega_q)(\omega_{gy}+i\Gamma_{gy}+\omega_q+\omega_r)(\omega_{gz}+i\Gamma_{gz}+\omega_p)}\right)\\
&-\sum_{x,y}{}'\left(\frac{\mu_{gx}^{i}\mu_{xg}^{j}\mu_{gy}^{k}\mu_{yg}^{l}}{(\omega_{gx}-i\Gamma_{gx}-\omega_p)(\omega_{gx}-i\Gamma_{gx}-\omega_q)(\omega_{gy}-i\Gamma_{gy}-\omega_s)}\right.\\
&+\frac{\mu_{gx}^{i}\mu_{xg}^{j}\mu_{gy}^{k}\mu_{yg}^{l}}{(\omega_{gx}-i\Gamma_{gx}-\omega_q)(\omega_{gy}+i\Gamma_{gy}+\omega_r)(\omega_{gy}-i\Gamma_{gy}-\omega_s)}\\
&+\frac{\mu_{gx}^{j}\mu_{xg}^{i}\mu_{gy}^{k}\mu_{yg}^{l}}{(\omega_{gx}+i\Gamma_{gx}+\omega_q)(\omega_{gx}+i\Gamma_{gx}+\omega_p)(\omega_{gy}+i\Gamma_{gy}+\omega_r)}\\
&\left.\left.+\frac{\mu_{gx}^{j}\mu_{xg}^{i}\mu_{gy}^{k}\mu_{yg}^{l}}{(\omega_{gx}+i\Gamma_{gx}+\omega_q)(\omega_{gy}+i\Gamma_{gy}+\omega_r)(\omega_{gy}-i\Gamma_{gy}-\omega_s)}\right)\right\}
\end{aligned}
\tag{1.3}
$$

where g denotes the electronic ground state and x, y, and z denote excited states; μ_{gx} is the transition dipole moment between states g and x; $\bar{\mu}_{gx}$ is the difference between the state dipole moments of state x and the ground state when x and y are equal; and $\hbar\omega_{gx}$ is the transition energy from state g to state x, with Γ_{gy} representing the damping factor (related to the lifetime) of excited state x. The permutation operator $\sum P_{123}$ sums over the terms

obtained by simultaneous permutation of the incident photon frequency and dipole moment operator. The electric-field frequencies are denoted by the terms ω_p, ω_q, ω_r, ω_s.

Equation 1.3 can be simplified to an essential-state model by making three reasonable assumptions: first, that a single excited state *e* is significantly dipole-coupled to the ground state *g*; second, that this excited state is only strongly coupled to a few higher-lying excited states e'; and third, that the molecular polarizability is dominated by the response along the long axis *j* (given the elongated nature of the relevant molecules).[20-23] This simplified equation is commonly referred to as the "three-term model" and writes:

$$\gamma_{jjjj}(\omega;\omega,-\omega,\omega) \propto \frac{\mu_{ge}^2 \Delta\mu_{eg}^2}{\left(E_{ge}-\hbar\omega-i\Gamma_{ge}\right)^2\left(E_{ge}-2\hbar\omega-i\Gamma_{ge}\right)} + \sum_{e'} \frac{\mu_{ge}^2 \mu_{ee'}^2}{\left(E_{ge}-\hbar\omega-i\Gamma_{ge}\right)^2\left(E_{ge'}-2\hbar\omega-i\Gamma_{ge'}\right)} - \frac{\mu_{ge}^4}{\left(E_{ge}-\hbar\omega-i\Gamma_{ge}\right)^3} \quad (1.4)$$

where $\Delta\mu_{eg}$ is the difference between state dipole moments of states g and e, and E_{ge} and $E_{ge'}$ are the OPA and TPA excited-state energies from the ground state, respectively. The first term is generally referred to as the dipolar term **D**, present only in noncentrosymmetric materials. The second term is referred to as the two-photon term **T**, as it also involves the transition dipole moment between states e and e'. The last term is referred to as the negative term **N**, as it provides a negative contribution to γ. This equation is useful for qualitatively discussing how changes in molecular properties impact γ. We note that in equation 1.4 we have set the frequencies of the applied electric fields to reflect those which gives rise to the

nonlinear refractive index and TPA, which as stated earlier depend on the real and imaginary components of $\gamma_{jjjj}(\omega;\omega,-\omega,\omega)$ and enable AOS.[15, 24] The **D** and **T** terms contribute to the TPA cross-section, δ_{TPA}, with two-photon resonances ($2\hbar\omega$) appearing in their denominators.

1.3. Third-Order Nonlinear Optical Response of Organic π-Conjugated Molecules

The third-order NLO responses of many π-conjugated organic materials have been investigated since the 1980s; however, most of these materials to date have generally unacceptably small FOMs for AOS at telecommunications wavelengths, in particular due to large TPA.[25-27] An exception has been found in the case of cyanine-like polymethines, which have been recently shown to possess the potential to realize the required FOM for AOS applications.[26, 28]

Polymethines are composed of a backbone consisting of methine (*i.e.*, sp^2-hybridized CH) groups, and include polyenes (neutral structures with an even number of methine units) and cyanine-like systems (charged structures with an odd number of methine units). Symmetrical (short) cyanine-like polymethine backbones are capped with two identical donor or acceptor moieties and possess C_{2V} symmetry. In studies relating the geometric structure of linear organic π-conjugated molecules to their NLO response, a relevant parameter to consider is the degree of bond-length alternation (BLA).[28-31] BLA can be defined as the difference in bond lengths between adjacent C-C bonds along the backbone,[32] or as the average of the absolute differences in the lengths of successive bonds over the entire length of the backbone.[30] The BLA in polyenes, whose backbones consist

of alternating double and single bonds, is of a significant degree at ~ 0.10 Å.[33-34] For cyanines with short backbone lengths, the charge can delocalize over the whole backbone, which leads to a small degree of BLA approaching 0.[30, 35]

The differences between the geometric structures of polyenes and cyanine-like polymethines ultimately arise from the differences in their electronic structures. In both classes of molecules, the highest occupied molecular orbital (HOMO) and the lowest unoccupied molecular orbital (LUMO) are formed from the p_z atomic orbitals contributed by each carbon atom. Figure 1.2 shows the Hückel molecular orbitals of the HOMO and LUMO and relative energies for model π-conjugated compounds of a neutral polyene (butadiene) and a charged cyanine-like polymethine (a three-carbon streptocyanine). We note that streptocyanines, cyanine-like polymethines containing amino end groups, have been used in a variety of NLO studies as prototypical cyanine molecules.[35-39]

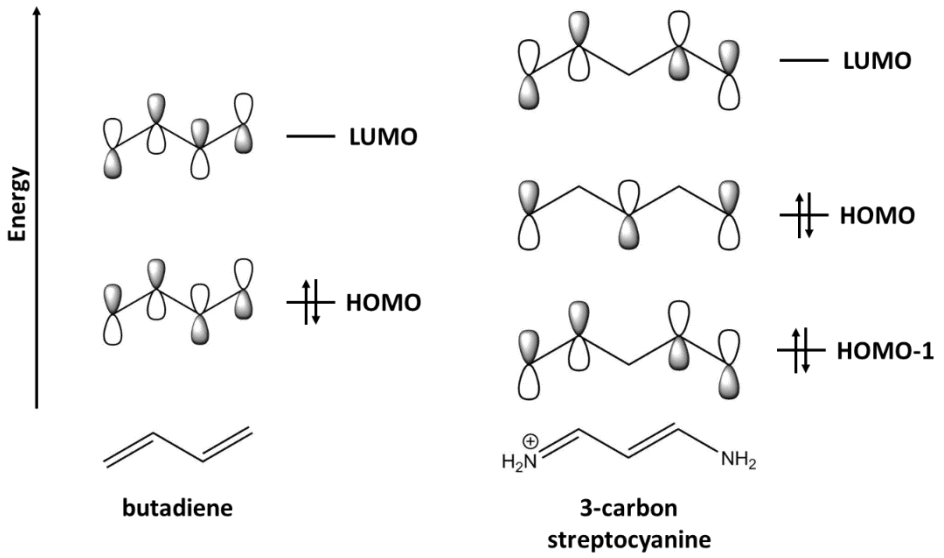

Figure 1.2: Hückel molecular orbitals and relative energies for butadiene (left) and 3-carbon streptocyanine (right). We note that the HOMO of the streptocyanine is non-bonding.

In the case of butadiene (Figure 1.2, left), nodes appear between the carbon atoms on bonds, implying that there is a non-zero probability for finding each π-electron near each carbon atom. The HOMO of butadiene, with its one node, is bonding across nominally double bonds and antibonding across nominally single bonds, while the LUMO, with its two nodes, is reversed. This bonding and anti-bonding character results in the appearance of non-zero BLA for polyene-like molecules, with a net atomic charges on the carbon atoms near zero.[40] For cyanine-like molecules, on the other hand, the frontier MOs are localized on alternate carbon atoms, with nodes present on both carbon atoms and bonds. The HOMO in the streptocyanine (Figure 1.2, right) has nodes on alternate carbon atoms, resulting in a non-bonding MO which appears between the bonding and anti-bonding MOs. Since the HOMO is localized on alternate atoms, there is a significant degree of charge

alternation and each bond has a similar degree of bonding and anti-bonding character; the latter leads to the negligibly small BLA in cyanine-like systems.

The third-order nonlinear optical response of linear π-conjugated organic molecules has been well-established to depend on the degree of BLA.[25, 28-30, 41] We note that BOA, the bond order alternation, is also often correlated to γ. Although BOA is a better overall indicator of electronic structure, and hence of the nonlinear properties, BLA (which reflects the geometric structure) is correlated to BOA (and thus to the electronic structure) when the molecule is in its equilibrium ground-state geometry.[42]

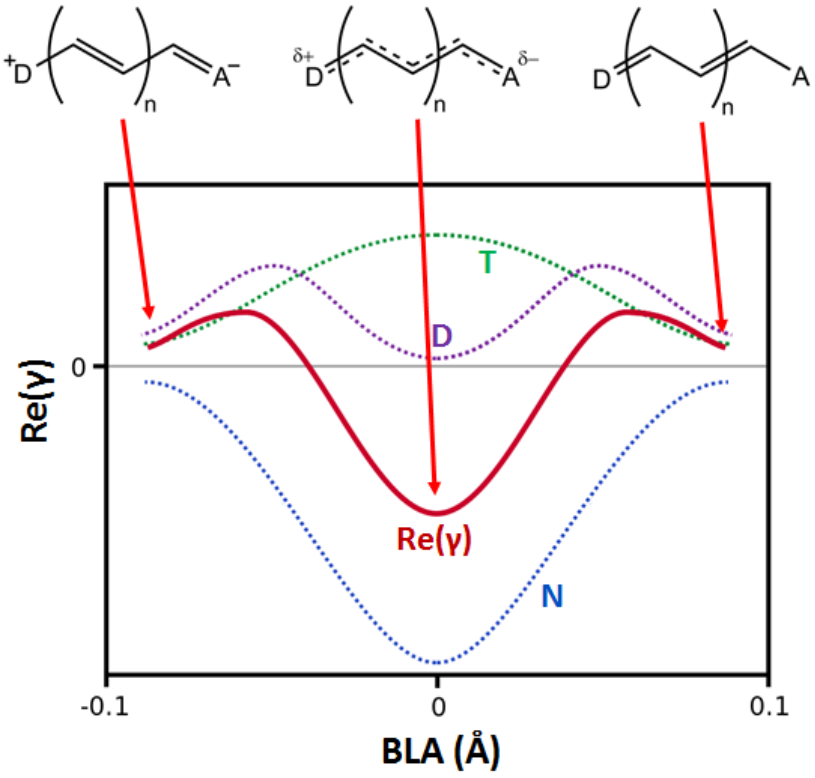

Figure 1.3: Evolution of Re(γ) and the contribution of each term from the three-term model as a function of BLA.[30]

We will discuss the relationship between BLA and γ by considering all molecules to be at their energetic minimum. Figure 1.3 shows the evolution of γ as a function of BLA.[30] The absolute magnitude of γ can be seen to reach a maximum in magnitude at three regimes, depending on the extent of ground-state polarization. At the polyene limit (BLA ~ 0.1 Å) and zwitterion limit (BLA ~ -0.1 Å), γ is small and positive. It reaches a positive maximum at two positions when the BLA is between the cyanine and polyene/zwitterion limits (at BLA ~ +/- 0.06 Å). γ is negative and attains its largest magnitude at the so-called "cyanine limit," when BLA ~ 0 Å. A number of means are available to tune the extent of ground-state polarization and BLA from the polyene-limit through the cyanine-limit to the zwitterion-limit, including adjusting the strength of the donor and/or acceptor end groups, applying an electric field parallel to the backbone, and changing the surrounding medium. Thus, among the structures considered here, cyanine-like polymethines inherently have a large, negative, γ.

Cyanines possess an additional critical advantage over other π-conjugated materials, such as polyenes, which makes their use in AOS applications especially promising.[15] In polyenes, by extension of the butadiene Hückel frontier MOs, a HOMO→LUMO electronic transition reverses the bonding and anti-bonding character across the adjacent carbon atoms, leading the equilibrium geometry of the excited state to be markedly different than that of the ground state. Consequently, this excitation will show a broad absorption band because of vibronic broadening. Furthermore in polyenes, the lowest OPA and TPA excited states are energetically close together, with the next higher excited states similarly spaced together (Figure 1.4, left). As a result, a large detuning factor Δ (*i.e.*, the energy difference between the incoming photon energy and the lowest OPA state) of more

than half the energy of the one-photon excited state is necessary to prevent unacceptable losses due to TPA. Since the optical signal is far from resonance, Re(γ) is usually rather small due to limited pre-resonant enhancement.

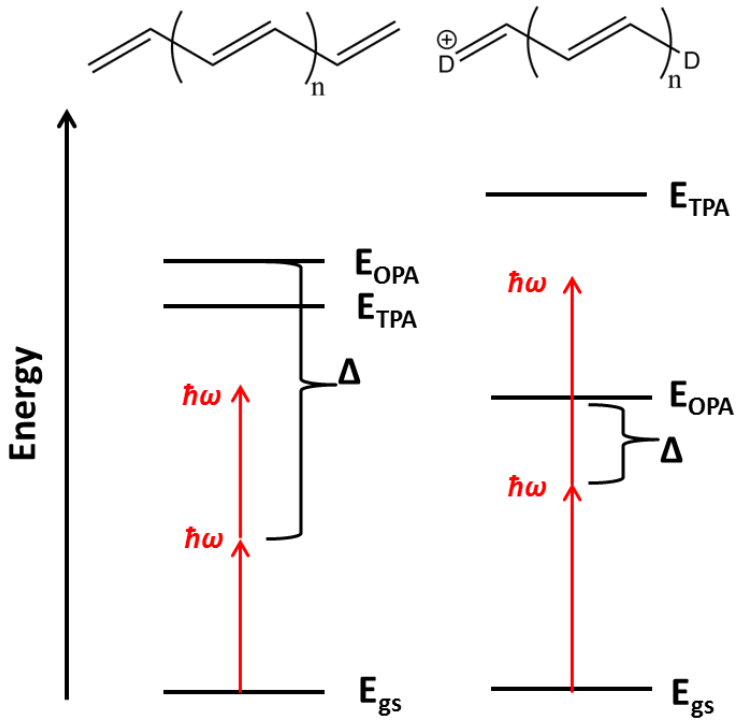

Figure 1.4: Illustration of the molecular geometry and typical excited state spacing in polyenes (left) and cyanines (right). E_{gs} denotes the ground state. Δ is the detuning between the energy of the incoming optical signal (ħω) and the energy of the OPA state. Adapted from Hales *et al.*[15]

The excited states in cyanine-like polymethines, such as streptocyanines, present a strikingly different situation. In these molecules, a HOMO→LUMO excitation primarily shifts the electron density from the even-numbered carbon atoms to the odd-numbered carbon atoms, leaving the bonding and anti-bonding character largely unaffected. The equilibrium geometries of the ground state and the excited state are thus very similar, and

the excitation is very sharp and narrow with a large transition dipole moment, μ_{ge}. Because of differences in orbital energetic spacing, the energy of the OPA state in cyanine-like polymethines is smaller than the energy of the OPA state in polyenes of similar length (Figure 1.2). In cyanine-like polymethines, the lowest TPA excited state is separated from the ground state by nearly twice the energy of the OPA state, affording a large energetic window between them.[15, 43-47] This window allows tuning of the optical signal frequency closer to the OPA state without suffering large optical losses due to TPA, as 2ħω will fall within this energetic window. Subsequently, the small detuning factor between the optical signal and the lowest OPA state enhances Re(γ) through pre-resonant enhancement.

We can now understand the inherently large γ of cyanine-like polymethines as arising from its favorable excited-state properties.[48] Possessing a comparatively large μ_{ge} and small E_{OPA} is advantageous for promoting a large magnitude of γ. Recalling the simplified three-term model (equation 1.4), we can see that each term in the expression depends on excited-state energies and transition dipole moments (either from the ground state to the OPA state for the **D** and **N** terms or additionally from the OPA state to TPA states in the case of the **T** term). A small E_{OPA} leads to smaller denominators, while a large μ_{ge} promotes a large numerator. In cyanine-like polymethines with C_{2v} symmetry at the cyanine-limit, the changes between state dipole moments are negligibly small; subsequently, the **D** term, which depends on $\Delta\mu_{ge}^2$, is negligibly small. As E_{TPA} is nearly twice the energy of E_{OPA}, and owing to the fact that $\mu_{ee'}$ is small in cyanines,[15, 81-82] the **T** term (which depends on μ_{ge} and $\mu_{ee'}$) is much smaller than the **N** term (which depends only on μ_{ge}^4). Thus, in cyanine-like polymethines, the **N** term dominates and is responsible for the sign and magnitude of γ. In polyenes with C_{2h} symmetry, the **D** term is likewise negligible, but the

T term is slightly greater than the **N** term because E_{TPA} is close in energy to E_{OPA} and possesses a non-negligible excited-state transition dipole moment; this leads to γ being small and positive at the polyene limit.

1.4. Challenges Confronting Cyanine-like Polymethines

It is clear from the discussion above that isolated cyanine-like polymethines possess very promising molecular-level properties and are uniquely suited as materials to potentially realize AOS. Indeed, selenopyrylium cyanines have been shown to exceed the required FOM in dilute solutions, and thin films of thiopyrylium cyanines have likewise met or exceeded the FOM in thin films.[49] There are many end groups available for substitution at the ends of the cyanine backbone, and cyanine properties can be further tuned by increasing the conjugation length by either extending the length of the backbone or through delocalization into the end groups, and/or chemical substitution at the end groups and/or along the backbone.[27, 50]

However, translating these promising molecular properties into useful materials with the large chromophore concentrations required for functional devices at the macroscale has proved challenging. While the electronic structure of cyanine-like polymethines confers on this class of molecules a highly polarizable nature (and thus large magnitudes of Re(γ)), it also leads to strong intermolecular interactions. Intermolecular interactions between chromophores at increased chromophore concentration and interactions between the chromophore and its environment can cause pronounced unfavorable changes to their linear and nonlinear optical properties of interest for AOS.[51-54] Significant efforts have been

directed towards understanding and minimizing interactions between chromophores in thin films and interactions between chromophores and their environment.

We recall that in a thin film or in solution, the charge of a cyanine unit must be balanced by the presence of a counterion. Environmental effects and cyanine-counterion interactions can induce geometric changes in the backbone which negatively impact NLO properties. The presence of the counterion can lead to ion-pairing, where the counterion and backbone charge tend to localize towards one end of the cyanine and induce symmetry breaking, which results in a molecular structure with large BLA.[36, 55-57] Symmetry-broken molecules lose their advantageous cyanine-like character, incurring substantial TPA, elimination of the OPA-TPA energetic window, and a reduction in $|\mathrm{Re}(\gamma)|$.[30, 36] Small and strongly polarizing counterions such as halides potentially lead to strong ion-pairing and symmetry breaking, if they overcome the ability of the dielectric medium to screen the charges.[55] Thus, it is critical to minimize the counterion's ion-pairing effect and subsequent symmetry-breaking in order to preserve the molecular NLO properties of cyanines and to realize materials suitable for AOS applications.

Cyanine-like polymethines are also prone to aggregate even at fairly low concentrations in both solution and thin films.[58] Many of the aggregate geometries can be described as a cofacial geometry (H-aggregates),[59-62] a slipped geometry (J-aggregates),[52, 63-64] perpendicular aggregates,[65] or more complex structures.[51, 66-67] Computational results suggest that these aggregate geometries are at similar energies for pairs of cyanines, and many of these geometries lead to closure of the optical window along with the appearance of new excited states.[36] The type of aggregation observed can be influenced by the chemical structure of the cyanine and counterion, as well as solvent.[62, 67-72] While the inherent

aggregating behavior of cyanines has been exploited (*e.g.*, for self-assembly of J-aggregates),[73-76] much work has focused on suppressing aggregation by increasing the steric bulk of the cyanine[53, 77-79] or using large, chemically soft counterions such as BAr'_4^- (Ar' = *m*,*m*-$(CF_3)_2C_6H_3$).[55, 80]

1.5. Thesis Objective and Outline

The goal of this Thesis is to use theoretical methods to enhance our understanding of the structure-property relationships of cyanines intended for use in AOS devices. As many of the fundamental structure-property relationships governing isolated cyanines and their NLO properties have been determined, we focus here in particular on how modifications to the cyanine backbone designed to minimize the detrimental effects of ion-pairing and aggregation affect the NLO properties of interest and packings in the solid state. We also investigate the third-order optical response of binary organic mixed-stack charge transfer complexes, materials which have recently gained renewed interest for use in organic electronics. To investigate these systems, we pay attention to their molecular geometries, electronic structures, and excited-state properties to explain their third-order optical responses. A recurring theme is the importance of minimizing cyanine-counterion interactions, and what effect the counterion or strategies to minimize it has on a cyanine.

To set the stage, we begin in **Chapter 2** with a brief review of electronic-structure and molecular-dynamics methods. We start with the Schrödinger equation and use a set of approximations to derive the various electronic-structure methods used here. We then discuss density functional theory (DFT) and survey the numerous classes of functionals

commonly employed, before concluding with a discussion on molecular dynamics and atomistic force fields.

Chapter 3 discusses research performed in collaboration with the Marder group at the Georgia Institute of Technology. We focus on evaluating cyanine-based materials designed to minimize aggregation in the solid state. We show that the NLO properties of metal (M = Ni, Pd, Pt) functionalized thiopyrylium cyanines depend on the identity of the metal, before evaluating the role the counterion plays when the cyanine molecular structure is optimized with large deaggregating groups.

In **Chapter 4** we stress that cyanine-counterion interactions must be minimized by considering the effect of a counterion on the NLO properties when present at various places along a streptocyanine backbone. Binding energies and non-covalent interactions between different backbone lengths and counterions are also discussed.

We assess the geometric and electronic structures and third-order polarizability of zwitterionic cyanines designed to eliminate the need for a counterion in **Chapter 5**. We demonstrate that the compounds must possess a high degree of zwitterionic character to maintain the favorable cyanine character of the backbone, and to do so requires that charge separation between cationic and anionic moieties must be favored electronically.

Binary organic mixed-stack charge transfer complexes are the focus of **Chapter 6**. We show that their third-order response arises from the interaction between the donor and acceptor molecules and is not contingent upon the response of the individual monomers of the complex.

We conclude in **Chapter 7** with the broader impacts of this Thesis and research directions for future work.

1.6. References

1. Sandvine, Inc. Spotlight: Inside the Connected Home - 2016 Global Internet Phenomena. https://www.sandvine.com/resources/global-internet-phenomena/the-connected-home.html, Accessed April 2017.

2. Cisco Systems, Inc., White paper: Cisco VNI Forecast and Methodology, 2015-2020, http://www.cisco.com/c/en/us/solutions/collateral/service-provider/visual-networking-index-vni/complete-white-paper-c11-481360.html, Accessed April 2017.

3. Hinton, H. S. Switching to photonics. *Spectrum* **1992,** *29*, 42-45.

4. Hochberg, M.; Baehr-Jones, T.; Wang, G.; Shearn, M.; Harverd, K.; Luo, J.; Chen, B.; Shi, Z.; Lawson, R.; Sullivan, P.; Jen, A. K. Y.; Dalton, L.; Scherer, A. Terahertz all-optical modulation in a silicon-polymer hybrid system. *Nat. Mat.* **2006,** *5*, 703-709.

5. Lin, Y.-M.; Dimitrakopoulos, C.; Jenkins, K. A.; Farmer, D. B.; Chiu, H.-Y.; Grill, A.; Avouris, P. 100-GHz transistors from wafer-scale epitaxial graphene. *Science* **2010,** *327*, 662-662.

6. Alloatti, L.; Korn, D.; Palmer, R.; Hillerkuss, D.; Li, J.; Barklund, A.; Dinu, R.; Wieland, J.; Fournier, M.; Fedeli, J.; Yu, H.; Bogaerts, W.; Dumon, P.; Baets, R.; Koos, C.; Freude, W.; Leuthold, J. 42.7 Gbit/s electro-optic modulator in silicon technology. *Optics Express* **2011,** *19*, 11841-11851.

7. Ramaswami, R., Sivarajan, K., Sasaki, G. Optical Networks: A Practical Perspective. 2009: Elsevier Science.

8. Stegeman, G. I.; Wright, E. M.; Finlayson, N.; Zanoni, R.; Seaton, C. T. Third order nonlinear integrated optics. *J. Lightwave Technol.* **1988,** *6*, 953-970.

9. Stegeman, G. I.; Wright, E. M. All-optical waveguide switching. *Optical and Quantum Electronics* **1990,** *22*, 95-122.

10. Gibbs, H. M. *Optical Bistability: controlling light with light*. Academic Press: Orlando, 1985.

11. Boyd, R. W. *Nonlinear Optics*. 2nd ed. ed.; Academic Press: San Diego, California, 2003.

12. Driessen, A.; Hoekstra, H. J. W. M.; Horst, F.; Krijnen, G. J. M.; Offrein, B. J.; van Schoot, J. B. P.; Lambeck, P. V.; Popma, T. J. A, All-optical integrated optic devices: A hybrid approach. *IEE Proc.-Optoelectron.* **1998,** *145*, 227-235.

13. Mizrahi, V.; DeLong, K. W.; Stegeman, G. I.; Saifi, M. A.; Andrejco, M. J. Two-photon absorption as a limitation to all-optical switching. *Opt. Lett.* **1989,** *14*, 1140-1142.

14. Stegeman, G. I.; Stolen, R. H. Waveguides and fibers for nonlinear optics. *J. Opt. Soc. Am. B* **1989,** *6*, 652-662.

15. Hales, J. M.; Matichak, J.; Barlow, S.; Ohira, S.; Yesudas, K.; Bredas, J. L.; Perry, J. W.; Marder, S. R. Design of polymethine dyes with large third-order optical nonlinearities and loss figures of merit. *Science* **2010,** *327*, 1485-1489.

16. Kanis, D. R.; Ratner, M. A.; Marks, T. J. Design and construction of molecular assemblies with large second-order optical nonlinarities. Quantum chemical aspects. *Chem. Rev.* **1994,** *94*, 195-242.

17. Shelton, D. P.; Rice, J. E. Measurements and calculations of the hyperpolarizabilities of atoms and small molecules in the gas phase. *Chem. Rev.* **1994,** *94*, 3-29.

18. Bishop, D. M. Molecular vibrational and rotational motion in static and dynamic electric fields. *Rev. Mod. Phys.* **1990,** *62*, 343-374.

19. Orr, B. J.; Ward, J. F. Perturbation theory of the non-linear optical polarization of an isolated system. *Mol. Phys.* **1971,** *20*, 513-526.

20. Kuzyk, M. G.; Dirk, C. W. Effects of centrosymmetry on the nonresonant electronic third-order nonlinear optical susceptibility. *Phys. Rev. A* **1990,** *41*, 5098-5109.

21. Pierce, B. M. A theoretical analysis of the third-order nonlinear optical properties of linear cyanines and polyenes. *SPIE* **1991,** *1560*, 148-161.

22. Garito, A. F.; Teng, C. C. Nonlinear optical processes in organic media: large non-resonant third order electronic responses in high performance liquid crystal polymer structures. *SPIE* **1986,** *613*, 146-151.

23. Dirk, C. W.; Cheng, L.-T.; Kuzyk, M. G. A simplified three-level model describing the molecular third-order nonlinear optical susceptibility. *Int. J. of Quant. Chem.* **1992,** *43*, 27-36.

24. Butcher, P. N.; Cotter, D. *The Elements of nonlinear Optics*. Cambridge University Press: Cambridge, UK, 1991.

25. Bredas, J. L.; Adant, C.; Tackx, P.; Persoons, A. Third-order nonlinear optical response in organic materials: theoretical and experimental aspects. *Chem. Rev.* **1994,** *94*, 243-78.

26. Nalwa, H. S. Organic materials for third-order nonlinear optics. *Adv. Mater.* **1993,** *5*, 341-358.

27. Hales, J. M.; Barlow, S.; Kim, H.; Mukhopadhyay, S.; Bredas, J.-L.; Perry, J. W.; Marder, S. R. Design of organic chromophores for all-optical signal processing applications. *Chem. Mater.* **2014,** *26*, 549-560.

28. Marder, S. R.; Gorman, C. B.; Meyers, F.; Perry, J. W.; Bourhill, G.; Bredas, J. L.; Pierce, B. M. A unified description of linear and nonlinear polarization in organic polymethine dyes. *Science* **1994,** *265*, 632-635.

29. Marder, S. R.; Perry, J. W.; Bourhill, G.; Gorman, C. B.; Tiemann, B. G.; Mansour, K. Relation between bond-length alternation and second electronic hyperpolarizability of conjugated organic molecules. *Science* **1993,** *261*, 186-189.

30. Meyers, F.; Marder, S. R.; Pierce, B. M.; Bredas, J. L. Electric field modulated nonlinear optical properties of donor-acceptor polyenes: sum-over-states investigation of the telationship between molecular polarizabilites and bond length alternation. *J. Am. Chem. Soc.* **1994,** *116*, 10703-10714.

31. Marder, S. R.; Cheng, L. T.; Tiemann, b. G.; Friedli, A. C.; Blanchard-Desce, M.; Perry, J. W.; Skindhøj, J. Large first hyperpolarizabilities in push-pull polyenes by tuning of the bond length alternation and aromaticity. *Science* **1994,** *263*, 511-514.

32. Gorman, C. B.; Marder, S. R. Effect of molecular polarizability on bond-length alternation, linear polarizability, first and second yyperpolarizability in donor-acceptor polyenes as a function of chain length. *Chem. Mater.* **1995,** *7*, 215-220.

33. Hudson, B.; Kohler, B. Linear polyene electronic structure and spectroscopy. *Annu. Rev. Phys. Chem.* **1974,** *25*, 437-460.

34. Baughman, R. H.; Kohler, B. E.; Levy, I. J.; Spangler, C. The crystal structure of trans,trans-1,3,5,7-octatetraene as a model for fully-ordered trans-polyacetylene. *Synth. Met.* **1985,** *11*, 37-52.

35. Jacquemin, D. New cyanine dyes or not? Theoretical insights for model chains. *J. Phys. Chem. A* **2011,** *115*, 2442-2445.

36. Mukhopadhyay, S.; Risko, C.; Marder, S. R.; Brédas, J.-L. Polymethine dyes for all-optical switching applications: a quantum-chemical characterization of counter-ion and aggregation effects on the third-order nonlinear optical response. *Chem. Sci.* **2012,** *3*, 3103-3112.

37. Jacquemin, D.; Zhao, Y.; Valero, R.; Adamo, C.; Ciofini, I.; Truhlar, D. G. Verdict: Time-dependent density functional theory "not guilty" of large errors for cyanines. *J. Chem. Theory Comput.* **2012,** *8*, 1255-1259.

38. Jacquemin, D.; Chibani, S.; Le Guennic, B.; Mennucci, B. Solvent effects on cyanine derivatives: a PCM investigation. *J. Phys. Chem. A* **2014,** *118*, 5343-5348.

39. Gieseking, R. L.; Mukhopadhyay, S.; Shiring, S. B.; Risko, C.; Brédas, J.-L. Impact of bulk aggregation on the electronic structure of streptocyanines: implications for the solid-

state nonlinear optical properties and all-optical switching applications. *J. Phys. Chem. C* **2014,** *118*, 23575-23585.

40. Salem, L. *The molecular orbital theory of conjugated systems*. W. A. Benjamin: Reading, Mass., 1974, c1966.

41. Johr, T.; Wernecke, W.; Pfeiffer, M.; Dahne, L. Third-order nonlinear polarizabilities of a homologous series of symemtric cyanines. *Chem. Phys. Lett.* **1995,** *246*, 521-526.

42. Gieseking, R. L.; Risko, C.; Bredas, J. L. Distinguishing the effects of bond-length alternation versus bond-order alternation on the nonlinear optical properties of pi-conjugated chromophores. *J. Phys. Chem. Lett.* **2015,** *6*, 2158-2162.

43. Tolbert, L. M.; Zhao, X. Beyond the cyanine limit: peierls distortion and symmetry collapse in a polymethine dye. *J. Am. Chem. Soc.* **1997,** *119*, 3253-3258.

44. Hales, J. M.; Zheng, S.; Barlow, S.; Marder, S. R.; Perry, J. W. Bisdioxaborine polymethines with large third-order nonlinearities for all-optical signal processing. *J. Am. Chem. Soc.* **2006,** *128*, 11362-11363.

45. Yau, M. S.; Pascu, S. I.; Odom, S. A.; Warren, J. E.; Klotz, F. j. F.; Frampton, M. J.; Williams, C. C.; Coropceanu, V.; Kuimova, M. K.; Philips, D.; Barlow, S.; Bredas, J. L.; Marder, S. R.; Millar, V.; Anderson, H. L. Stabilisation of a heptamethine cyanine dye by rotaxane encapsulation. *Chem. Commun.* **2008,** *25*, 2897-2899.

46. Matichak, J. D.; Hales, J. M.; Ohira, S.; Barlow, S.; Jang, S.-H.; Jen, A. K. Y.; Bredas, J. L.; Perry, J. W.; Marder, S. R. Using end groups to tune the linear and nonlinear optical properties of bis(dioxaborine)-terminated polymethine dyes. *ChemPhysChem* **2010,** *11*, 130-138.

47. Padilha, L. A.; Webster, S.; Przhonska, O. V.; Hu, H.; Peceli, D.; Ensley, T. R.; Bondar, M. V.; Gerasov, A. O.; Kovtun, Y. P.; Shandura, M. P.; D., K.; Hagan, D. J.; Van Stryland, E. W. Efficient two-photon absorbing acceptor-π-acceptor polymethine dyes. *J. Phys. Chem. A* **2010,** *114*, 2493-6501.

48. Gieseking, R. L.; Mukhopadhyay, S.; Risko, C.; Marder, S. R.; Bredas, J. L. 25th anniversary article: design of polymethine dyes for all-optical switching applications: guidance from theoretical and computational studies. *Adv/ Mater.* **2014,** *26*, 68-83.

49. Hales, J. M.; Matichak, J.; Barlow, S.; Ohira, S.; Yesudas, K.; Bredas, J. L.; Perry, J. W.; Marder, S. R. Design of polymethine dyes with large third-order optical nolinearities and loss figures of merit. *Science* **2010,** *327*, 1485-1488.

50. Arjona-Esteban, A.; Stolte, M.; Wurthner, F. Conformational witching of pi-conjugated junctions from merocyanine to cyanine states by solvent polarity. *Angew. Chem. Int. Ed.* **2016,** *55*, 2470-2473.

51. Von Berlepsch, H.; Böttcher, C.; Dähne, L. Structure of J-aggregates of pseudoisocyanine dye in qqueous solution. *J. Phys. Chem. B* **2000,** *104*, 8792-8799.

52. Belfield, K. D.; Bondar, M. V.; Hernandez, F. E.; Przhonska, O. V.; Yao, S. Two-photon absorption of a supramolecular pseudoisocyanine J-aggregate assembly. C*hem. Phys.* **2006,** *320*, 118-124.

53. Scarpaci, A.; Nantalaksakul, A.; Hales, J. M.; Matichak, J. D.; Barlow, S.; Rumi, M.; Perry, J. W.; Marder, S. R. Effects of dendronization on the linear and third-order nonlinear optical properties of bis(thiopyrylium) polymethine dyes in solution and the solid state. *Chem. Mater.* **2012,** *24*, 1606-1618.

54. Hayes, S. C.; Bittner, E. R.; Starovoytov, A. A.; Kaliteevskaya, E.; Krutyakova, V.; Razumova, T. Influence of the molecular orientation on the optical properties and photomodification of cyanine thin film. *Proc. of SPIE* **2015,** *9549*, 95490Y-1-95490Y-5.

55. Bouit, P.-A.; Aronica, C.; Toupet, L.; Le Guennic, B.; Andraud, C.; Maury, O. Continuous symmetry breaking induced by ion pairing effect in heptamethine cyanine dyes: beyond the cyanine limit. *J. Am. Chem. Soc.* **2010,** *132*, 4328-4335.

56. Bambgelu, A.; Wang, J.; Leszczynski, J. TDDFT study of the optical properties of Cy5 and its derivatives. *J. Phys. Chem. A* **2010,** *114*, 3551-3555.

57. Karaman, R.; Menger, F. M. Electrostatic effects on the energetics and geometry of a cyanine dye. *Journal of Molecular Structure: THEOCHEM* **2010,** *959*, 87-91.

58. Jelley, E. E. Spectral absorption and fluorescence of dyes in the molecular state. *Nature* **1936,** *138*, 1009-1010.

59. Baraldi, I.; Caselli, M.; Momicchioli, F.; Ponterini, G.; Vanossi, D. Dimerization of green sensitizing cyanines in solution. A spectroscopic and theoretical study of the bonding nature. *Chem. Phys.* **2002,** *275*, 149-165.

60. Gadde, S.; Batchelor, E. K.; Weiss, J. P.; Ling, Y.; Kaifer, A. E. Control of H- and J-aggregate formation via host-guest complexation using cucurbituril hosts. *J. Am. Chem. Soc.* **2008,** *130*, 17114-17119.

61. Caselli, M.; Latterini, L.; Ponterini, G. Consequences of H-dimerization on the photophysics and photochemistry of oxacarbocyanines. *Phys. Chem. Chem. Phys.* **2004,** *6*, 3857-3863.

62. Batchelor, E. K.; Gadde, S.; Kaifer, A. E. Host–guest control on the formation of pinacyanol chloride H-aggregates in anionic polyelectrolyte solutions. *Supramolec. Chem.* **2010,** *22*, 40-45.

63. Busse, G.; Frederichs, B.; Petrov, N. K.; Techert, S. Structure determination of thiacyanine dye J-aggregates in thin films: Comparison between spectroscopy and wide angle X-ray scattering. *Phys. Chem. Chem. Phys.* **2004,** *6*, 3309-3314.

64. Tani, K.; Ito, C.; Hanawa, Y.; Uchida, M.; Otaguro, K.; Horiuchi, H.; Hiratsuka, H. Photophysical property and photostability of J-aggregate thin films of thiacyanine dyes prepared by the spin-coating method. *J. Phys. Chem. B* **2008,** *112*, 836-844.

65. Etter, M. C.; Kress, R. B.; Bernstein, J.; Cash, D. J. Solid-state chemistry and structures of a new class of mixed dyes. Cyanine-oxonol. *J. Am. Chem. Soc.* **1984,** *106*, 6921-6927.

66. Didraga, C.; Pugzlys, A.; Hania, P. R.; von Berlepsch, H.; Duppen, K.; Knoester, J. Structure, spectroscopy, and microscopic model of tubular carbocyanine dye aggregates. *J. Phys. Chem. B* **2004,** *108*, 14976-14985.

67. Mishra, A.; Behera, R. K.; Behera, P. K.; Mishra, B. K.; Behera, G. B. Cyanines during the 1990s: A review. *Chem. Rev.* **2000,** *100*, 1973-2012.

68. Gorner, H.; Chibisov, A. K.; Slavnova, T. D. Kinetics of J-aggregation of cyanine dyes in the presence of gelatin. *J. Phys. Chem. B* **2006,** *110*, 3917-3923.

69. Kawasaki, M.; Aoyama, S.; Kozawa, E. Enhanced intra-aggregate charge separation from binary excitons in mixed J-aggregates of cyanine dyes. *J. Phys. Chem. B* **2006,** *110*, 24480-24485.

70. Das, S.; Bwambok, D.; El-Zahab, B.; Monk, J.; de Rooy, S. L.; Challa, S.; Li, M.; Hung, F. R.; Baker, G. A.; Warner, I. M. Nontemplated approach to tuning the spectral properties of cyanine-based fluorescent NanoGUMBOS. *Langmuir* **2010,** *26*, 12867-12876.

71. Abd-El-Aziz, A. S.; Strohm, E. A.; Okasha, R. M. Design and spectroscopic characterization of novel series of near infrared indocyanine dyes. *J. Mol. Struc.* **2015,** *1091*, 228-235.

72. Li, Z. a.; Kim, H.; Chi, S.-H.; Hales, J. M.; Jang, S.-H.; Perry, J. W.; Jen, A. K. Y. Effects of counterions with multiple charges on the linear and nonlinear optical properties of polymethine salts. *Chem. Mater.* **2016,** *28*, 3115-3121.

73. Shapiro, B. I.; Manulik, E. V. Synthesis of mixed J-aggregates based on polymethine dyes of different structure. *Nanotechnologies in Russia* **2017,** *12*, 9-18.

74. Petrenko, A.; Stein, M. Molecular reorganization energy as a key determinant of J-band formation in J-aggregates of polymethine dyes. *J. Phys. Chem. A* **2015,** *119*, 6773-80.

75. Li, Z.; Zhao, P.; Tofighi, S.; Sharma, R.; Ensley, T. R.; Jang, S.-H.; Hagan, D. J.; Van Stryland, E. W.; Jen, A. K.-Y. Zwitterionic cyanine-cyanine salt: structure and optical properties. *J. Phys. Chem. C* **2016,** *120*, 15378-15384.

76. Li, Z.; Mukhopadhyay, S.; Jang, S. H.; Bredas, J. L.; Jen, A. K. Supramolecular assembly of complementary cyanine salt J-aggregates. *J Am Chem Soc* **2015,** *137*, 11920-11923.

77. Davydenko, I.; Barlow, S.; Sharma, R.; Benis, S.; Simon, J.; Allen, T. G.; Cooper, M. W.; Khrustalev, V.; Jucov, E. V.; Castaneda, R.; Ordonez, C.; Li, Z.; Chi, S.-H.; Jang, S. H.; Parker, T. C.; Timofeeva, T. V.; Perry, J. W.; Jen, A. K.-Y.; Hagan, D. J.; Van Stryland, E. W.; Marder, S. R. Facile incorporation of $Pd(PPh_3)_2$ Hal substituents into polymethines, merocyanines, and perylene diimides as a means of suppressing intermolecular interactions. *J. Am. Chem. Soc.* **2016,** *138*, 10112-10115.

78. Gieseking, R. L.; Mukhopadhyay, S.; Risko, C.; Marder, S. R.; Brédas, J.-L. Effect of bulky substituents on thiopyrylium polymethine aggregation in the solid state: A theoretical evaluation of the implications for all-optical switching applications. *Chem. Mater.* **2014,** *26*, 6439-6447.

79. Hales, J. M.; Kim, H.; Barlow, S.; Getmanenko, Y. A.; Zhang, Y.; Gieseking, R. L.; Risko, C.; Shahin, S.; Kieu, K.; Norwood, R. A.; Peyghambarian, N.; Bredas, J. L.; Marder, S. R.; Perry, J. W. Polymethines with macroscopic optical nonlinearities suitable for all-optical signal processing. *CLOE* **2014**.

80. Barlow, S.; Brédas, J.-L.; Getmanenko, Y. A.; Gieseking, R. L.; Hales, J. M.; Kim, H.; Marder, S. R.; Perry, J. W.; Risko, C.; Zhang, Y. Polymethine materials with solid-state third-order optical susceptibilities suitable for all-optical signal-processing applications. *Mater. Horiz.* **2014,** *1*, 577-581.

81. Fu, J.; Padilha, L. A.; Hagan, D. J.; Van Stryland, E. W.; Przhonska, O. V.; Bondar, M. V.; Slominsky, Y. L.; Kachkovskii, A. Molecular structure − two-photon absorption property relations in polymethine dyes. *J. Opt. Soc. Am. B* **2007**, *24*, 56−66.

82. Gieseking, R. L.; Mukhopadhyay, S.; Risko, C.; Brédas, J.-L. Impact of the nature of the excited-state transition dipole moments on the third-order nonlinear optical response of polymethine dyes for all-optical switching applications. *ACS Photonics* **2014**, *1*, 261-269.

CHAPTER 2

THEORETICAL METHODOLOGY

In this Chapter, we briefly review the computational methods employed within this body of work. We discuss electronic structure methods and approximations used to describe π-conjugated organic molecules in their electronic ground state and excited states, beginning with Hartree-Fock and subsequent semi-empirical and Post-Hartree-Fock methods, and concluding with Density Functional Theory and approximate functionals. An overview of atomistic simulations, in regards to molecular dynamics, is presented, including a discussion on the energetic terms in a force field. The notation used throughout this Chapter is adapted from Jensen[1] and Szabo and Ostlund.[2]

2.1. Electronic Structure Methods

2.1.1. Schrödinger Equation

Formally, all knowledge about a quantum system is contained within the many-body wavefunction, Ψ. The wavefunction for a stationary collection of particles containing N electrons at positions r_i and M light nuclei at positions R_A can be found by solving the time-independent, non-relativistic Schrödinger equation:

$$\hat{H}\psi_i = E\psi_i \tag{2.1}$$

where H is the Hamiltonian operator and E is the energy of the system at eigenstate ψ_i. The total Hamiltonian is written, in atomic units, in terms of the kinetic energies of the

electrons and nuclei ($\mathbf{T_e}$ and $\mathbf{T_n}$, respectively), and the potential energies of electron-electron ($\mathbf{V_{ee}}$) repulsion, electron-nucleus ($\mathbf{V_{en}}$) attraction, and nucleus-nucleus ($\mathbf{V_{nn}}$) repulsion in the absence of any external perturbation as:

$$\begin{aligned}\hat{H}_{tot} &= \hat{T}_e + \hat{T}_n + \hat{V}_{ee} + \hat{V}_{en} + \hat{V}_{nn} \\ &= -\frac{1}{2}\sum_{i=1}^{N}\nabla_i^2 - \frac{1}{2}\sum_{A=1}^{M}\frac{1}{M_A}\nabla_A^2 - \sum_{i=1}^{N}\sum_{A=1}^{M}\frac{Z_A}{r_{iA}} + \sum_{i=1}^{N}\sum_{J>i}^{N}\frac{1}{r_{ij}} + \sum_{A=1}^{M}\sum_{B>A}^{M}\frac{Z_A Z_B}{r_{AB}}\end{aligned} \quad (2.2)$$

where M_A is the ratio the mass of nucleus A to the mass of an electron, Z_A is the atomic number of nucleus A, $r_{iA} = |\mathbf{r_i} - \mathbf{R_A}|$ is the distance between the *i*th electron and *A*th nucleus, and $r_{AB} = |\mathbf{R_A} - \mathbf{R_B}|$ is the distance between the *A*th and *B*th nuclei. The Laplacian operators ∇_i^2 and ∇_A^2 involve the second partial derivative with respect to the coordinates of electron *i* and nucleus *A*, respectively.

As exact solutions to the Schrödinger equation are unavailable except for hydrogenoids, approximations are applied to simply the equation. A first approximation, already applied above, is to neglect relativistic effects, as these are not significant for elements composing organic molecules. A second approximation exploits the large differences between the nucleus and electron masses: since the lightest nucleus is still nearly 1,800 times heavier than the electron, the electrons respond much more quickly to variations in their environment than the nuclei. Thus, the Born-Oppenheimer approximation considers that the electrons move in a field of fixed nuclei. The total Hamiltonian then simplifies to the electronic Hamiltonian ($\mathbf{H_{elec}}$) by neglecting the $\mathbf{T_n}$ term and treating $\mathbf{V_{nn}}$ as a constant:

$$\hat{H}_{elec} = -\frac{1}{2}\sum_{i=1}^{N}\nabla_i^2 - \sum_{i=1}^{N}\sum_{A=1}^{M}\frac{Z_A}{r_{iA}} + \sum_{i=1}^{N}\sum_{J>i}^{N}\frac{1}{r_{ij}} \quad (2.3)$$

which gives the electronic Schrödinger equation:

$$\hat{H}_{elec}\psi_{elec} = E_{elec}\psi_{elec} \tag{2.4}$$

where the electronic wavefunction depends only on the coordinates of the electrons for a give nuclear configuration. The total energy is then expressed as:

$$E_{tot} = E_{elec} + E_{nuc} \tag{2.5}$$

where E_{nuc} is the nuclear repulsion energy.

2.1.2. Hartree-Fock Theory

Despite applying the above approximations, solving the electronic Schrödinger equation still becomes intractable for systems consisting of more than one electron due to their coupled motions giving rise to electron-electron repulsion ($\mathbf{V_{ee}}$). Hartree-Fock (HF) Theory invokes a further approximation by treating the electrons in a mean-field manner. The *N*-electron wavefunction (Ψ_H) then becomes a product of *N* one-electron spin-orbitals χ_i that contain the spatial and spin coordinates of electron *i;* the spin orbitals are thus composed of a spatial orbital φ(r) and one of the two spin functions, α(s) or β(s):

$$\chi(x) = \begin{cases} \varphi(\mathrm{x})\alpha(\mathrm{s}) \\ or \\ \varphi(\mathrm{x})\beta(\mathrm{s}) \end{cases} \tag{2.6}$$

To satisfy the antisymmetry principle, the *N*-electron wavefunction is represented as a single Slater determinant:

$$\Psi_H(x_1, x_2, \dots x_n) = \frac{1}{\sqrt{N!}} \begin{vmatrix} \chi_1(x_1) & \chi_j(x_1) & \dots & \chi_N(x_1) \\ \chi_1(x_2) & \chi_j(x_2) & \dots & \chi_N(x_2) \\ \vdots & \vdots & & \vdots \\ \chi_1(x_N) & \chi_j(x_N) & \dots & \chi_N(x_N) \end{vmatrix} \tag{2.7}$$

where $\frac{1}{\sqrt{N!}}$ is the normalization factor and the $\chi_i(x_j)$ are the spin-orbitals. The use of the Slater determinant ensures the indistinguishability of the electrons: the interchange of any two electrons (*i.e.*, the interchange of two rows) changes the sign of the determinant, while two electrons occupying the same spin-orbital (*i.e.*, two columns being equal) renders the determinant zero.

The best wavefunction is determined according to the variational principle, which states that the energy of the Hartree-Fock wavefunction is always greater than or equal to the exact energy, E_0:

$$E_{elec} = \langle \Psi_H | H_{elec} | \Psi_H \rangle \geq E_0 \tag{2.8}$$

where we assume a normalized wavefunction. By minimizing E_{elec} with respect to the spin-orbitals, the Hartree-Fock equation to determine the optimal spin-orbitals can be obtained:

$$f(i)\chi(x_i) = E_{HF}\chi(x_i) \tag{2.9}$$

where $f(i)$ is the Fock operator, an effective one-electron operator of the form:

$$f(i) = -\frac{1}{2}\nabla_i^2 - \sum_{A=1}^{M} \frac{Z_A}{r_{iA}} + v^{HF}(i) \tag{2.10}$$

where $v^{HF}(i)$ is potential of the *i*th electron due to the mean field of the other electrons. The electronic component of the HF energy is then expressed as:

$$E_{HF} = \sum_{i}^{N} \left(i|\hat{h}|i\right) + \frac{1}{2}\sum_{i}^{N}\sum_{j}^{N} (ii|jj) - (ij|ji) \tag{2.11}$$

with the first term

$$\left(i|\hat{h}|i\right) = \int \chi_i^*(x_1)\left[-\frac{1}{2}\nabla_i^2 - \sum_{A}^{M}\frac{Z_A}{r_{iA}}\right]\chi_i(x_1)d(x_1) \tag{2.12}$$

corresponding to the one-electron integral for the kinetic energy and electron-nuclear attraction of electron *i*, and the following two two-electron terms

$$(ii|jj) = \iint \chi_i^*(x_1)\chi_i(x_1)\frac{1}{r_{12}}\chi_j^*(x_2)\chi_j(x_2)dx_1dx_2 \tag{2.13}$$

$$(ij|ji) = \iint \chi_i^*(x_1)\chi_j(x_1)\frac{1}{r_{12}}\chi_j^*(x_2)\chi_i(x_2)dx_1dx_2 \tag{2.14}$$

corresponding to the Coulomb and exchange integrals, respectively.

The energy must be solved for iteratively, as equations 2.13 and 2.14 depend on the spin-orbitals of the other electrons. This is accomplished through the so-called self-consistent-field (SCF) method, where the orbitals are optimized iteratively to obtain the lowest possible energy within the constraint of orthonormal orbitals. The HF spin-orbitals are typically defined as a linear combination of atom-centered Gaussian functions to form molecular orbitals

2.1.3. Semi-Empirical Approximations

Despite the HF method's use of approximations, the cost of a HF calculation formally scales as $O(n^4)$, where n is the number of basis functions, due to computing the two-electron integrals. Historically, semi-empirical methods have sought to reduce this cost by reducing the number of two-electron integrals that must be calculated. All semi-empirical techniques share two common approximations: they only consider the valence electrons explicitly, and they use only a minimum basis set (consisting mostly of *s*- and *p*- orbitals and functions).

At the heart of semi-empirical methods lies the Zero Differential Overlap (ZDO) scheme, which assumes that there is no overlap between basis functions centered on different atoms. Subsequently, all one-electron integrals involving three atom centers are assumed to be zero, and all two-electron integrals involving three or four atom centers are neglected. To compensate for these drastic approximations, the remaining integrals are then parameterized in such a way as to reproduce results derived from higher-level computational or experimental results.

Various semi-empirical methods have been developed which are defined by the number of integrals neglected and the method of parameterization. The semi-empirical method used within this dissertation is the Intermediate Neglect of Differential Overlap (INDO) method, in which all two-atom centered two-electron integrals are neglected that are not of the Coulomb type. This method then is coupled to a configuration interaction scheme, to be described below.

2.1.4. Post-Hartree-Fock

As shown above, HF is a mean-field theory which assumes that each electron individually moves within a static field created by the remaining electrons. This assumption neglects electron correlation (*i.e.*, instantaneous electron-electron interactions), treating the real electron-electron interaction by an average interaction. Inclusion of this dynamic electron correlation improves the HF energy, which can be accomplished by explicitly including multiple Slater determinants as in configuration interaction (CI). Both ground state and excited states can be considered by including multiple determinants of appropriate configuration.

2.1.4.1. Configuration Interaction

Within CI, the *N*-electron wavefunction can be expressed exactly as a linear combination of all possible *N*-electron Slater determinants. The total wavefunction, $|\Phi\rangle$, is composed of *N*-electron basis functions $|\Psi\rangle$ that are constructed as Slater determinants involving excitations of electrons from the HF reference determinant, $|\Psi_0\rangle$:

$$|\Phi\rangle = c_0|\Psi_0\rangle + \sum_{a,r} c_a^r|\Psi_a^r\rangle + \sum_{\substack{a<b \\ r<s}} c_{ab}^{rs}|\Psi_{ab}^{rs}\rangle + \sum_{\substack{a<b<c \\ r<s<t}} c_{abc}^{rst}|\Psi_{abc}^{rst}\rangle + \cdots$$
$$= c_0|\Psi_0\rangle + c_S|S\rangle + c_D|D\rangle + c_T|T\rangle + \cdots \quad (2.15)$$

In the expansion, $|\Psi_a^r\rangle$ represents a Slater determinant that is different from $|\Psi_0\rangle$ only by replacing the spin orbital χ_a with χ_r corresponding to a single electron excitation, and $|\Psi_{ab}^{rs}\rangle$ and $|\Psi_{abc}^{rst}\rangle$ analogously represent doubly and triply excited Slater determinants, respectively. The CI coefficients for each Slater determinant are labelled as c_0, c_a^r, etc. A

compact form can be written symbolically by using the CI coefficient c_S and determinant $|S\rangle$ to represent all single-electron excitations and similar terms for multi-electron excitations. The structure of the CI matrix (shown only as a lower triangle) can then be written as:

$$\begin{array}{c} \\ \langle\Psi_0| \\ \langle S| \\ \langle D| \\ \langle T| \\ \vdots \end{array} \begin{array}{c} \begin{array}{ccccc} |\Psi_0\rangle & |S\rangle & |D\rangle & |T\rangle & \ldots \end{array} \\ \begin{bmatrix} \langle\Psi_0|H|\Psi_0\rangle & & & & \ldots \\ 0 & \langle S|H|S\rangle & & & \ldots \\ \langle D|H|\Psi_0\rangle & \langle D|H|S\rangle & \langle D|H|D\rangle & & \ldots \\ 0 & \langle T|H|S\rangle & \langle T|H|D\rangle & \langle T|H|T\rangle & \ldots \\ \vdots & \vdots & \vdots & \vdots & \vdots \end{bmatrix} \end{array} \tag{2.16}$$

As a consequence of Brillouin's theorem, matrix elements of the type $\langle\Psi_0|H|S\rangle$ are 0, as there is no coupling between the HF ground state and single excitations. Furthermore, according to Slater's rule, there is no coupling between determinants that differ by more than two orbitals, so $\langle\Psi_0|H|T\rangle$ and higher-order terms are equal to zero. The eigenvectors and eigenvalues of the CI matrix yield the wavefunctions and corresponding energies for the ground state and excited states.

The number of determinants increases factorially with the number of electrons and basis functions, such that full CI is impractical for systems of chemical interest. In order for CI calculations to be performed with less difficulty, the CI expansion is often truncated. Typically, excitations are limited to those relative to the ground state within a reduced active space, which includes only some of the occupied and unoccupied orbitals. SCI considers only single excitations from the ground state, while higher-order truncations such as SDCI consider both single and double excitations. Specific reference determinants may be included through a multi-reference determinant (MRDCI) scheme. It should be stressed

that while full CI is an exact theory, truncated CI is no longer exact and is not size extensive or size consistent.

2.1.4.2. Symmetry Adapted Cluster-Configuration Interaction

SAC-CI is an alternative method to recover the electron correlation that is both size extensive and size consistent.[3-5] In the SAC-CI method, a symmetry-adapted excitation operator operates on the HF ground-state ($|\Psi_{gs}^{HF}\rangle$) to yield symmetry-adapted configurations. States are thus restricted to certain symmetry constraints, such as spatial and spin symmetries. The symmetry-adapted ground state ($|\Psi_{gs}^{SAC}\rangle$) is expressed as

$$|\Psi_{gs}^{SAC}\rangle = \exp(S)|\Psi_{gs}^{HF}\rangle \tag{2.17}$$

where $S = \sum_i C_i S_i$. The cluster expansion of $\exp(S)$ ($\exp(S) = 1 + \sum_i C_i S_i + \frac{1}{2}\sum_i C_i C_j S_i S_j + \cdots$) incorporates doubles, triples, and quadruple excitations. The expansion is usually truncated at $\sum_i C_i C_j S_i S_j$ to include both single and double excitations.

2.1.4.3. Symmetry Adapted Perturbation Theory

Understanding non-covalent interactions is critical when studying the interactions between non-bonded chemical groups. The SAPT method has been developed to compute directly the non-covalent interaction between two molecules.[6] Considering a complex of two monomers, A and B, the non-covalent interactions between the two can be evaluated by computing the interaction energy:

$$E_{interaction} = E_{dimer}^{complex} - E_{monomer\ A}^{complex} - E_{monomer\ B}^{complex} \quad (2.18)$$

SAPT is a method which decomposes the interaction energy into a sum of physically motivated terms[7-8]:

$$E_{SAPT} = E_{elec}^{(1)} + E_{exch}^{(1)} + E_{ind}^{(2)} + E_{disp}^{(2)} \quad (2.19)$$

where $E_{elec}^{(1)}, E_{exch}^{(1)}, E_{ind}^{(2)}, E_{disp}^{(2)}$ are the first-order electrostatic, first-order exchange, second-order induction, and second-order dispersion contribution, respectively. The *electrostatics* term represents the electrostatic (*i.e.*, Coulombic) interaction between the monomer's charge distributions. The *exchange-repulsion* term captures the purely quantum mechanical effect of electrons of the same spin avoiding the overlap region of the monomers wavefunctions, and is a result of the Pauli Exclusion Principle. The *induction* term arises from the mutual polarization of each monomer by each monomer's unperturbed static electric field. Finally, the *dispersion* term results from the interaction of instantaneous charge fluctuations, mostly as a result of dipole-dipole fluctuations.

2.1.5. Density Functional Theory

Hartree-Fock-based methods rely on the *N*-electron wavefunction, which contains 4*N* variables (three spatial and one spin coordinate, for each electron). Density Functional Theory (DFT), based on the seminal proof by Hohenberg and Kohn, instead focuses on the electron density, $\rho(r)$, containing a total of only three spatial variables.[9] Hohenberg and Kohn posited that there exists a one-to-one correspondence between the ground-state

electronic energy and the electron density. Hohenberg and Kohn introduced two theorems upon which modern DFT is built.

2.1.5.1 Hohenberg-Kohn Theorems

The first theorem states that an external potential, $V_{ext}(r)$, is a unique functional of $\rho(r)$, and because $\rho(r)$ uniquely determines the Hamiltonian, it also uniquely determines all other molecular properties. The second theorem is a recapitulation of the variational principle for DFT, stating that the ground-state energy may be obtained variationally and that the electron density that minimizes the total energy is the exact ground state. The second theorem allows the self-consistent machinery developed for wavefunction methods to be applied to DFT.

From the first theorem, the expectation value for an observable may be defined as a functional of the electron density:

$$\langle A \rangle = A[\rho(r)] \tag{2.20}$$

and that the energy is defined as:

$$E[\rho(r)] = \langle \Psi | H | \Psi \rangle = T[\rho] + E_{Ne}[\rho] + E_{ee}[\rho] \tag{2.21}$$

in which the Hamiltonian consists of a kinetic energy component, $T[\rho]$, a nuclear-electron attraction component, $E_{Ne}[\rho]$, and an electron-electron repulsion component, $E_{ee}[\rho]$. The electron density is defined as:

$$\rho(r) = N \int d^3 r_2 \dots \int d^3 r_N |\Psi(r_1, r_2, \dots, r_N)|^2 \tag{2.22}$$

The universal functional of Hohenberg and Kohn is then introduced as the sum of the electron-only contributions:

$$F[\rho(r)] = \langle \Psi | T + V_{ee} | \Psi \rangle = T[\rho] + J[\rho] + E_{ncl}[\rho] \quad (2.23)$$

where $J[\rho]$ and $E_{ncl}[\rho]$ are the Coulomb functional and the non-classical correlation functional, respectively. $E_{ncl}[\rho]$ encapsulates the effects of self-interaction, exchange, and electron correlation. While the form of $J[\rho]$ is known exactly, the exact form of $E_{ncl}[\rho]$ is unknown and must be approximated.

2.1.5.2. Kohn-Sham Theory

Although DFT as originally derived by Hohenberg-Kohn is orbital free and relies exclusively on the electron density, deriving an exact kinetic energy term as a function of the density has proven elusive. Therefore, Kohn and Sham proposed introducing orbitals, reducing the problem of interacting electrons in an external potential to one of a system of non-interacting electrons in an effective potential.[10] As a consequence, the complexity has returned to 3N variables, and the approximate density of the system can be written as a sum of the electron densities of the occupied orbitals as:

$$\rho_{approx} = \sum_{i}^{N} |\varphi_i|^2 \quad (2.24)$$

The kinetic energy term is then split into an orbital-based term and a small correction term. The orbital-based kinetic energy term is known exactly:

$$T_S = -\frac{1}{2} \sum_{i}^{N} \langle \varphi_i | \nabla^2 | \varphi_i \rangle \quad (2.25)$$

and the correction term is often accounted for by the functional kernel selected. The universal functional then becomes:

$$F[\rho] = T_s[\rho] + J[\rho] + E_{XC}[\rho] \tag{2.26}$$

where $E_{XC}[\rho]$ is the exchange-correlation energy. This term contains the correction to the kinetic energy and the non-classical electron correlation contribution:

$$E_{XC}[\rho] = (T[\rho] - T_s[\rho]) + (E_{ee}[\rho] - J[\rho]) \tag{2.27}$$

where the first term is the kinetic correlation energy, and the second term contains both the potential correlation energy and the exchange energy. The total energy of the system is then written as

$$E_v[\rho] = T_S[\rho] + E_{eN}[\rho] + J[\rho] + E_{XC}[\rho] \tag{2.28}$$

The Schrödinger equation is:

$$\left[-\frac{1}{2}\nabla^2 - \sum_A^M \frac{Z_A}{r_{iA}} + \int \frac{\rho(r_2)}{r_{12}} dr_2 + V_{XC}(r_1)\right]\phi_i = \varepsilon_i \phi_i \tag{2.29}$$

with the exchange-correlation potential, V_{XC}, as:

$$V_{XC} = \frac{\delta E_{XC}}{\delta \rho} \tag{2.30}$$

Unfortunately, the exact form of this exchange-correlation potential is not known, and subsequently the accuracy of a DFT functional depends on the accuracy of its exchange-correlation potential and the approximations contained therein.

2.1.5.3. Approximate Exchange-Correlation Functionals

The choice of the functional form (*i.e.*, the expression for the exchange-correlation potential) is the difference between the various DFT methods. In contrast to wavefunction methods, as each DFT functional contains its own approximations, a systematic approach

to improving overall accuracy is impossible. Perdew and Schmidt introduced a "Jacob's ladder" hierarchy of functional approximations to aide in categorizing functionals based on the complexity of their functional form.[11] We briefly review below four of the most common types of functionals currently in use.

Local Density Approximation

This is the simplest approximation for the exchange-correlation, and it treats local electron density as a uniform electron gas, assuming that the density slowly varies over space. In that context, the exchange energy is known exactly and is given by the Dirac formula:

$$E_X^{LDA}[\rho] = -C_X \int \rho^{4/3}(\vec{r})d\vec{r} \tag{2.31}$$

where $C_X = {}^{3}/_{4}\sqrt[3]{{}^{3}/_{\pi}}$. The correlation energy is not known exactly, except at high and low density limits; for intermediate values, its contributions are derived from quantum Monte Carlo simulations on the uniform electron gas. While the assumption of approximating the electron density as a slowly varying density is valid for systems like metals, in molecular systems this assumption is not as robust as the electron density varies significantly over space. Subsequently, this approach tends to underestimate the exchange energy and overestimate the correlation energy.

Generalized Gradient Approximation

Since the electron density is not uniform in space in molecular systems, the generalized gradient approximation includes information about the gradient of the electron density, $\nabla\rho$, in addition to the electron density at a given point to take into account the inhomogeneity, in particular, of molecular systems. The exchange-correlation term then takes on the form:

$$E_X^{GGA}[\rho] = \int \rho(r)\varepsilon_{XC}^{GGA}\left(\rho_\alpha, \rho_\beta, \nabla\rho_\alpha, \nabla\rho_\beta\right)dr \tag{2.32}$$

which accounts for any difference in electron spin densities.

Hybrid Functionals

Within the exchange-correlation potential, the exchange contributions are typically much larger than the correlation contributions. Hybrid functionals seek to improve the total energy by computing a more accurate exchange energy. This is accomplished by including some fraction of Hartree-Fock exchange in the DFT exchange-correlation functional:

$$E_{XC}^{hybrid}[\rho] = aE_X^{HF} + (1-a)E_X^{KS} + E_C^{KS} \tag{2.33}$$

Introducing the HF exchange has the advantage of minimizing the self-interaction error pathological to DFT. In DFT, the density of a single electron causes a non-zero Coulomb repulsion ($J[\rho]$). In HF, the exchange is exact in the limit of non-interacting electrons. While this approach has been shown to generally improve the accuracy of molecular properties, the accuracy relies on the fraction of HF exchange which is dependent on the system and properties of interest. To date, many hybrid functionals incorporating HF

exchange have been developed; among them, the most popular is the B3LYP functional.[12-13]

Long-Range Corrected Functionals

Despite these improvements, hybrid functionals fail to describe distance-dependent exchange interactions, resulting in incorrect exponential asymptotic behavior at long range. To resolve this inadequacy, long-range corrected functionals have been developed, in which the two-electron operator is partitioned into short-range and long-range components by the standard error function as[14-15]

$$\frac{1}{r_{12}} = \frac{1 - erfc(\omega r_{12})}{r_{12}} + \frac{erf(\omega r_{12})}{r_{12}} \tag{2.34}$$

where ω is a parameter for determining the distance for transitioning between the short-range and long-range contributions. The short-range component is handled by the DFT exchange, which accurately describes short-range interactions, while the long-range component is handled by HF exchange, which has the correct long-range asymptotic behavior. The general functional form is:

$$E_{XC}^{LRC}[\rho] = E_X^{SR-KS} + E_X^{SR-HF} + E_X^{LR-HF} + E_C^{KS} \tag{2.35}$$

2.2. Atomistic Simulations

While HF, post-HF, and DFT methods have enjoyed success in calculating a variety of molecular properties, electronic-structure methods are limited in application to small-to-medium sized molecules. As simulating large ensembles of molecules containing thousands of atoms is essential for describing the bulk morphological properties of materials, approximate methods must be used. Molecular Dynamics (MD) is an approximate technique that uses classical mechanics to describe the motion of particles within a bulk material by propagating an initial configuration according to Newton's second equation. MD relies on force fields, which are composed of sets of parameters that define the potential energy, using fitted terms for different interactions, to calculate the energy as a function of nuclear coordinates.

2.2.1. Force Fields

Since electrons are neglected and the electronic Schrödinger equation is unused, information concerning bonded and non-bonded interactions between atoms must be explicitly provided by the use of force fields. The force field energy is generally written as:

$$E = E_{str} + E_{bend} + E_{tors} + E_{vdw} + E_{el} \tag{2.36}$$

The first three terms describe bonded interactions (stretch, bend, and torsion rotation, respectively), while the remaining terms describe non-bonded interactions (van der Waals and electrostatic energy, respectively). The physical parameters (*e.g.*, equilibrium bond lengths, equilibrium angles, force constants) used to define each atom used within a MD

simulation are derived from experimental measurements or higher-level electronic-structure methods.

Bonded Interactions

The stretch energy, E_{str}, is the energy of stretching a pair of bonded atoms A and B about their equilibrium bond length, R_0^{AB}. This term is typically described by a harmonic potential, which is sufficient for a description at bond lengths near its energetic minimum:

$$E_{str}(R^{AB}) = k^{AB}(R^{AB} - R_0^{AB})^2 \tag{2.37}$$

The bend energy, E_{bend}, is the energy needed to bend a molecule about an angle (θ) formed by three bonded atoms, A-B-C. A harmonic potential again is used to describe this interaction:

$$E_{bend}(R^{AB}) = \theta^{ABC}(\theta^{ABC} - \theta_0^{ABC})^2 \tag{2.38}$$

The final bonded term, the torsion energy, E_{tor}, describes the energy change when rotating about the bond B-C in a A-B-C-D, a set of four bonded atoms. The torsion potential does not share a harmonic potential as the previous two terms did, for the torsion potential function must be periodic (a rotation of 360° should return the same energy) and the energetic barrier of rotation is often small. To capture these effects, $E_{tor}$is written as a Fourier series:

$$E_{tors}(\omega^{ABCD}) = \sum_{n} V_n^{ABCD}(cos\omega^{ABCD}) \tag{2.39}$$

Non-Bonded Interactions

The first non-bonded term, the van der Waals term (E_{vdw}), describes the repulsion or attraction between non-bonded atoms, including exchange-repulsion at short interatomic distances and weak attraction due to dispersion at intermediate distances. A Lennard-Jones potential is usually selected to express this term due to its computational efficiency:

$$E_{vdw}(R^{AB}) = \varepsilon^{AB}\left[\left(\frac{R_0^{AB}}{R^{AB}}\right)^{12} - 2\left(\frac{R_0^{AB}}{R^{AB}}\right)^{6}\right] \tag{2.40}$$

where R_0^{AB} is the minimum-energy distance, and ε^{AB} is the depth of the potential well. The pairwise interactions in the minimum-energy distance are usually expressed in terms of the atomic van der Waals radii and interaction energies via:

$$R_0^{AB} = R_0^A + R_0^B \tag{2.41}$$

$$\varepsilon^{AB} = \sqrt{\varepsilon^A \varepsilon^B}$$

Finally, point charges are used to compute electrostatic interactions (E_{el}). These interactions include charge-charge, charge-dipole, dipole-dipole, and higher multipole interactions. The molecular charge distribution is taken as being atom-centered, and the interactions between the point charges are calculated using the Coulomb potential:

$$E_{el}(R^{AB}) = \frac{Q^A Q^B}{\varepsilon R^{AB}} \tag{2.42}$$

where ε is the dielectric constant. The values for the atomic charges (Q^A and Q^B) can be computed from quantum-mechanical calculations or from standard atomic charges for each atom.

2.2.2. Molecular Dynamics

As stated above, MD treats the motion of the particles in a simulation trajectory classically according to Newton's second equation:

$$-\frac{dV}{dr} = m\frac{d^2r}{dt^2} \tag{2.43}$$

This equation must be integrated over the simulation run time. This run time is broken into discrete time steps, at which the velocities and positions of all the particles are calculated. The size of the time steps taken must be shorter than the rate of the fastest process of interest; in order to accurately capture molecular vibrations, a time step on the order of 1 femtosecond is required. At time step $i+1$, the new atomic positions (r_{i+1}) can be written in terms of the old atomic positions (r_i), velocities (v_i), and accelerations (a_i) of the previous time step i. This is generally expressed as a Taylor series expansion:

$$r_{i+1} = r_i + \frac{\partial r}{\partial t}(\Delta t) + \frac{1}{2}\frac{\partial^2 r}{\partial t^2}(\Delta t)^2 + \cdots \tag{2.44}$$

$$= r_i + v_i(\Delta t) + \frac{1}{2}a_i(\Delta t)^2 + \cdots$$

where Δt is the time step between steps i and $i+1$.

There are many algorithms available to perform this integration. The one implemented in the software used in this dissertation is the Verlet algorithm, which is the most common

integration algorithm used. This algorithm uses the present atomic coordinates at time t and the atomic coordinates at the previous time step ($t - \Delta t$) to compute the new positions and accelerations for the next time step at time $t + \Delta t$. The velocities, while not used to compute the next time step, are typically approximated.

The MD method generates an ensemble at the end of a simulation. An ensemble is a large collection of microscopic states that can describe all possible states of a system. The results from an MD simulation can be related to macroscopic observables by invoking the ergodic hypothesis: given infinite time a system will pass through all possible states, implying that averaging over a single particle or a few for a sufficiently long length of time is equivalent to an average over a large number of particles at a discrete moment in time.

2.3. Programs Used

All electronic-structure methods used for calculations in this dissertation were implemented in the following software packages: Gaussian09 (Rev. B.01 and Rev. D.01)[1617], PSI (4.0.0.-beta5+)[18], and ZINDO. All crystal structures were obtained from the Cambridge Crystallographic Database.[19] Crystal structures were analyzed by and geometries extracted with Mercury 3.0.[20] Custom scripts were developed to aide in data analysis. Molecular Dynamics simulations were carried out using GROMACS 4.5.4[21] and the OPLS-AA force field.[22]

2.4. References

1. Jensen, F., *Introduction to Computational Chemistry*. 2nd Ed. ed.; John Wiley & Sons, Ltd.: Hoboken, New Jersey, 2007.

2. Szabo, A.; Ostlund, N. S., *Modern Quantum Chemistry: Introduction to Advanced Electronic Structure Theory*. 1st, Rev. Ed. ed.; McGraw-Hill, Inc: New York, 1989.

3. Nakatsuji, H. Cluster expansion of the wavefunction. Excited states. *Chem. Phys. Lett.* **1978,** *59*, 362-364.

4. Nakatsuji, H. Cluster expansion of the wavefunction. Electron correlations in ground and excited states by SAC (symmetry-adapted-cluster) and SAC CI theories. *Chem. Phys. Lett.* **1979,** *67*, 329-333.

5. Nakatsuji, H. Cluster expansion of the wavefunction. Calculation of electron correlations in ground and excited states by SAC and SAC CI theories. *Chem. Phys. Lett.* **1979,** *67*, 334-342.

6. Jeziorski, B.; Moszynski, R.; Szalewicz, K. perturbation theory approach to intermolecular potential energy surfaces of van der waals complexes. *Chem. Rev.* **1994,** *94*, 1887-1930.

7. Jeziorski, B.; Moszynski, R.; Szalewicz, K. Perturbation theory approach to intermolecular potential energy surfaces of van der waals complexes. *Chem. Rev.* **1994,** *94*, 1887-1930.

8. Hesselmann, A.; Jansen, G.; Schutz, M. Density-functional theory-symmetry-adapted intermolecular perturbation theory with density fitting: A new efficient method to study intermolecular interaction energies. *J. Chem. Phys.* **2005,** *122*, 014103.

9. Hohenberg, P.; Kohn, W. Inhomogeneous electron gas. *Phys. Rev. B* **1964,** *136*, B864.

10 Kohn, W.; Sham, L. Self-consistent equations including exchange and correlation effects. *J. Phys. Rev.* **1965,** *140*, A1133.

11. Perdew, J. P.; Schmidt, K. Jacob's ladder of density functional approximations for the exchange-correlation energy. *AIP Conf. Proc.* **2001,** *577*, 1-20.

12. Lee, C. T.; Yang, W. T.; Parr, R. G. Development of the Colle-Salvetti correlation-energy formula into a functional of the electron density. *Phys. Rev. B* **1988,** *37*, 785-789.

13. Becke, A. D. Density-functional thermochemistry. III. The role of exact exchange. *J. Chem. Phys.* **1993,** *98*, 5648-5652.

14. Savin, A.; Flad, H. J. Density functionals for the Yukawa electron-electron interaction. *Int. J. Quantum Chem.* **1995,** *56*, 327-332.

15. Gill, P. M. W.; Adamson, R. D.; Pople, J. A. Coulomb-attenuated exchange energy density functionals. *Mol. Phys.* **1996**, *88*, 1005-1009.

16. Gaussian 09, Revision B.01, M. J. Frisch, G. W. Trucks, H. B. Schlegel, G. E. Scuseria, M. A. Robb, J. R. Cheeseman, G. Scalmani, V. Barone, B. Mennucci, G. A. Petersson, H. Nakatsuji, M. Caricato, X. Li, H. P. Hratchian, A. F. Izmaylov, J. Bloino, G. Zheng, J. L. Sonnenberg, M. Hada, M. Ehara, K. Toyota, R. Fukuda, J. Hasegawa, M. Ishida, T. Nakajima, Y. Honda, O. Kitao, H. Nakai, T. Vreven, J. A. Montgomery, Jr., J. E. Peralta, F. Ogliaro, M. Bearpark, J. J. Heyd, E. Brothers, K. N. Kudin, V. N. Staroverov, T. Keith, R. Kobayashi, J. Normand, K. Raghavachari, A. Rendell, J. C. Burant, S. S. Iyengar, J. Tomasi, M. Cossi, N. Rega, J. M. Millam, M. Klene, J. E. Knox, J. B. Cross, V. Bakken, C. Adamo, J. Jaramillo, R. Gomperts, R. E. Stratmann, O. Yazyev, A. J. Austin, R. Cammi, C. Pomelli, J. W. Ochterski, R. L. Martin, K. Morokuma, V. G. Zakrzewski, G. A. Voth, P. Salvador, J. J. Dannenberg, S. Dapprich, A. D. Daniels, O. Farkas, J. B. Foresman, J. V. Ortiz, J. Cioslowski, and D. J. Fox, Gaussian, Inc., Wallingford CT, 2010.

17. Gaussian 09, Revision D.01, M. J. Frisch, G. W. Trucks, H. B. Schlegel, G. E. Scuseria, M. A. Robb, J. R. Cheeseman, G. Scalmani, V. Barone, B. Mennucci, G. A. Petersson, H. Nakatsuji, M. Caricato, X. Li, H. P. Hratchian, A. F. Izmaylov, J. Bloino, G. Zheng, J. L. Sonnenberg, M. Hada, M. Ehara, K. Toyota, R. Fukuda, J. Hasegawa, M. Ishida, T. Nakajima, Y. Honda, O. Kitao, H. Nakai, T. Vreven, J. A. Montgomery, Jr., J. E. Peralta, F. Ogliaro, M. Bearpark, J. J. Heyd, E. Brothers, K. N. Kudin, V. N. Staroverov, T. Keith, R. Kobayashi, J. Normand, K. Raghavachari, A. Rendell, J. C. Burant, S. S. Iyengar, J. Tomasi, M. Cossi, N. Rega, J. M. Millam, M. Klene, J. E. Knox, J. B. Cross, V. Bakken, C. Adamo, J. Jaramillo, R. Gomperts, R. E. Stratmann, O. Yazyev, A. J. Austin, R. Cammi, C. Pomelli, J. W. Ochterski, R. L. Martin, K. Morokuma, V. G. Zakrzewski, G. A. Voth, P. Salvador, J. J. Dannenberg, S. Dapprich, A. D. Daniels, O. Farkas, J. B. Foresman, J. V. Ortiz, J. Cioslowski, and D. J. Fox, Gaussian, Inc., Wallingford CT, 2013.

18. J. M. Turney, A. C. Simmonett, R. M. Parrish, E. G. Hohenstein, F. A. Evangelista, J. T. Fermann, B. J. Mintz, L. A. Burns, J. J. Wilke, M. L. Abrams, N. J. Russ, M. L. Leininger, C. L. Janssen, E. T. Seidl, W. D. Allen, H. F. Schaefer, R. A. King, E. F. Valeev, C. D. Sherrill, and T. D. Crawford, WIREs Comput. Mol. Sci., (2011) (doi: 10.1002/wcms.93)

19. Allen, F. H. The Cambridge Structural Database: a quarter of a million crystal structures and rising. *Acta Crystallogr.* **2002**, *B58*, 380-388.

20. Macrae, C. F.; Bruno, I. J.; Chisholm, J. A.; Edgington, P. R.; McCabe, P.; Pidcock, E.; Rodriquez-Monge, L.; Taylor, R.; Streek, J. v. d.; Wood, P. A. Mercury CSD 2.0 – new features for the visualization and investigation of crystal structures. *J. Appl. Cryst.* **2008**, *41*, 466-470.

21. Written by Emile Apol, Rossen Apostolov, Herman J.C. Berendsen, Aldert van Buuren, Pär Bjelkmar, Rudi van Drunen, Anton Feenstra, Gerrit Groenhof, Peter Kasson,Per Larsson, Pieter Meulenhoff, Teemu Murtola, Szilard Pall, Sander Pronk, Roland Schulz, Michael Shirts, Alfons Sijbers, Peter Tieleman, Berk Hess, David van der Spoel,and Erik Lindahl. Copyright (c) 1991-2000, University of Groningen, The Netherlands. Copyright (c) 2001-2010, The GROMACS development team at Uppsala University & The Royal Institute of Technology, Sweden.

22. Jorgensen, W. L.; Maxwell, D. S.; Tirado-Rives, J. Development and testing of the opls all-atom force field on conformational energetics and properties of organic liquids. *J. Am. Chem. Soc.* **1996**, *118*, 11225-11236.

CHAPTER 3

CYANINES WITH BULKY SUBSTITUENTS: INFLUENCE OF CYANINE AND COUNTERION SIZES ON CYANINE AGGREGATION

3.1. Introduction

Translating the promising optical properties of cyanines found in dilute solution into high number density materials suitable for AOS applications is one of the critical challenges facing the field. Although the highly polarizable nature of the cyanine π-system makes these molecules desirable for NLO applications, this same property also leads to strong intermolecular interactions in the solid state.[1] In particular, intermolecular interactions, including π-π interactions, between cyanines in thin films result in the formation of various aggregate geometry structures, such as J-aggregates or H-aggregates.[2-4] Aggregation can severely adversely modify the cyanine NLO properties of interest for AOS.[5-9] Limiting these intermolecular interactions to reduce cyanine-cyanine aggregation is thus critical to achieve materials with figures-of-merit suitable for these applications. Both molecular dynamics and experimental studies have suggested that increasing the cyanine steric bulk by attaching bulky out-of-plane groups to the cyanine backbone is an effective way to minimize aggregation.[10-11]

One strategy recently pursued by the Marder group at the Georgia Institute of Technology has been to introduce a large rigid bulky substituent to the center of the cyanine backbone; these molecules have been shown experimentally to maintain dilute solution-like NLO

properties in thin films.[12] The bulky substituent, composed primarily of two triphenylphosphine groups (PPh_3), is introduced to the thiopyrylium cyanine backbone *via* a square-planar metal center. In this Chapter, we use a combination of electronic structure and MD methodologies to investigate how the addition a carbon-metal bond influences the electronic structure of the thiopyrylium backbone, and what impact the addition of a large substituent to the center of the backbone has on the cyanine-cyanine packings. We compare these metallated thiopyrylium cyanines to heptamethine benzo[g]indolium cyanines, whose generally bulky structures have also been designed and synthesized by the Marder group to minimize aggregation (Figure 3.1).

Since cyanines carry a charge, this charge must be balanced by the presence of a counterion. As cyanine-counterion interactions (*e.g.*, ion-pairing) can also induce geometric changes of the backbone which negatively impact NLO properties, it is critical to assess how the structures of the cyanine and counterion influence the locations the counterion can occupy about the cyanine backbone. Although larger counterions can reduce ion-pairing with the cyanine backbone[5] and have been shown to aid in reducing aggregation,[1] an investigation into their impact on aggregation when the cyanine itself is tailored to minimize aggregation is lacking, particularly from a theoretical perspective. We thus use MD to investigate the ability of the counterion to aid in minimizing aggregation in thin films.

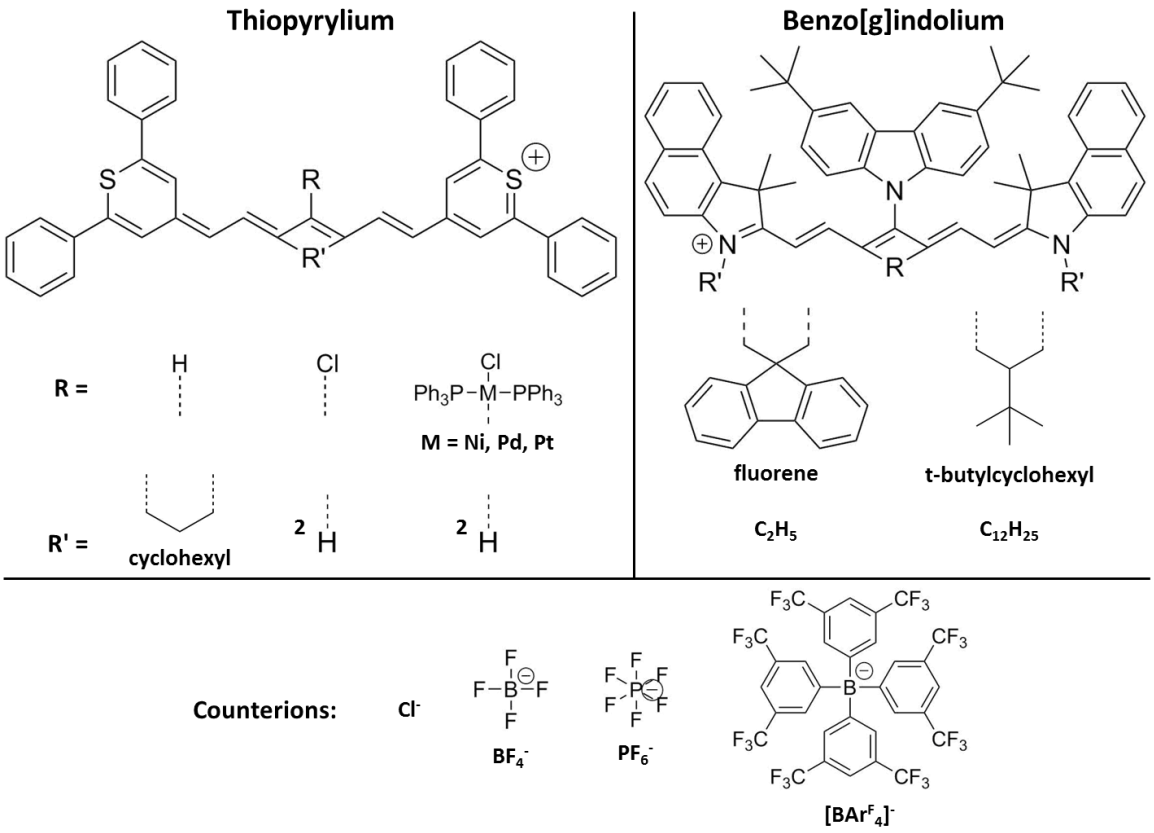

compound	backbone	R	R'	Counterion
1	thiopyrylium	–Cl	2 –H	–
2	thiopyrylium	$Ni(PPh_3)_2$	2 –H	–
3	thiopyrylium	$Pd(PPh_3)_2$	2 –H	–
4	thiopyrylium	$Pt(PPh_3)_2$	2 –H	–
5	thiopyrylium	–H	cyclohexyl	BF_4^-
6	thiopyrylium	–H	cyclohexyl	$[BAr^F{}_4]^-$
7	benzo[g]indolium	fluorene	C_2H_5	Cl^-
8	benzo[g]indolium	t-butylcyclohexyl	$C_{12}H_{25}$	PF_6^-
9	benzo[g]indolium	t-butylcyclohexyl	$C_{12}H_{25}$	$[BAr^F{}_4]^-$

Figure 3.1: List of compounds and chemical structures of cyanine dyes and counterions studied here.

3.2. Theoretical Methodology

3.2.1. Electronic Structure Calculations

Ground-state geometry optimizations were performed using DFT with the long-range corrected ωB97X-D functional[13-14] using the default range-separation parameter ω (ω = 0.2 Bohr^{-1}) and the cc-pVDZ basis set.[15] The cc-pVDZ basis sets for the Ni, Pd, and Pt atoms were taken from the EMSL Basis Set Exchange.[16-17] For comparison with experiment, the geometry optimizations were conducted by considering an implicit dielectric medium corresponding to chloroform (ε = 4.71) within the Polarizable Continuum Model (PCM). The absence of imaginary frequencies confirmed the geometries were at a global minimum. The molecular van der Waals volumes of the counterions were computed using multiwfn.

Symmetry Adapted Cluster Configuration Interaction (SAC-CI)[18-19] calculations (also performed in a chloroform-like medium) were used to obtain the vertical excited-state energies, transition dipole moments, and state dipole moments; since the SAC-CI active space incorporates single and higher-order excitations, it can correctly describe two-photon absorbing states, which is essential to accurately capture the molecular third-order NLO properties of cyanines. SAC-CI has previously been used to evaluate the excited-state properties for cyanines and dimers of cyanine/counterion complexes.[6] The chosen active space included the 40 highest-lying occupied orbitals and the 110 lowest-lying unoccupied orbitals, which were obtained at the Hartree-Fock/cc-pVDZ level of theory. The static ($\hbar\omega = 0$) third-order polarizabilities ($\gamma(\omega; \omega,-\omega, \omega)$) were obtained by a sum-over-states perturbation approach using the SAC-CI results as inputs for an essential-state calculation

involving 10 excited states. All electronic-structure calculations were performed in the Gaussian 09 (Rev. D.01) suite of programs.[20]

3.2.2. Molecular Dynamics Simulations of Amorphous Structures

3.2.2.1. Simulation Procedure

The molecular dynamics simulations and subsequent analyses of the cyanine-cyanine and cyanine-counterion geometries were conducted as detailed in references 10 and 21. In brief, the GROMACS 4.5.4 package[22] was used to conduct atomistic molecular dynamics (MD) simulations using the OPLS-AA force field.[23] This force field has previously shown good agreement with experiment for cyanine aggregates in solution.[24] The initial geometries of the isolated cyanines and counterions were obtained using the same level of theory without PCM as detailed above, with the atomic charges used in the MD simulations obtained from NBO calculations at the same level theory. Since *cis-trans* isomerization of the cyanines is not expected to occur in the films studied experimentally, all torsions about the C-C bonds in the polymethine backbone were constrained to within 10° of planarity to prevent isomerization during the high-temperature annealing. After generating an initial geometry by randomly placing cyanines and counterions in a periodic box, the energy was minimized at constant volume, and an initial run of 10 ps was performed at 50 K under the NVT ensemble. Following the initial run, the simulation box was equilibrated at 800 K under the NPT ensemble using the Berendsen barostat until the volume equilibrated, and then allowed to run for several additional ns. Several geometries at 1 ns intervals were extracted, and this series of amorphous geometries were equilibrated for 1 ns at the annealing

temperature using the Parrinello-Rahman barostat, cooled over 2 ns to 300 K, and finally simulated for 1 ns at 300 K. The following analyses exploited the final 1 ns of this simulation. The Nose-Hoover thermostat and periodic boundary conditions were used for all simulations, along with a time step of 1 fs; the Ewald summation was used for Coulomb interactions and the spherical cutoff for the summation of van der Waals interactions was set at 1.0 nm. The results were averaged over enough simulations to obtain a total of at least 1200 cyanine-counterion complexes.

3.2.2.2. Analysis of cyanine-counterion geometries

An internal coordinate system was defined to analyze the cyanine-counterion geometries. The origin **C** was set as the geometric center of the two hetero-atoms in the cyanine backbone. Vector $\vec{\boldsymbol{X}}$ was computed as the normalized vector from **C** to the first terminal hetero-atom, with vector $\vec{\boldsymbol{Y}}$ computed as the negative of the normalized component of a vector from **C** to the location of the central carbon atom orthogonal to $\vec{\boldsymbol{X}}$. The cross product of $\vec{\boldsymbol{X}}$ and $\vec{\boldsymbol{Y}}$ defined vector $\vec{\boldsymbol{Z}}$. Vector $\vec{\boldsymbol{D}}$ was defined as the vector from **C** to the counterion's central atom. The displacements along the internal axes ($\mathbf{D_x}$, $\mathbf{D_y}$, $\mathbf{D_z}$) were computed as the dot products of $\vec{\boldsymbol{D}}$ with $\vec{\boldsymbol{X}}$, $\vec{\boldsymbol{Y}}$, and $\vec{\boldsymbol{Z}}$. The cutoff distance for cyanine-counterion pairs was set at -20 Å to 20 Å along each axis and each pair within this cutoff was considered and sorted into bins with a width of 1 Å in each direction. For each simulation, the analysis was conducted for 501 frames at 2 ps intervals and the results averaged. The bulk density of the cyanine-counterion pairs was calculated as the product of the number of cyanines and the number of counterions in each frame divided by the average frame volume. Each bin was

normalized by dividing its count by the bin volume and the bulk density. Each X-Y displacement plot was constructed by averaging over a depth ranging from -5 Å to +5 Å along the z axis.

3.2.2.3. Analysis of cyanine-cyanine aggregate geometries

The positions of each atom at the end of the cyanine backbone were used to analyze the cyanine-cyanine aggregate geometries (Figure 3.2). Given each pair of cyanines (A and B), vectors $\vec{A}$ and $\vec{B}$ were defined between the two terminal atoms of each cyanine, respectively. The geometric centers of the cyanines, $\mathbf{C_A}$ and $\mathbf{C_B}$, were computed as the average position of the two terminal backbone atoms. Vector $\vec{C}$ was defined as the vector between $\mathbf{C_A}$ and $\mathbf{C_B}$. Vector $\vec{F}$, the offset, is the projection of $\vec{C}$ onto $\vec{A}$; vector $\vec{R}$, the radial distance, is the projection of $\vec{C}$ into the plane perpendicular to $\vec{A}$. The offset and the radial distance were computed as the magnitudes of vectors $\vec{F}$ and $\vec{R}$, respectively. The torsion angle was computed by determining vector $\vec{B'}$ as the projection of $\vec{B}$ into the plane perpendicular to $\vec{R}$, then computing the angle (D) between $\vec{A}$ and $\vec{B'}$. Since the two ends of the cyanine are identical, the torsion angle was computed as (180°-D) if D was greater than 90°. All ordered pairs of cyanines were considered, as the offset, radial distance, and torsion depend on whether cyanine A or B is chosen first. All cyanines pairs within a radial distance of 6 Å and an offset less than 12 Å were considered and sorted in bins of 1 Å offset and 10° torsion angle. Each bin count was normalized relative to the bulk density. The analysis was conducted for each simulation over 501 frames at 2 ps intervals and then averaged.

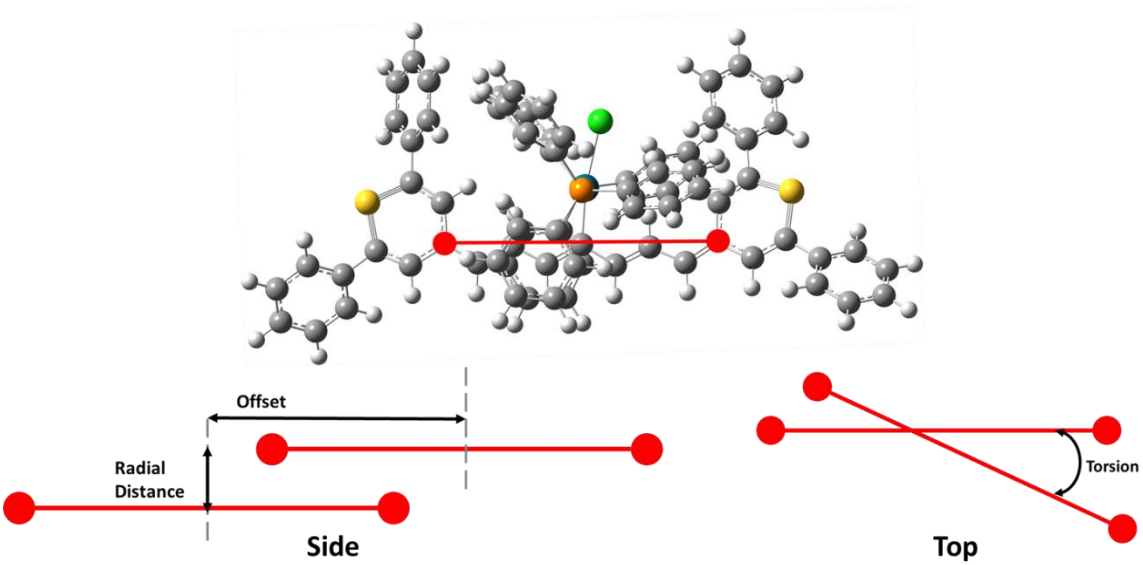

Figure 3.2: Atoms selected for analysis of cyanine aggregate geometries (top) and visualization of the analysis of cyanine-cyanine interaction geometries (bottom).

3.3. Results

The results in this Chapter are divided into two sections. In the first section, we focus on electronic-structure calculations of the M-functionalized thiopyrylium compounds, examining how the addition of the metallated substituent impacts the geometry, frontier MOs, excited states, and calculated static $\mathrm{Re}(\gamma)$. In the second section, we use molecular dynamics simulations to understand the interplay between the chemical structure and size of the cyanine and the size of counterion in cyanine-cyanine and counterion-cyanine packings.

3.3.1. Electronic Structure Results

We begin by examining the electronic structure and excited states of individual cyanines **1** – **4** in chloroform (ε=4.71) without the presence of a counterion as a function of metal center. Physical parameters, including BLA and dihedral angles (angles *a* and *b*, corresponding to the dihedral angles between the phosphines of the metal substituent and the thiopyrylium backbone) for the backbone and $M(PPh_3)_2Cl$ substituent, are presented in Table 3.1. The commonly-used definition of BLA for linear conjugated systems is not appropriate for use as a comparison here, as the geometries of the thiopyrylium cyanines are not expected to be significantly modified upon addition of the metallated substituents, remaining overly symmetric. Instead, we compute the *absolute average* BLA, which is the average of the absolute differences between successive carbon-carbon bond lengths along the cyanine backbone.

$$\text{Absolute Average BLA} = \frac{|b_{1-2} - b_{2-3}| + |b_{2-3} - b_{3-4}| + \cdots}{(N-2)} \tag{3.1}$$

where b_{x-y} is the bond length between atoms C_x and C_y, and N is the number of carbon atoms along the cyanine backbone.

Table 3.1: Physical properties of Cl-substituted (**1**) and $M(PPh_3)_2Cl$-substituted thiopyrylium cyanines (**2 – 4**) calculated in implicit solvent at the ωB97X-D/cc-pVDZ level of theory. C denotes the central carbon atom of the thiopyrylium backbone. Dihedral angles *a* and *b* correspond to the dihedral angles between the phosphines of the metal substituent and the thiopyrylium backbone.

	BLA (Å)	**dihedral *a* (°)**	**dihedral *b* (°)**	**backbone torsion (°)**	**M-C bond length (Å)**
1	0.0069	-	-	-4.7	-
2	0.019	92.8	88.9	-4.6	1.90
3	0.019	87.4	90.1	-15.2	2.01
4	0.024	89.9	89.5	-0.7	2.01

We highlight the unsubstituted thiopyrylium **1** for comparison, which shows the ideal cyanine geometry: negligible BLA and a largely planar backbone. As indicated above, for **2 – 4**, substitution at the central carbon atom with the $M(PPh_3)_2Cl$ substituent does not significantly impact the cyanine backbone or substituent geometries. The BLA increases slightly for **2** and **3**, while **4** shows the largest increase in BLA at ~0.024 Å. Despite these small increases in BLA, the M-functionalized thiopyrylium series largely retain their C_{2V} symmetry. While the backbone torsion angle generally remains small (< 5°), it is substantial (~15°) in the case of **3**; however, this larger torsion angle does not significantly impact the excited-state properties, which will be discussed shortly.

Similarly, the substituent geometry is not modified upon addition to the cyanine. Regardless of the identity of the metal, the metal center maintains a square planar geometry. The dihedral angles between the phosphines of the metal substituent and the thiopyrylium backbone (dihedrals *a* and *b*) are ca. 90°. Maintaining this square planar geometry confers an interesting advantage to the cyanine: the substituent straddles the cyanine backbone, with the phosphine groups overhanging on either side. Of the three

phenyl rings bonded to each phosphine atom, two are above the plane of the backbone, while the third lies within the plane of the backbone. The function of these bulky out-of-plane substituents can then be thought of as a "bumper" around the cyanine backbone, increasing cyanine-cyanine intermolecular distances. We note that while the Pd-C and Pt-C bond lengths are identical between **3** and **4**, the Ni-C bond length in **2** is shorter by ~0.1 Å.

As the OPA state and TPA state in cyanines involve excitations among the frontier MOs (HOMO-1, HOMO, LUMO, and LUMO+1), it is critical to investigate the impact the $M(PPh_3)_2Cl$ substituent has on these MOs, which we do next. Taking again the thiopyrylium **1** for reference, the MOs (Figure 3.3) are shown to be identical for a prototypical cyanine: the HOMO, HOMO-1, LUMO, and LUMO+1 are localized along the thiopyrylium backbone. We also take into consideration the HOMO-2 and the LUMO+2 when comparing the frontier orbitals, which will be shown to contain electron density from the substituent in **2 – 4**. In these two MOs, the density in the unsubstituted thiopyrylium is localized towards alternate ends of the backbone through the terminal phenyl rings.

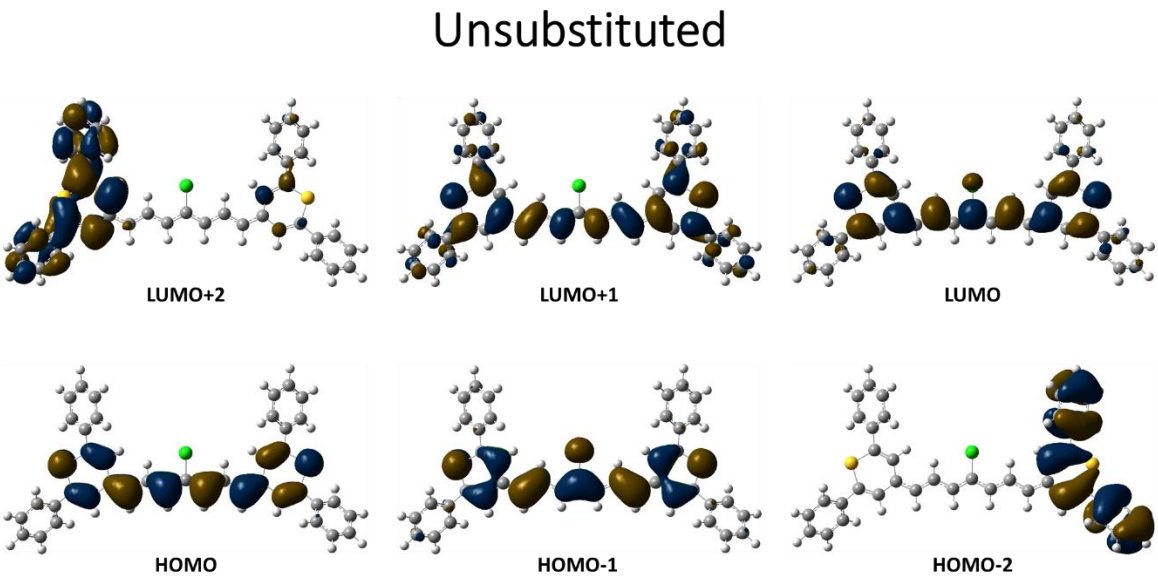

Figure 3.3: Molecular orbital plots of the frontier orbitals, including LUMO+2 and HOMO-2, for **1**, the unsubstituted thiopyrylium as calculated in implicit solvent at the ωB97X-D/cc-pVDZ level of theory.

In general for the series **2 – 4**, the addition of the $M(PPh_3)_2Cl$-substituent does not significantly alter the frontier MOs (see Figure 3.4, Figure 3.5, and Figure 3.6 for the MOs of compounds **2**, **3**, **4**, respectively). The HOMO, HOMO-1, LUMO, and LUMO+1 retain their unsubstituted cyanine-like character, being localized across the thiopyrylium cyanine. It is thus expected that any excitations among these orbitals will remain similar to the unsubstituted thiopyrylium, and will be local excitations based along the thiopyrylium backbone. Significant density on the substituent does not appear until the HOMO-2 and LUMO+2, in which case the density for the Pd and Pt systems resides predominantly on the substituent. As a node lies on the central carbon atom in the backbone in the HOMO and LUMO+1, the substituent can only interact electronically with the backbone *via* with the HOMO-1 and LUMO, as these two MOs have electron density on the backbone's central carbon atom. This electronic coupling between the cyanine backbone and the

substituent can be observed with density from the metal center d-orbitals appearing in the LUMO and HOMO-1; additionally, a minor contribution of density from the Cl atom in the substituent appears in the HOMO-1.

The frontier orbitals of the $Ni(PPh_3)_2Cl$-substituted thiopyrylium, shown in Figure 3.4, differ in character more than those of the Pd and Pt metal centered ones. In particular, in the HOMO-2 and LUMO+2 of **2**, the electron density is not restricted to the substituent. In the LUMO+2, the density on the substituent is present on the metal center and the phosphine atoms, delocalizing through the phenyl rings above the plane of the thiopyrylium backbone; additional density is also delocalized through the terminal phenyl rings at *both* molecular ends, and into the molecular center of the thiopyrylium cyanine through the substituent. In the HOMO-2, while the electron density is concentrated primarily on the center of the substituent and through all substituent phenyl rings, density slightly extends into the center of the backbone through the central carbon atom.

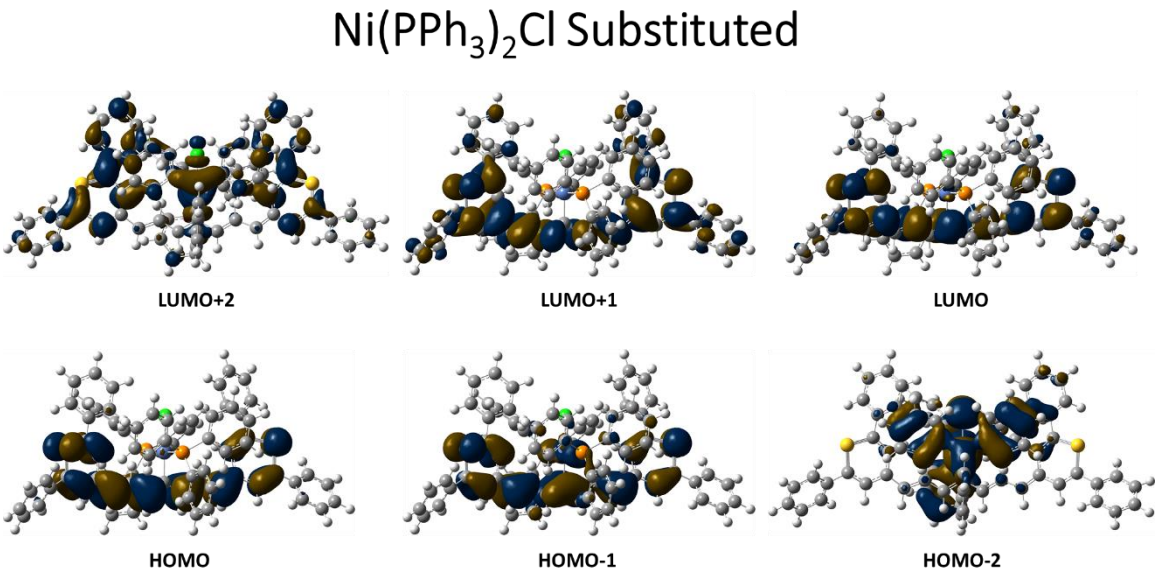

Figure 3.4: Molecular orbital plots of the frontier orbitals, including LUMO+2 and HOMO-2, for **2**, the $Ni(PPh_3)_2Cl$-substituted thiopyrylium, as calculated in implicit solvent at the ωB97X-D/cc-pVDZ level of theory.

The LUMO+2 and HOMO-2 in **3** and **4** (Figure 3.5 and Figure 3.6, respectively) are similar with respect to each other. Concerning the HOMO-2, it is localized exclusively on the metallated substituent in both compounds, being composed of orbitals centered on the metal, chlorine, and phosphine atoms, along with density primarily on the phenyls that are in the plane of the backbone. For **4**, the LUMO+2 is a combination of the unsubstituted thiopyrylium LUMO+2 and the substituent-centered orbitals (with some density on the backbone central carbon atom). However, for **3**, the LUMO+2 is identical to the unsubstituted thiopyrylium LUMO+2, and no density is present on the substituent. Indeed, with the $Pt(PPh_3)_2Cl$ substituent, the LUMO+2 and the LUMO+3 remain thiopyrylium-like, being localized on the thiopyrylium terminal phenyl rings and backbone, and density from the substituent does not appear until the LUMO+4. Thus, the Pt-based substituent has the smallest impact on the thiopyrylium orbitals in the metallated cyanines.

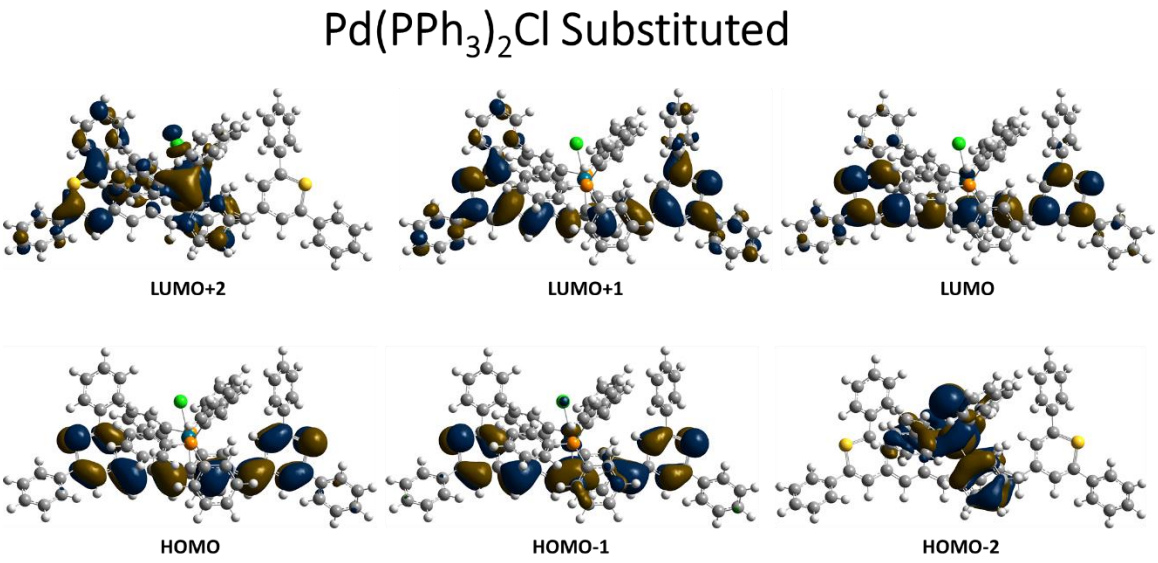

Figure 3.5: Molecular orbital plots of the frontier orbitals, including LUMO+2 and HOMO-2, for **3**, the $Pd(PPh_3)_2Cl$-substituted thiopyrylium, as calculated in implicit solvent at the ωB97X-D/cc-pVDZ level of theory.

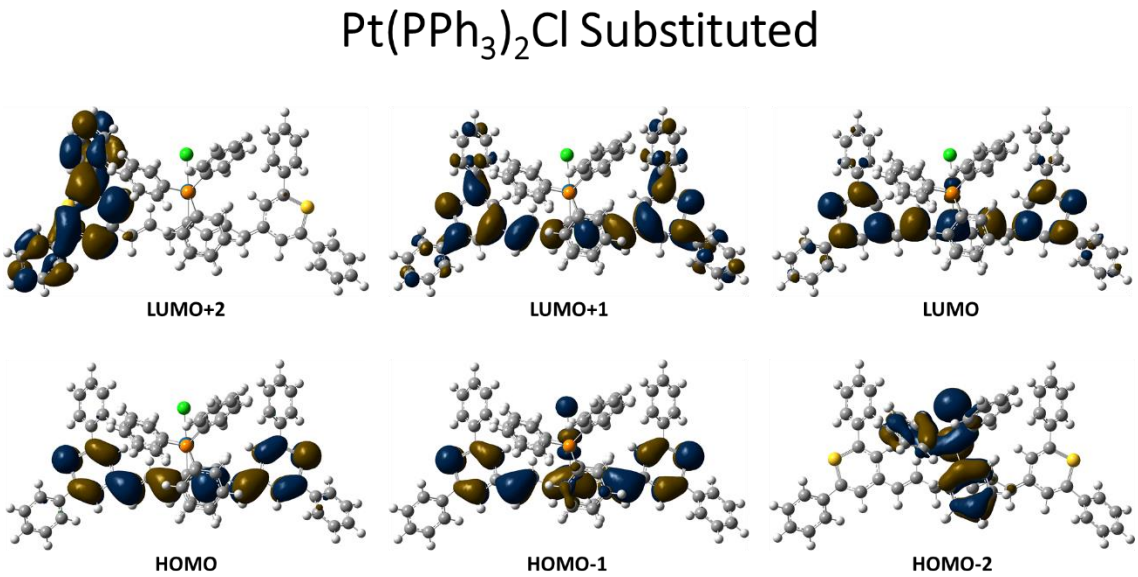

Figure 3.6: Molecular orbital plots of the frontier orbitals, including LUMO+2 and HOMO-2, for **4**, the $Pd(PPh_3)_2Cl$-substituted thiopyrylium, as calculated in implicit solvent at the ωB97X-D/cc-pVDZ level of theory.

The frontier MO energies are plotted in Figure 3.7 as a function of metal center identity. In general, the addition of the $M(PPh_3)_2Cl$ substituent destabilizes all frontier MOs. The HOMO-1 and the HOMO-2 are destabilized the most, by ca. 0.6 eV, due to the addition of density from the metal center in the HOMO-1 and the replacement of the thiopyrylium orbital with the substituent-centered orbital in the HOMO-2. Since the HOMO has a node on the central carbon atom, the addition of the substituent barely disturbs the orbital and its energy. The situation, however, is different in the LUMO: the LUMO energy is destabilized, and this increase in energy broadens the HOMO-LUMO gap by ca. 0.3 eV for each metallated cyanine as compared to the unsubstituted thiopyrylium. This is consistent with the fact that experimentally the maximum absorption peak for metallated cyanines are blue-shifted compared to unsubstituted cyanines.[12] There are only minor differences among the LUMO+1 and the LUMO+2 energies from the unsubstituted to metallated thiopyrylium. Among the metallated thiopyrylium cyanines with different metal centers, the frontier MO energies vary slightly as a function of metal identity.

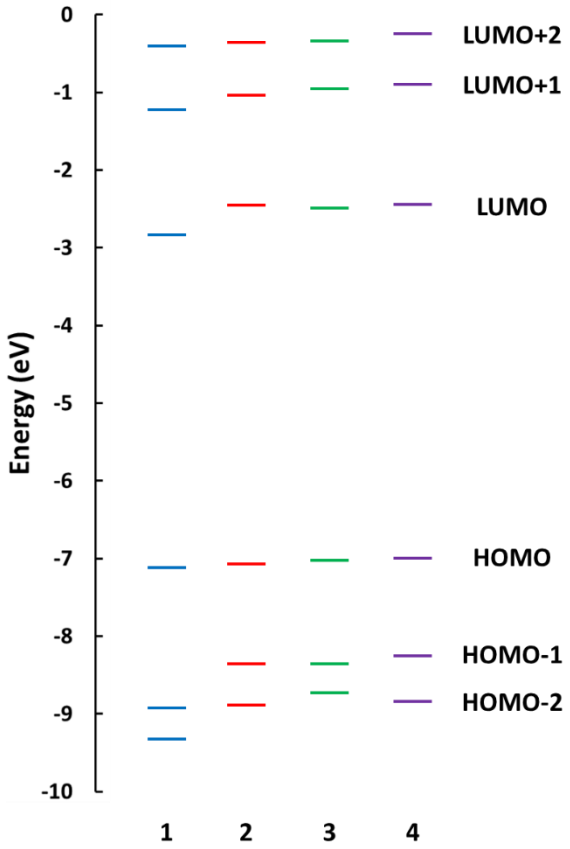

Figure 3.7: Frontier molecular orbital energies for the unsubstituted (**1**) and the $M(PPh_3)_2Cl$-substituted (**2 – 4**) thiopyrylium cyanines as calculated in implicit solvent at the ωB97X-D/cc-pVDZ level of theory.

The subtle differences in the M-C bond length and frontier MOs among the metal center series give rise to a different excited-state picture compared to **1**, as seen in Figure 3.8. Table 3.2 collects the vertical excitation energies for the OPA and TPA states, transition dipole moments between ground and OPA state, transition dipole moments between OPA and TPA state, and CI decompositions for each state, as computed at the SAC-CI level of theory. The excited-state energies are relatively insensitive to the identity of the metal atom in the substituted thiopyrylium cyanines (**2 – 4**).

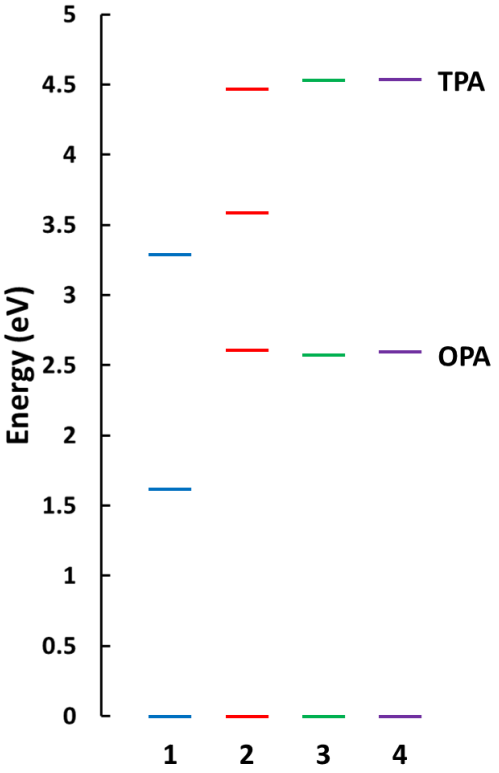

Figure 3.8: Evolution of OPA and TPA excited states upon addition of the $M(PPh_3)_2Cl$ substituent as calculated in implicit solvent at the SAC-CI/HF/cc-pVDZ level of theory.

The most significant change for the series **2** – **4** as compared to **1** is the blue-shift of the OPA and TPA vertical excitation energies in the $M(PPh_3)_2Cl$-substituted thiopyrylium cyanines. For the OPA state energy, this destabilization amounts to nearly 1 eV, regardless of the identity of the metal, while the TPA state energy destabilization is ca. 1.2 eV. This has the noteworthy consequence of leading to a slight broadening of the OPA-TPA energy window for the metallated thiopyrylium cyanines **3** and **4**. Most significant is the appearance of a *new excited state* in compound **2** (denoted E_{S2} in Table 3.2). This new state, which will be described in more detail below, is strongly TPA, appears in the middle of the OPA-TPA energy window, and is only 0.3 eV above the OPA; for **2**, this new excited state closes down the energetic window.

Table 3.2: Vertical excitation energies for OPA and TPA states (eV), transition dipole moments between the ground and OPA state (μ_{ge}, Debye) and between OPA and TPA state ($\mu_{ee'}$ (Debye)) for the unsubstituted (**1**) and $M(PPh_3)_2Cl$-substituted (**2 – 4**) thiopyrylium cyanines as calculated in implicit solvent at the SAC-CI/HF/cc-pVDZ level of theory. For each state, its CI decomposition is listed; H denotes HOMO and L denotes LUMO. E_{S_2} in compound **2** corresponds to the new TPA state.

	1	**2**	**3**	**4**
$\mathbf{E_{OPA}}\,(\boldsymbol{\mu_{ge}})$	1.62 (*22.39*)	2.61 (*17.39*)	2.57 (*18.38*)	2.59 (*18.64*)
CI composition	$0.92\|H \rightarrow L\rangle$	$0.95\|H \rightarrow L\rangle$	$0.95\|H \rightarrow L\rangle$	$0.95\|H \rightarrow L\rangle$
$\mathbf{E_{S2}}\,(\boldsymbol{\mu_{eE_{S_2}}})$		3.59 (*13.35*)		
CI composition		$0.60\|H-1 \rightarrow L\rangle$ $-0.42\|H \rightarrow L+1\rangle$ $-0.53\|H,H \rightarrow L,L\rangle$		
$\mathbf{E_{TPA}}\,(\boldsymbol{\mu_{ee'}})$	3.28 (*14.93*)	4.47 (*16.94*)	4.52 (*14.45*)	4.54 (*15.57*)
CI composition	$-0.53\|H-1 \rightarrow L\rangle$ $-0.49\|H \rightarrow L+1\rangle$ $-0.52\|H,H \rightarrow L,L\rangle$	$-0.68\|H-1 \rightarrow L\rangle$ $-0.59\|H \rightarrow L+1\rangle$ $0.26\|H,H \rightarrow L,L\rangle$	$-0.66\|H-1 \rightarrow L\rangle$ $0.59\|H \rightarrow L+1\rangle$ $0.30\|H,H \rightarrow L,L\rangle$	$0.66\|H-1 \rightarrow L\rangle$ $-0.57\|H \rightarrow L+1\rangle$ $-0.33\|H,H \rightarrow L,L\rangle$

The two (or in the case of compound **2**, three) lowest singlet excited states were examined, and the description of each state is collected in Table 3.2. In all cases for compounds **1** – **4**, we find that the first singlet excited state corresponds to the OPA state, with its electronic transition predominately (~90%) a local excitation centered on the thiopyrylium backbone. With the exception of compound **2**, the second excited state corresponds to the TPA state, with three local excitations centered on the thiopyrylium backbone composed of a $|HOMO-1 \rightarrow LUMO\rangle$, a $|HOMO \rightarrow LUMO+1\rangle$, and a double $|HOMO \rightarrow LUMO\rangle$ transition. For **2** (with the Ni metal), the new second excited state (denoted E_{S_2}) and the third excited state are both a TPA state, described by the same three local excitations centered on the thiopyrylium backbone. The excited-state transition dipole moment from the OPA state to both TPA states ($\mu_{ee'}$) are similar in magnitude for state E_{S_2} and E_{TPA} in **2**. For the $M(PPh_3)_2Cl$-substittued thiopyrylium cyanines, we note that the ground to OPA

state transition dipole moment (μ_{ge}) becomes reduced by ~4 Debye compared to the unsubstituted thiopyrylium, but the magnitude does not greatly depend on the identity of the metal.

Table 3.3: Re(γ_{static}) and its decomposition into the three-term model, reported in 10^{-33} esu.

	Re(γ_{static}) (10^{-33} esu)	**D-term**	**T-term**	**N-term**
1	-29.9	0.136	38.1	-68.2
2	0.141	0.0243	6.08	-5.97
3	-4.54	0.192	3.07	-7.79
4	-4.61	0.0121	3.42	-8.04

The smaller μ_{ge} and larger OPA state energy in the metallated thiopyrylium cyanines lead to a reduction in the magnitude of Re(γ_{static}) by an order of magnitude for **2-4** as compared to **1** (see **Table 3.3**). For compounds **3** and **4**, Re(γ_{static}) remains large and negative, as the **N** term dominates the three-term expression. In compound **2**, however, Re(γ_{static}) has become small (as compared with the rest of the series) and takes on a positive value due to a slight reduction in the magnitude of the **N** term and a large increase in the magnitude of the **T** term, which nearly cancel each other out. Indeed, the **T** term is twice as large in **2** as compared to compounds **3** and **4**. This suggests that the FOM for **2** is unacceptable for use in AOS devices due to the combination of small and positive Re(γ_{static}) and increased losses due to TPA. We note that the predicted dependence and trend of Re(γ_{static}) on the identity of the metal atom is in line with what has been observed experimentally in the Marder group.[25]

3.3.2. Molecular Dynamics Results

Having described how the addition of the large $M(PPh_3)_2Cl$ substituent impacts the molecular properties of interest for NLO, we now turn to a discussion of atomistic MD simulations in order to understand the substituent's impact on cyanine-cyanine aggregation and cyanine-counterion geometries. Previous MD simulations conducted on amorphous cyanine/counterion bulk systems revealed that substitution at the molecular ends and/or at the molecular center on the cyanine backbone can play a key role in reducing aggregation, and that increasing the bulk of the cyanine backbone by attaching bulky groups to the molecular ends is an effective strategy to minimize aggregation.[10] Here, we seek to investigate: (1) the impact the $Pd(PPh_3)_2Cl$-substituent (compound **3**) has on the packing of thiopyrylium cyanines in an amorphous solid; and (2) the interplay between cyanine size and counterion size in influencing cyanine/cyanine and cyanine/counterion geometries in experimentally relevant cyanines. We consider two cyanine backbones: (1) the thiopyrylium cyanine with the large bulky $Pd(PPh_3)_2Cl$ substituent in the center and moderate bulk at the molecular ends; and (2) a benzo[g]indolium cyanine, which has a moderately bulky substituent at the molecular center. Each cyanine is paired with counterions of increasing size.

3.3.2.1 Effect of $Pd(PPh_3)_2Cl$ substituent on cyanine/cyanine and cyanine/counterion geometries

To examine the impact the addition of a large bulky substituent to the molecular center of the cyanine has on cyanine/cyanine and cyanine/counterion geometries, we consider the

unsubstituted thiopyrylium with the BF_4^- (compound **5**) and $[BAr^F{}_4]^-$ (compound **6**) counterions and the substituted thiopyrylium with the $Pd(PPh_3)_2Cl$ substituent with the small, hard Cl^- counterion (compound **3**). Compounds **5** and **6** are molecules that exemplify the messages from previous MD studies for maintaining solution-like cyanine properties, as their molecular structures consist of large groups at the molecular ends and large, soft counterions. Figure 3.9 shows the probabilities of finding cyanine-cyanine pairs in aggregate geometries (top) and the counterion most probable positions relative to the cyanine (bottom).

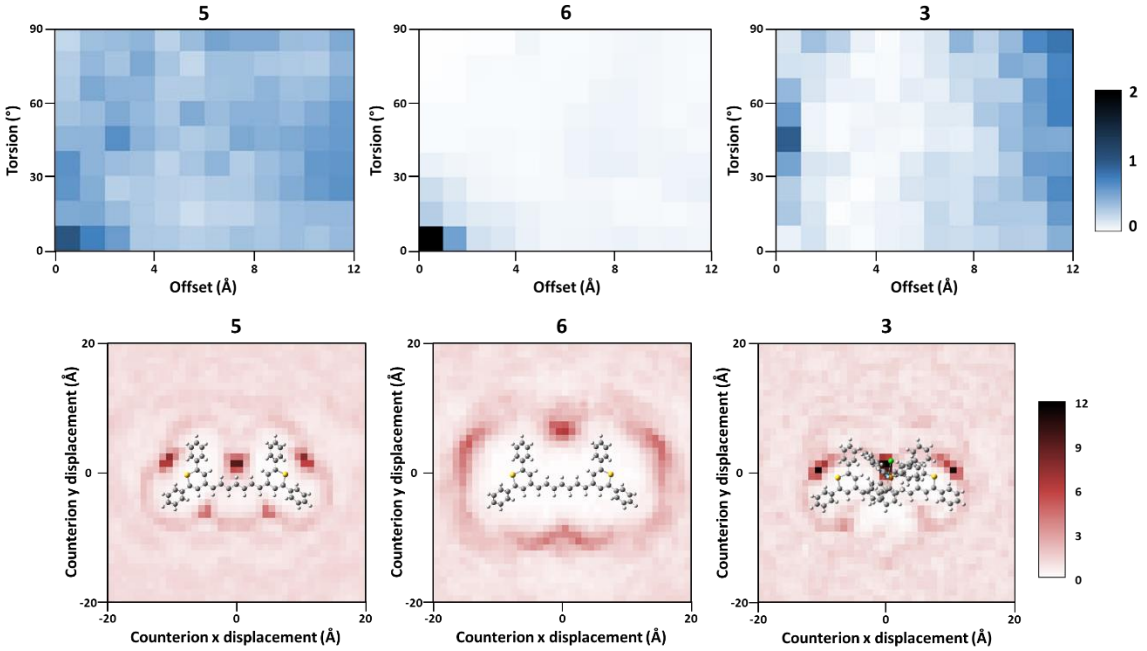

Figure 3.9: Cyanine-cyanine geometries (top) and cyanine-counterion geometries (bottom) for thiopyrylium cyanines **5**, **6**, and **3**. The color scale corresponds to the probability of finding pairs, with a probability of 1 corresponding to the average bulk density of cyanine−counterion pairs. The superimposed cyanine images represent the orientation and scale of the molecule.

The bulkiness of the cyanine and counterion complement each other to reduce cyanine-cyanine aggregation. Given the unsubstituted thiopyrylium, a variety of aggregate geometries are possible for the smaller BF_4^- counterion (**5**). When paired with the significantly larger $[BAr^F{}_4]^-$ counterion (**6**), all other aggregate geometries besides parallel geometries with small offsets are suppressed, as denoted by the majority of white in the probability plot for **6** (top). In **6**, the increased probabilities for parallel geometries with small torsion angles implies π-stacking through the planar terminal phenyl rings, and indeed in **5** the tendency for π-π stacking can be observed with the slightly larger probability at parallel geometries with short offsets. The size of the $[BAr^F{}_4]^-$ counterion can therefore disrupt aggregation when it is able to pack between adjacent cyanine backbones, but by virtue of its size can also enhance aggregate geometries intrinsic to a cyanine by not being able to pack between all cyanine pairs. Given the unsubstituted thiopyrylium with terminal phenyl rings, we should expect the cyanine to have a predilection for π-π stacking, leading to electronic coupling between such molecules. More generally, such a dependence of aggregation on counterion size has been observed experimentally.[26]

Since large, bulky counterions can aid in reducing cyanine-cyanine aggregation, pairing the metallated thiopyrylium with the small, hard Cl^- counterion allows us to directly assess the ability of the $Pd(PPh_3)_2Cl$ substituent to aid in minimizing cyanine-cyanine aggregation as the small Cl^- counterion is expected to contribute minimally to preventing aggregation. The addition of the $Pd(PPh_3)_2Cl$ substituent in **3** prevents most aggregate geometries (far right plot in Figure 3.9), especially those with small parallel offsets. The $Pd(PPh_3)_2Cl$ substituent, however, increases the probability of finding geometries with short offsets and

large torsion angles, implying an increase in 45° aggregate geometries between two thiopyrylium cyanines. The addition of a significantly large substituent to the center of the thiopyrylium is thus an effective strategy to minimize cyanine-cyanine aggregation, and can overcome the stacking motifs preferred by unsubstituted thiopyrylium cyanines.

The size of the counterion can be seen to influence the degree of counterion localization along the cyanine backbone. The BF_4^- counterion, which has a molecular van der Waals volume of 64.8 $Å^3$, has an increased probability of localizing more towards the center of the thiopyrylium and near the sulfur atoms, where it is sterically accessible and electrically favored. On the other hand, the significantly larger $[BAr^F_4]^-$ counterion, with a volume of 708.8 $Å^3$, occupies similar yet broader positions to the BF_4 counterion, owing to its larger bulk. The 10 times increase in molecular volume between the BF_4 and $[BAr^F_4]^-$ counterions leads to an increase the backbone-$[BAr^F_4]^-$ distance by an average of 5 Å in the x-displacement and an average of 3 Å in the y-displacement. The large $Pd(PPh_3)_2Cl$ substituent, with its phenyl groups which overhang the sides of the backbone, limits the counterion to near the sulfur atoms exclusively, as the thiopyrylium termini are the only sterically-accessible areas the counterion can approach. We note that the larger probability for finding a chloride ion located at the molecular center in compound **3** (Figure 3.9, bottom, far right) is a spurious effect and does not represent an increased probability of finding a counterion at that position. Instead, the increased probability is related to the presence of the chlorine atom contained within the $Pd(PPh_3)_2Cl$ substituent. As our analysis script does not distinguish between the chloride counterion and the substituent chlorine atom, we see an increased probability at the molecular center which is related to the molecular composition of the substituent.

3.3.2.2. Role of Counterion in Cyanines Designed to Minimize Aggregation

While increasing the counterion size can aid in reducing random cyanine-cyanine aggregate geometries, an increase in the steric bulk of the counterion can lead to a reduction in the concentration of molecules in neat films, especially when the accompanying cyanines are large themselves. Thin films of benzo[g]indolium cyanines designed to minimize aggregation, by incorporating steric bulk along the cyanine backbone, present absorption spectra similar to the absorption spectra of the cyanines in dilute solutions when paired with counterions larger than Cl^-.[25] In this section, we seek to understand whether or not the identity of the counterion matters when paired with cyanines designed to minimize aggregation. The cyanine-cyanine and cyanine-counterion geometry probability plots as a function of increasing counterion size are shown in Figure 3.10.

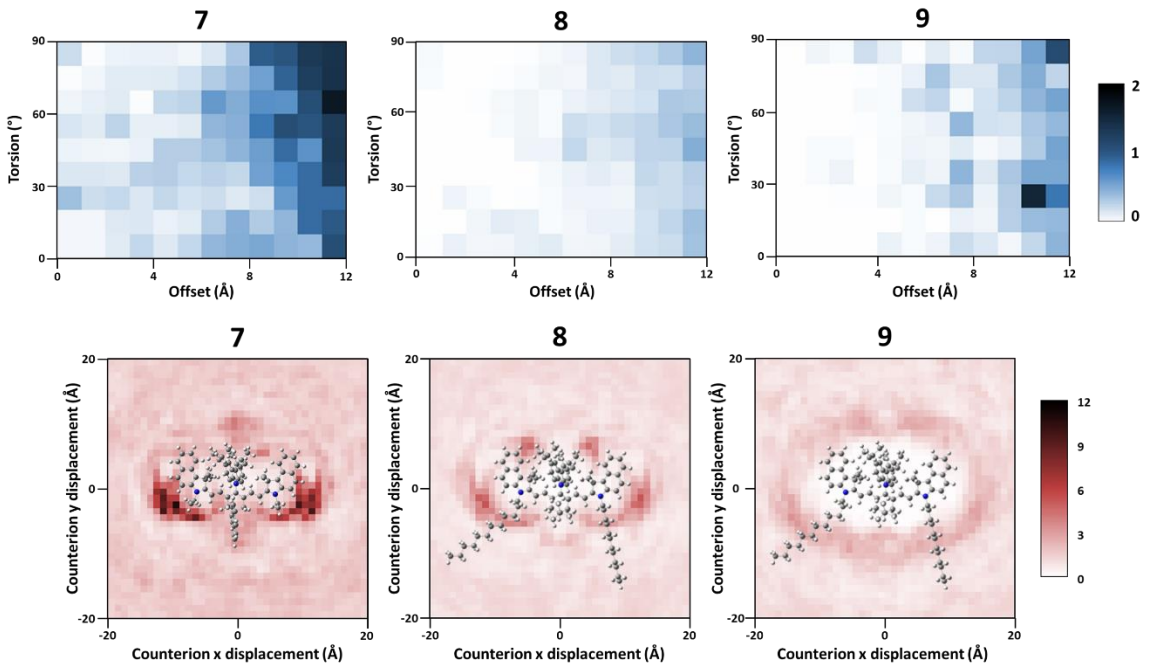

Figure 3.10: Cyanine-cyanine geometries (top) and cyanine-counterion geometries (bottom) for benzo[g]indolium compounds **7**, **8**, and **9**. The color scale corresponds to the probability of finding pairs, with a probability of 1 corresponding to the average bulk density of cyanine−counterion pairs. The superimposed cyanine images represent the orientation and scale of the molecule.

The MD simulation results for compound **7** (Figure 3.10**)** show that the benzo[g]indolium structure, with moderate bulk at the molecular ends and center, inherently leads to fewer aggregate geometries with respect to the unsubstituted thiopyrylium **5**; the probabilities for finding aggregate geometries below an offset of 4 Å are small (white areas), particularly for the parallel offsets observed with **5**. Since this cyanine is paired with the small hard Cl^- counterion, the decrease in probability of aggregate geometries, especially compared to **5**, can be attributed to the general increase in steric bulk along the benzo[g]indolium backbone, which limits the ability of the backbones to approach one another. Further reduction in aggregate geometry probabilities is obtained by pairing the benzo[g]indolium with the slightly larger PF_6^- counterion in **8**, especially for geometries at offset distances

greater than 8 Å. However, no further significant improvement in reducing the aggregate geometry probabilities is obtained when pairing with the large $[BAr^F{}_4]^-$ counterion in **9**. This trend suggests that once sufficient bulk has added to the cyanine backbone, a bulky counterion beyond a certain size (for the benzo[g]indolium series, the threshold size would be greater than PF_6^-) is ineffective at further reducing aggregate geometry formation.

While increasing the counterion size has diminishing improvement on minimizing cyanine-cyanine aggregates, the size of the counterion critically influences the cyanine-counterion ion pairing. The smaller, harder counterions (*e.g.*, Cl^-) exclusively localize towards the sterically-accessible terminal nitrogen atoms to be near the positive charge on the cyanine backbone. As the counterion size is increased (from PF_6^- to $[BAr^F{}_4]^-$), the counterion occupies increasingly broader and more distant positions along the benzo[g]indolium backbone, as indicated by the smearing of the probabilities in space near the terminal N atoms in **8** and the ring of increased probability around the backbone in **9**. For the $[BAr^F{}_4]^-$ counterion, its most probable positions are smeared out with approximately equal probabilities around the backbone. An average increase of 2 Å in both the x- and y-displacements for the region with highest counterion probability is obtained upon pairing with the next larger counterion, such that the average center-to-center distance from the counterion to the backbone in the XY-plane is 9.5 Å for Cl^- and is 13.9 Å for $[BAr^F{}_4]^-$.

Cyanines are able to undergo symmetry breaking through ion-pairing with the counterions, and a counterion contribution to symmetry breaking is expected to be maximized when it is localized near one end of the cyanine backbone.[5-6] Thus, even though the optimized cyanine structure limits aggregation, significant symmetry-breaking is anticipated with the Cl^- counterion, which could negatively impact the cyanine advantageous individual

electronic properties. Increasing counterion size increases the average cyanine-counterion distance and broadens the possible counterion positions along the benzo[g]indolium backbone, and the counterion ability to ion-pair with the cyanine backbone is reduced. It is likely that because of the broadness of counterion positions with increased probability along the cyanine backbone that the cyanines exist in various degrees of symmetry brokenness in thin films. This is particularly likely in the case of PF_6^-, which is large enough to avoid localizing entirely near the terminal N atoms (like Cl^-), yet is still small enough to approach closer to the cyanine backbone than $[BAr^F{}_4]^-$ is capable of doing.

3.4. Conclusions

In this Chapter, we have carried out dual investigations on two types of large bulky cyanines whose geometries were designed to minimize aggregation in the solid state. First, we investigated a thiopyrylium cyanine with the $M(PPh_3)_2Cl$ (M= Ni, Pd, Pt) substituent attached to the central carbon atom, focusing on what effect the addition of a metallated substituent has on the electronic structure and third-order response of the thiopyrylium. Next, we used MD simulations to understand: (1) the effect the $Pd(PPh_3)_2Cl$ substituent has on cyanine-cyanine aggregation in the solid state; and (2) the interplay between cyanine and counterion structures in cyanine-counterion packing, using a benzo[g]indolium cyanine designed to minimize aggregation.

The addition of the $M(PPh_3)_2Cl$ substituent destabilizes the excited-state energies and reduces the transition dipole moments, which leads to a reduction in the magnitude of $\mathrm{Re}(\gamma)$ compared to the unsubstituted thiopyrylium. The identity of the metal atom can play

a critical role in determining the NLO properties. Among the systems we have studied, Ni introduces a new excited state within the optical window between the first and second excited states, and in this molecule $\mathrm{Re}(\gamma)$ is positive and small. Pd and Pt are similar with respect to each other, with their frontier orbitals and excited-state spacing look unsubstituted cyanine-like, and $\mathrm{Re}(\gamma)$ is negative and large in both compounds.

We have used MD simulations to investigate experimentally-relevant cyanines with additional bulk at locations corresponding to either (1) moderate bulk at the molecular ends and center or (2) significant bulk at the molecular center. Aggregate geometry formation is reduced in these cyanines. In the case of the $Pd(PPh_3)_2Cl$-substituent, the large substituent in the center of the backbone can overcome the tendency of the cyanine to aggregate in specific geometries inherent to its molecular structure (*i.e.*, disrupt π-π stacking through the terminal phenyl rings). Increasing the counterion size can aid in reducing the uncontrolled cyanine-cyanine aggregation, but also can promote aggregate configurations triggered by the specifics of the molecular geometry. This suggests that a judicious selection of cyanine and counterion can provide a means to control the formation of aggregate geometries. However, once the cyanine structure has been optimized to reduce aggregation and has been paired with a counterion of sufficient bulkiness, no further reduction in aggregate geometry formation is obtained by going to a larger counterion. Critically, the size of the counterion determines the extent that the counterion can approach the cyanine backbone and the degree of localization near cyanine molecular end, with larger, bulky counterions being sterically prohibited from approaching closely and occupying broader positions along the cyanine backbone. The broad range of counterion positions near the cyanine backbone, particularly for counterions of medium size like

PF_6^-, suggest that cyanines in the solid state exist in various degrees of symmetry-brokenness.

3.5. References

1. Hales, J. M.; Barlow, S.; Kim, H.; Mukhopadhyay, S.; Brédas, J.-L.; Perry, J. W.; Marder, S. R. Design of organic chromophores for all-optical signal processing applications. *Chem. Mater.* **2014,** *26*, 549-560.

2. Belfield, K. D.; Bondar, M. V.; Hernandez, F. E.; Przhonska, O. V.; Yao, S. Two-photon absorption of a supramolecular pseudoisocyanine J-aggregate assembly. *Chem. Phys.* **2006,** *320*, 118-124.

3. Busse, G.; Frederichs, B.; Petrov, N. K.; Techert, S. Structure determination of thiacyanine dye J-aggregates in thin films: Comparison between spectroscopy and wide angle X-ray scattering. *Phys. Chem. Chem. Phys.* **2004,** *6*, 3309-3314.

4. Gadde, S.; KBatchelor, E. K.; Weiss, J. P.; Ling, Y.; Kaifer, A. E. Control of h- and j-aggregate formation via host-guest complexation using cucurbituril hosts. *J. Am. Chem. Soc.* **2008,** *130*, 17114-17119.

5. Bouit, P.-A.; Aronica, C.; Toupet, L.; Le Guennic, B.; Andraud, C.; Maury, O. Continuous symmetry breaking induced by ion pairing effect in heptamethine cyanine dyes: Beyond the cyanine limit. *J. Am. Chem. Soc.* **2010,** *132*, 4328-4335.

6. Mukhopadhyay, S.; Risko, C.; Marder, S. R.; Brédas, J.-L. Polymethine dyes for all-optical switching applications: a quantum-chemical characterization of counter-ion and aggregation effects on the third-order nonlinear optical response. *Chem. Sci.* **2012,** *3*, 3103-3112.

7. Bambgelu, A.; Wang, J.; Leszczynski, J. TDDFT study of the optical properties of cy5 and its derivatives. *J. Phys. Chem. A* **2010,** *114*, 3551-3555.

8. Karaman, R.; Menger, F. M. Electrostatic effects on the energetics and geometry of a cyanine dye. *J. Mol. Struct.: THEOCHEM* **2010,** *959*, 87-91.

9. Scarpaci, A.; Nantalaksakul, A.; Hales, J. M.; Matichak, J. D.; Barlow, S.; Rumi, M.; Perry, J. W.; Marder, S. R. Effects of dendronization on the linear and third-order nonlinear optical properties of bis(thiopyrylium) polymethine dyes in solution and the solid state. *Chem. Mat.* **2012,** *24*, 1606-1618.

10. Gieseking, R. L.; Mukhopadhyay, S.; Risko, C.; Marder, S. R.; Bredas, J. L. Design of organic chromophores for all-optical signal processing applications. *Chem. Mater.* **2014,** *26*, 6439.

11. Barlow, S.; Brédas, J.-L.; Getmanenko, Y. A.; Gieseking, R. L.; Hales, J. M.; Kim, H.; Marder, S. R.; Perry, J. W.; Risko, C.; Zhang, Y. Polymethine materials with solid-state third-order optical susceptibilities suitable for all-optical signal-processing applications. *Mater. Horiz.* **2014,** *1*, 577-581.

12. Davydenko, I.; Barlow, S.; Sharma, R.; Benis, S.; Simon, J.; Allen, T. G.; Cooper, M. W.; Khrustalev, V.; Jucov, E. V.; Castaneda, R.; Ordonez, C.; Li, Z.; Chi, S.-H.; Jang, S. H.; Parker, T. C.; Timofeeva, T. V.; Perry, J. W.; Jen, A. K.-Y.; Hagan, D. J.; Van Stryland, E. W.; Marder, S. R. Facile incorporation of Pd(PPh3)2 hal substituents into polymethines, merocyanines, and perylene diimides as a means of suppressing intermolecular interactions. *J. Am. Chem. Soc.* **2016,** *138*, 10112-10115.

13. Chai, J.-D.; Head-Gordon, M. Long-range corrected hybrid density functionals with damped atom–atom dispersion corrections. *Phys. Chem. Chem. Phys.* **2008,** *10*, 6615-6620.

14. Chai, J.-D.; Head-Gordon, M. Systematic optimization of long-range corrected hybrid density functionals. *J. Chem. Phys.* **2008,** *128*, 084106.

15. Dunning, T. H. Gaussian basis sets for use in correlated molecular calculations. I. The atoms boron through neon and hydrogen. *J. Chem. Phys.* **1989,** *90*, 1007-1023.

16. Feller, D. The role of databases in support of computational chemistry calculations. *J. Comp. Chem.* **1996,** *17*, 1571–1586.

17. Schuchardt, K. L.; Didier, B. T.; Elsethagen, T.; Sun, L.; Gurumoorthi, V.; Chase, J.; Li, J.; Windus, T. L. Basis Set Exchange: A community database for computational sciences. *J. Chem. Inf. Model.* **2007,** *47*, 1045-1052.

18. Nakatsuji, H.; Hirao, K. Cluster expansion of the wavefunction. Symmetry-adapted-cluster expansion, its variational determination, and extension of open-shell orbital theory. *J. Chem. Phys.* **1978,** *68*, 2053-2065.

19. Nakano, M. Cluster expansion of the wavefunction. Excited states. *Chem. Phys. Lett.* **1978,** *59*, 362-364.

20. Gaussian 09, R. D.; M. J. Frisch, G. W. T., H. B. Schlegel, G. E. Scuseria, ; M. A. Robb, J. R. C., G. Scalmani, V. Barone, B. Mennucci, ; G. A. Petersson, H. N., M. Caricato, X. Li, H. P. Hratchian, ; A. F. Izmaylov, J. B., G. Zheng, J. L. Sonnenberg, M. Hada, ; M. Ehara, K. T., R. Fukuda, J. Hasegawa, M. Ishida, T. Nakajima, ; Y. Honda, O. K., H. Nakai, T. Vreven, J. A. Montgomery, Jr., ; J. E. Peralta, F. O., M. Bearpark, J. J. Heyd, E. Brothers, ; K. N. Kudin, V. N. S., T. Keith, R. Kobayashi, J. Normand, ; K. Raghavachari, A. R., J. C. Burant, S. S. Iyengar, J. Tomasi, ; M. Cossi, N. R., J. M. Millam, M. Klene, J. E. Knox, J. B. Cross, ; V. Bakken, C. A., J. Jaramillo, R. Gomperts, R. E. Stratmann, ; O. Yazyev,

A. J. A., R. Cammi, C. Pomelli, J. W. Ochterski, ; R. L. Martin, K. M., V. G. Zakrzewski, G. A. Voth, ; P. Salvador, J. J. D., S. Dapprich, A. D. Daniels, ; O. Farkas, J. B. F., J. V. Ortiz, J. Cioslowski, ; and D. J. Fox, G., Inc., Wallingford CT, 2013.

21. Gieseking, R. L.; Mukhopadhyay, S.; Shiring, S. B.; Risko, C.; Bredas, J. L. Impact of bulk aggregation on the electronic structure of streptocyanines: implications for the solid-state nonlinear optical properties and all-optical switching applications. *J. Phys. Chem. C* **2014,** *118*, 23575-23585.

22. Hess, B.; BKutzner, C.; van der Spoel, D.; Lindahl, E. GROMACS 4: Algorithms for highly efficient, load-balanced, and scalable molecular simulation. *J. Chem. Theory Comput.* **2008,** *4*, 435–447.

23. Jorgensen, W. L.; Maxwell, D. S.; Tirado-Rives, J. Development and testing of the opls all-atom force field on conformational energetics and properties of organic liquids. *J. Am. Chem. Soc.* **1996,** *118*, 11225–11236.

24. Das, S.; Bwambok, D.; El-Zahab, B.; Monk, J.; de Rooy, S. L.; Challa, S.; Li, M.; Hung, F. R.; Baker, G. A.; Warner, I. M. Nontemplated approach to tuning the spectral properties of cyanine-based fluorescent NanoGUMBOS. *Langmuir* **2010,** *26*, 12867–12876.

25. Davydenko, I.; Marder, S. R. Unpublished work.

26. Hales, J. M.; Barlow, S.; Kim, H.; Mukhopadhyay, S.; Bredas, J.-L.; Perry, J. W.; Marder, S. R., Design of organic chromophores for all-optical signal processing applications. *Chem. Mater.* **2014,** *26*, 549-560.

CHAPTER 4

NON-COVALENT INTERACTIONS IN COUNTERION-CYANINE COMPLEXES

4.1. Introduction

As discussed in the Introduction, interactions between a cyanine and its counterion can lead to the loss of the promising cyanine NLO properties. This typically occurs *via* ion-pairing, in which the counterion localizes towards one end of the cyanine backbone and induces symmetry-breaking, a process enhanced especially with small, hard counterions such as chloride.[1] A cyanine in a symmetry-broken structure exhibits increased charge localization on the backbone near the end with the counterion and a concurrent increase in BLA.[1-3] As a consequence, the absorption peaks of the cyanines become blue-shifted and/or significantly broadened.[4-5]

A quantum-mechanical study involving a model streptocyanine with dimethylamino end groups and a chloride counterion revealed that when the counterion localizes towards one end of the cyanine the degree of BLA is increased.[6] This is consistent with an abundance of crystallographic data which show cyanines with large values of BLA[7-8] and the presence of the counterion near one end of the cyanine backbone.[9] When the counterion is in this position, Re(γ) becomes positive and Im(γ) increases. This leads to properties that are unsuitable for AOS applications.

Molecular dynamics simulations show that in thin films the counterion can be located at various positions broadly along the cyanine backbone.[10-12] Thus, to improve our fundamental understanding of symmetry-breaking due to cyanine-counterion interactions, a more detailed understanding of the counterion-cyanine interactions and energetics is needed. Here, we consider cyanine-counterion complexes with the counterion displaced from the molecular center of the cyanine backbone out to one molecular end. We pair a streptocyanine of increasing backbone lengths of 5 carbon (5C), 7 carbon (7C), 9 carbon (9C), and 11 carbon (11C) atoms with two counterions: a small, chemically hard chloride (Cl^-) and a larger, chemically soft tetrafluoroborate (BF_4^-), to construct potential energy surfaces of the cyanine-counterion complexes (Figure 4.1). Streptocyanines, cyanines with amino end groups, have been used in a variety of NLO studies as prototypical cyanine molecules.[6, 13-15] By applying the symmetry-adapted perturbation technique (SAPT), we can study the evolution of the interaction energy and non-covalent interactions as a function of counterion displacement and compare the preferred counterion displacements among backbone lengths and counterions. Understanding the nature of cyanine-counterion interactions can aid in developing strategies to control or minimize them.

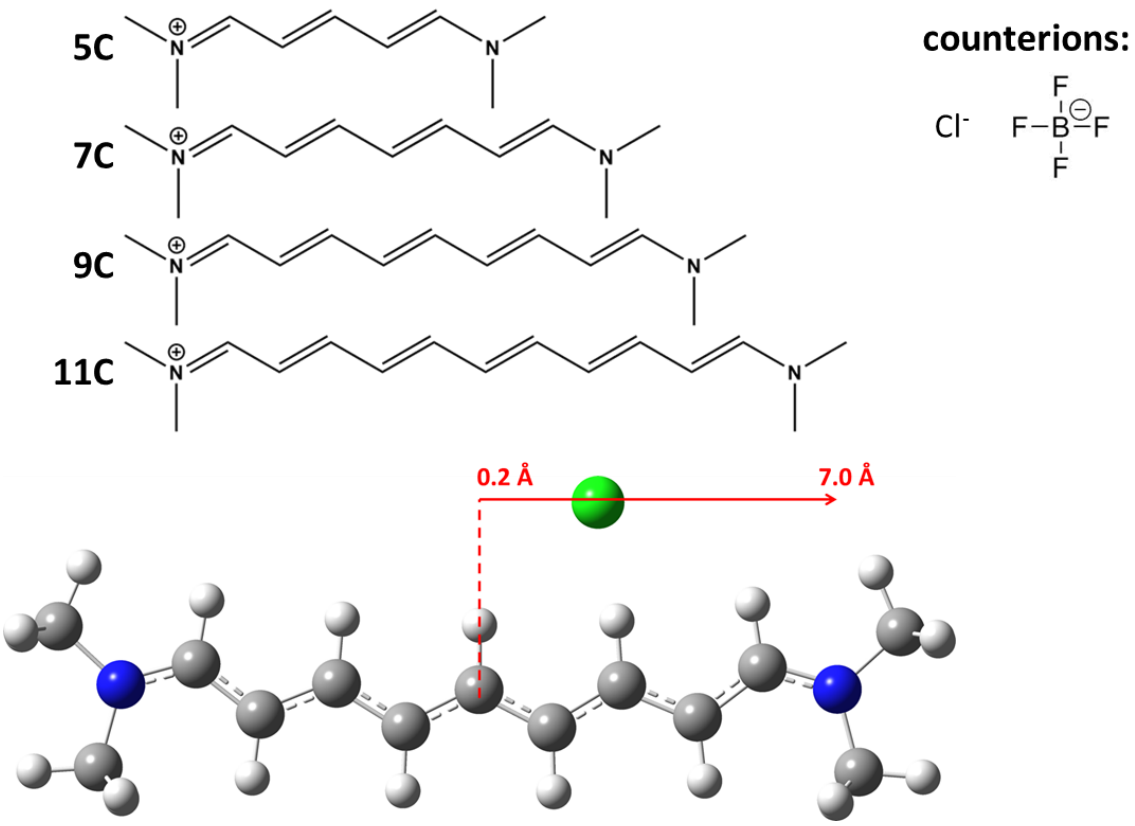

Figure 4.1: Chemical structures of streptocyanines and counterions (top, left and right, respectively), and illustration of counterion displacement along the 11C backbone (Cl^- shown for example).

4.2. Computational Methodology

Three series of ground-state geometry optimizations were performed: (1) unconstrained optimizations for each isolated streptocyanine with and without an applied electric field; (2) unconstrained optimizations for each streptocyanine with each counterion (Cl^- and BF_4^-); and (3) constrained optimizations for each streptocyanine with the Cl^- counterion (and for 5C with BF_4^-) displaced along the backbone.

The unconstrained ground-state geometry optimizations of the isolated streptocyanines were performed at the DFT level using the ωB97X-D functional[16] with the default range-separation parameter (ω = 0.2 $Bohr^{-1}$) and the cc-pVDZ basis set[17], which has been shown previously to give reasonable BLA values for streptocyanines.[6] The unconstrained ground-state geometry optimizations of the streptocyanine/counterion complexes were performed with the ωB97X functional[18] with its default range-separation parameter (ω = 0.3 $Bohr^{-1}$) and cc-pVDZ basis set for consistency with the constrained geometry optimizations (see below for reason why dispersion-corrected functionals could not be used). The absence of imaginary frequencies was used to confirm that the optimized geometries correspond to minima on the potential energy surfaces. Geometry optimizations with an electric field applied along the long molecular axis were conducted at the same level of theory; the applied field strengths ranged from 0.0 to +8.0 $x10^7$ V/cm, which correspond to the usual field strengths considered in similar calculations.[19]

The optimized geometries of the isolated streptocyanines were used as an initial starting point for constrained geometry optimizations of the streptocyanine/chloride counterion complexes (see following paragraph for a discussion on the imposed constraints). The constrained geometry optimizations of the streptocyanines-chloride complexes were performed using the ωB97X functional with its default range-separation parameter (ω = 0.3 $Bohr^{-1}$) with the cc-pVDZ basis set[17]. We note that the dispersion-corrected functional could not be used for the constrained geometry optimizations due to the presence of ghost atoms (which contain no charge or electrons), as the ghost atoms required to properly constrain the counterion position are not implemented in the Gaussian software with dispersion-corrected functionals. To avoid basis set superposition errors, the geometry

optimizations of the streptocyanine-counterion complexes were performed using the counterpoise correction.[20]

In the streptocyanine-chloride complex optimizations, the geometry of the streptocyanine backbone was constrained to maintain the backbone angles between the hydrogen atom of the central carbon atom and the terminal nitrogen atom to those values of the optimized isolated streptocyanine backbone (Figure 4.2, top). We define an internal coordinate system such that the *x*-axis is parallel to the molecular long axis between the terminal nitrogen atoms; the *y*-axis is perpendicular to the *x*-axis within the molecular plane, and the *z*-axis is out of the molecular XY plane. The counterion was constrained to the XY plane of the streptocyanine backbone in order to be kept parallel to the backbone (Figure 4.2, bottom). The counterion was then displaced along the x axis from the center of the streptocyanine backbone towards one molecular end at increments of 0.2 Å. The constrained geometry optimizations were performed for each displacement. All geometry optimizations were performed in Gaussian 09.[21] The average bond-length alternation (BLA) was calculated as the difference between the average bond lengths of the nominally single and double bonds.

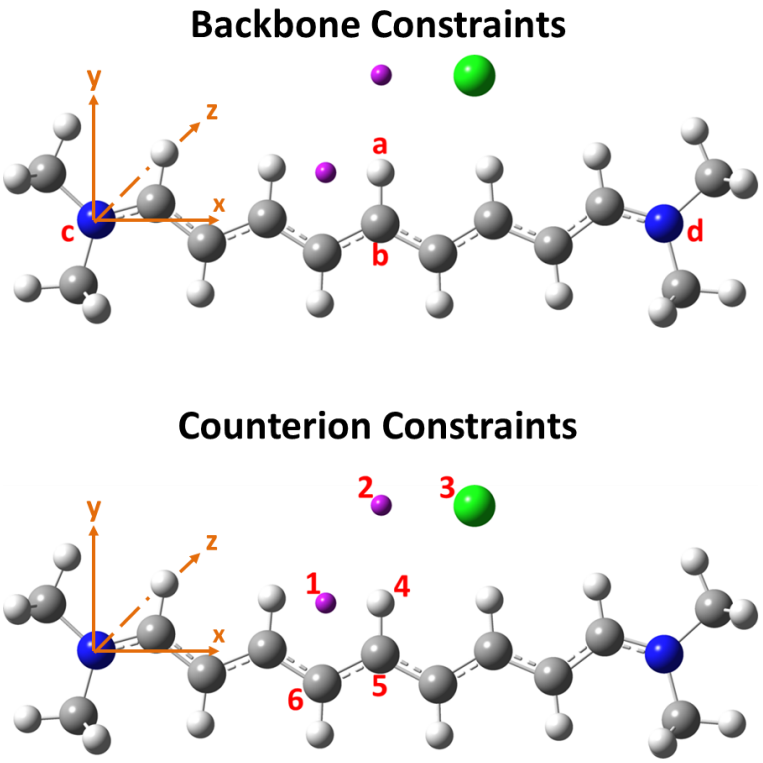

Constraint		
angle	a-b-c	fixed
angle	a-b-d	fixed

Constraint		
angle	1-4-2	90°
angle	1-4-5	90°
angle	4-2-3	90°
bond	1-4	
bond	2-3	
dihedral	1-4-2-3	180°
dihedral	1-4-5-6	180°

Figure 4.2: Illustration and corresponding constraints imposed upon the streptocyanine backbone (top) and counterion (bottom) (shown here as Cl^-). The purple dots are the ghost atoms. An internal coordinate system is defined such that the *x*-axis points aligns between terminal nitrogen atoms, the *y*-axis is perpendicular to the *x*-axis such that the XY plane contains the streptocyanine, and the *z*-axis is perpendicular to the XY plane.

To understand the effect of counterion positioning on the magnitude and sign of Re(γ), Re(γ) was calculated using the INDO Hamiltonian along with a multi-reference determinant configuration interaction (MRDCI) scheme. The reference determinants selected for the MRDCI scheme included the ground-state reference determinant, the single-electron excitations corresponding to HOMO-1→LUMO and HOMO→LUMO+1, and the double-electron excitation HOMO→LUMO for orbitals centered on the streptocyanine backbone. All possible single-electron excitations within the first 30

occupied and 30 unoccupied orbitals were included. Re(γ) were computed using a sum-over-states perturbation approach, summing over 950 excited states. These calculations for each counterion displacement were performed within ZINDO.

The binding energy as a function counterion displacement was evaluated by using density-fitted 2nd-order Møller–Plesset perturbation theory with the jun-cc-pVDZ basis set.[22] The binding energy (E_{bind}) is calculated as:

$$E_{bind} = E_{int} + E_{def} \tag{4.1}$$

where E_{int} is the interaction energy and E_{def} is the deformation energy. The interaction energy is the energy needed to separate the streptocyanine/counterion complex into two infinitely separated monomers, each with the geometry that was found in the complex; the deformation energy is the energy needed to relax these separated monomers to their separate equilibrium geometries. Symmetry adapted perturbation theory (SAPT(0)/ jun-cc-pVDZ) was used to decompose the non-covalent interaction energy as a function of counterion displacement into electrostatic, induction, dispersion, and exchange terms. Both SAPT and DF-MP2 calculations were performed using PSI4.[23] The geometries for these calculations were taken from the constrained geometry optimizations of the streptocyanine/chloride complexes.

4.3. Results

We begin our discussion with the fully optimized streptocyanine/counterion complexes, then consider the evolution of the streptocyanine BLAs as a function of counterion displacement, and follow up with a discussion on the binding energies as function of

streptocyanine backbone length. We conclude by discussing the non-covalent interactions between the streptocyanine and counterion.

4.3.1. Impact on Streptocyanine Molecular Geometry

The distances, vector components, and BLA for the Cl^- and BF_4^- counterions from the closest terminal nitrogen atom and central carbon atom along the backbone at their fully optimized distances for each streptocyanine backbone length are presented in Table 4.1. We note that a previous investigation in our research group stated that the counterion increasingly localizes towards one molecular end of the backbone as a function of increasing backbone length in unconstrained geometry optimizations of streptocyanine/Cl^- complexes.[6] Here, we stress a slightly different view: That the counterion localizes at a consistent distance from the terminal end of the backbone, near the nitrogen atom, regardless of the number of carbon atoms in the backbone or size of the counterion.

Table 4.1: Distance (Å) and vector components (Å) of counterion from a center of origin at the nearest terminal nitrogen atom (top) and a center of origin at the central carbon atom on the backbone (bottom), as measured in the unconstrained geometry optimizations of streptocyanine with Cl^- or BF_4^- counterions, as calculated at the ωB97X/cc-pVDZ level. BLA (Å) included for each counterion and backbone length.

	5C		**7C**		**9C**		**11C**	
	Cl^-	**BF_4^-**	**Cl^-**	**BF_4^-**	**Cl^-**	**BF_4^-**	**Cl^-**	**BF_4^-**
Center of Origin: Nearest Terminal Nitrogen Atom								
x (Å)	2.63	3.61	2.09	2.42	2.01	1.71	2.06	1.71
y (Å)	3.33	3.49	3.41	3.56	3.38	3.59	3.33	3.55
z (Å)	0.00	0.0949	0.00	0.125	0.00	0.136	0.00	0.227
distance (Å)	4.24	5.02	4.00	4.31	3.93	3.98	3.92	3.94
Center of Origin: Center Backbone Carbon Atom								
x (Å)	0.969	0.00	2.80	2.48	4.00	4.26	5.28	5.64
y (Å)	3.18	3.28	3.81	3.88	3.18	3.03	3.88	3.65
z (Å)	0.00	0.497	0.00	0.235	0.00	0.359	0.00	0.211
distance (Å)	3.33	3.64	4.73	4.92	5.11	6.00	6.56	7.35
BLA (Å)	0.0194	0.00	0.0483	0.0327	0.0625	0.0523	0.0716	0.0611

Each counterion stays roughly in the same location for each series of backbone lengths, and the distances from the terminal N atom are similar for both counterions, especially for the longer backbones (9C and 11C). Due to the increased size of the BF_4^- counterion compared to Cl^-, BF_4^- sits further away from the nitrogen in the *y*-direction (along the cyanine short axis) but closer to the nitrogen in the *x*-direction (along the cyanine long axis). Unlike the Cl^- counterion, BF_4^- does not remain perfectly in the plane of the backbone

along the *z*-axis, but becomes angled to expose more of the boron atom to the streptocyanine backbone.

As the chain length is increased, the counterion is increasingly further removed from the molecular center. For the shortest streptocyanine (5C), the BF_4^- counterion optimized geometry is at the molecular center and the Cl^- counterion is near the molecular center. Even though the counterion localizes consistently near one terminal end of the backbone, the distance relative to the center carbon atom increases as a function of increasing chain length. Overall, the degree of BLA is smaller for the larger, less-polarizing BF_4^- counterion than for the smaller, more polarizing Cl^- counterion. We will refer back to these optimized values as the preferred geometries in the subsequent discussion and sections, and consider the unconstrained optimization geometries again in the context of SAPT(0) later.

The evolution of the degree of BLA for the streptocyanine backbones as a function of Cl^- counterion position is presented in Figure 4.3. For each streptocyanine backbone length, the degree of BLA smoothly evolves from cyanine-like (BLA ~ 0.0 Å) to nearly polyene-like (BLA ~ 0.1 Å) as the counterion is displaced from the molecular center of the backbone to one molecular end. The degree of BLA reaches its maximum for each streptocyanine backbone length when the Cl^- counterion is at the molecular end near the terminal nitrogen atom, and subsequently most of the positive charge carried by the streptocyanine becomes localized there. Comparing the maximum BLA for each backbone length, we see that the longer the backbone length, the larger the maximum BLA; thus, the 11C streptocyanine backbone possesses the largest degree of BLA (0.0793 Å) among the backbone lengths investigated, given its longer backbone affording larger displacements. While the 11C possesses the largest BLA at the maximum counterion displacement, the degree of BLA

does not quite reach the polyene-limit. For displacements beyond the terminal nitrogen atom, the degree of BLA becomes reduced.

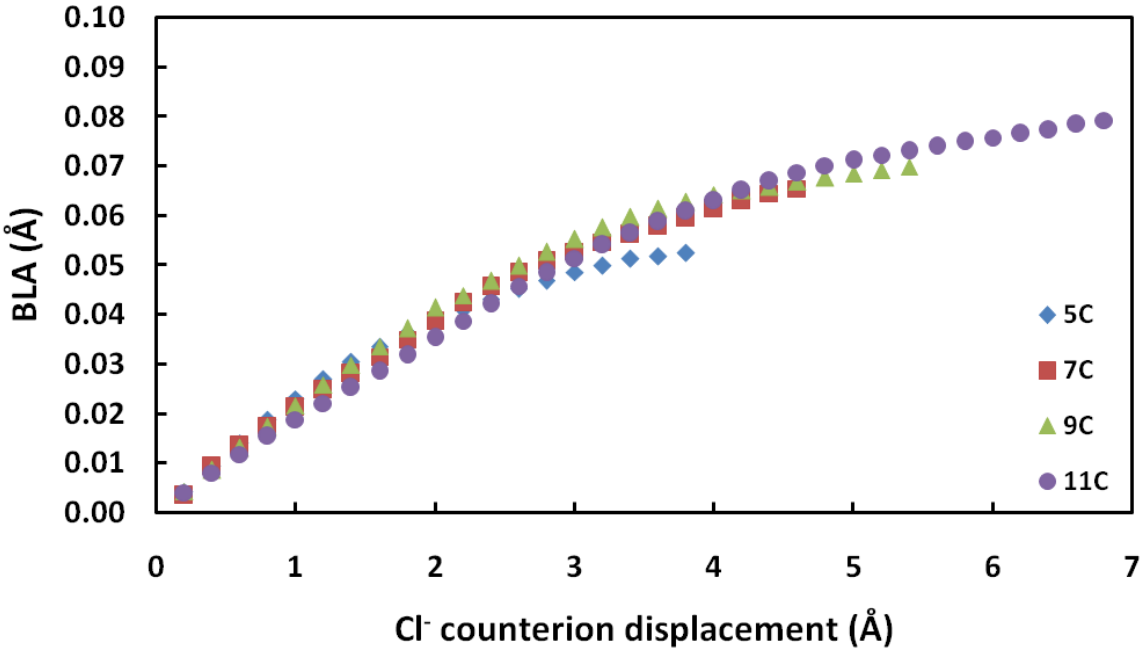

Figure 4.3: Evolution of BLA (Å) as a function of Cl^- counterion displacement (Å) for streptocyanine backbones containing 5C (blue diamonds), 7C (red squares), 9C (green triangles), and 11C (purple circles) atoms, as calculated at the ωB97X/cc-pVDZ level.

Importantly, the degree of BLA is similar for each backbone length at the same Cl^- displacement. As stated above, longer streptocyanines are significantly more polarizable than shorter ones, and the similarity between degrees of BLA for each counterion displacement is markedly different from the degrees of BLA obtained when a uniform electric field is applied along the long axis (Figure 4.4). At each strength of the applied electric field, the longer backbones have a larger degree of BLA compared to the smaller backbones, such that at a field strength of 4×10^7 V/cm the BLA of the 11C backbone is

double that of the 5C backbone. The degree of BLA for the 11C has nearly reached the polyene-limit under application of a uniform field.

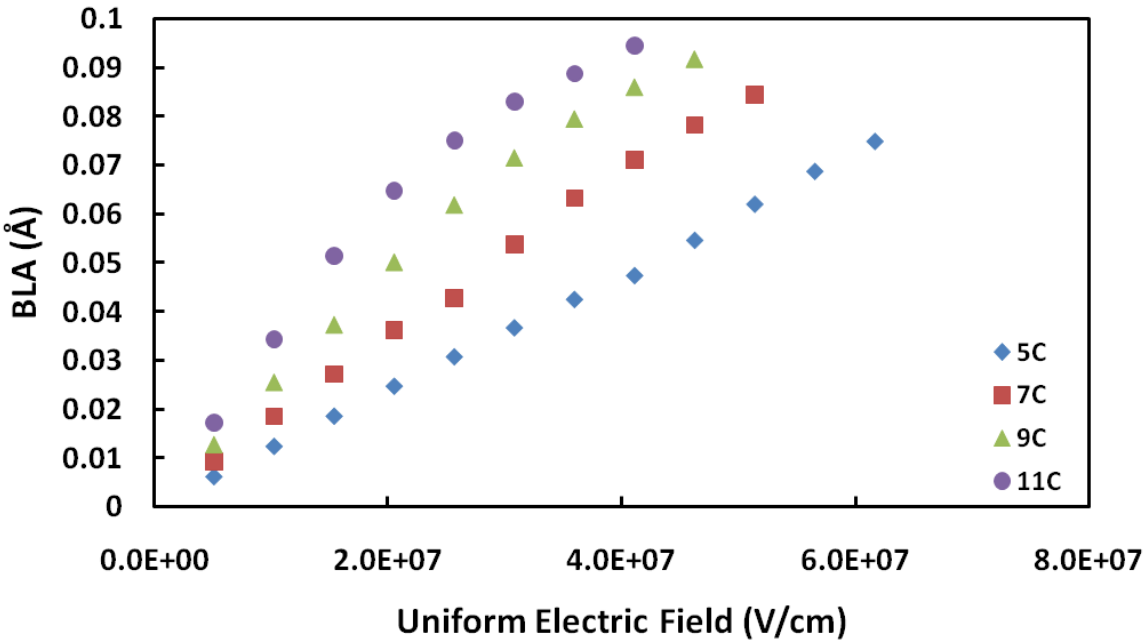

Figure 4.4: Evolution of BLA (Å) as a function of applied uniform electric field (0.0 to 8.00 x10^7 V/cm), as calculated at the ωB97X/cc-pVDZ level.

We can understand the difference in behavior in the relative degrees of BLA between the environments by comparing the electric fields generated by the counterion and an applied electric field (Figure 4.5). The electric field generated by the counterion is radial, so the direction and intensity vary along the backbone. The counterion electric field is localized near the counterion position at its displacement along the backbone, a situation different from an electric field applied uniformly along the streptocyanine backbone. Since the counterion electric field is non-uniform, we approximate the magnitude of the electric field

along the streptocyanine backbone as the difference between the counterion electric field magnitudes at the two terminal nitrogen atoms.

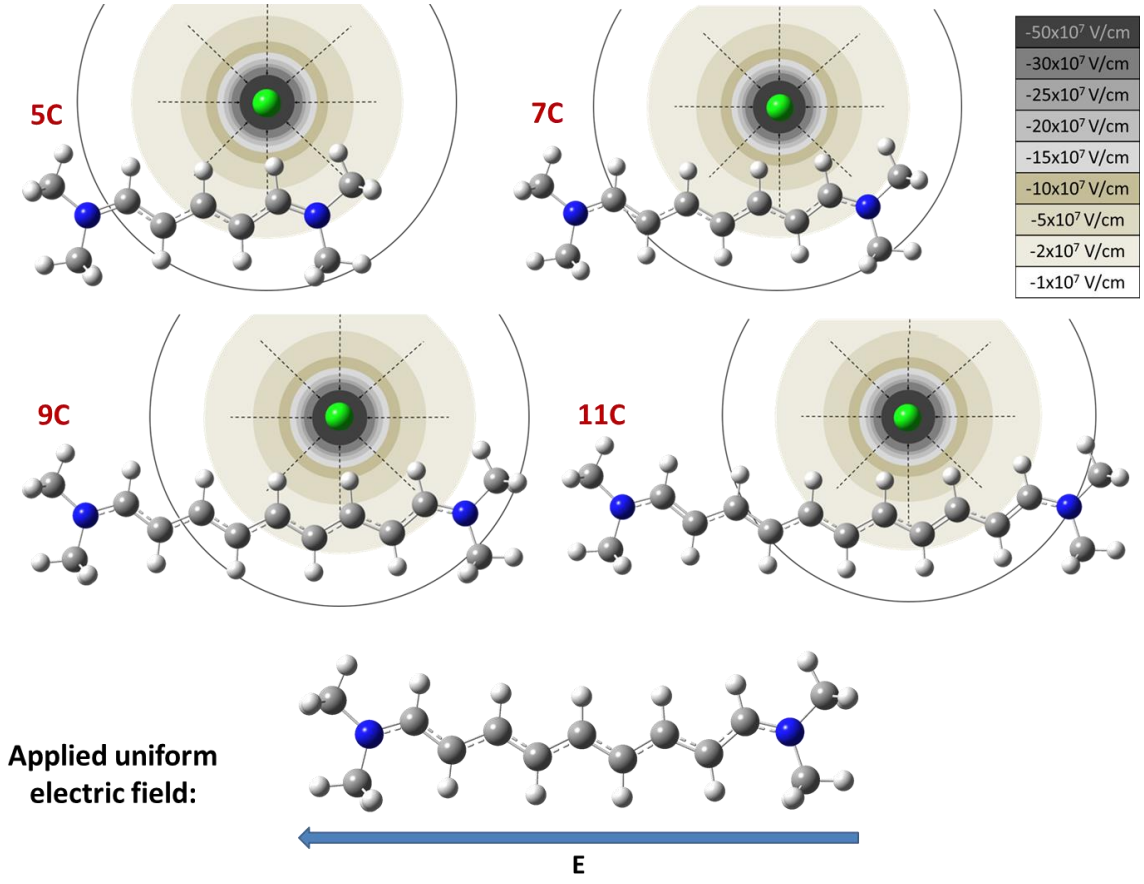

Figure 4.5: Comparison of electric fields generated by a counterion at a displacement of 2 Å as a function of chain length (top) and an applied uniform field (bottom). The counterion electric field is highly non-uniform, leading to different field strength magnitudes across the length of the backbone.

The electric field generated by the small, hard, Cl^- counterion is very localized along the streptocyanine backbone, such that the shorter backbones feel a stronger effective electric field compared to the longer backbones (Figure 4.6). The shorter streptocyanine backbones have a larger difference in the electric field between molecular ends at the same

displacement compared to the longer backbones. Although the displacements from the molecular center are the same, in the shorter backbones the counterion is closer to a molecular end. This molecular end experiences a stronger electric field compared to the opposite end, and an asymmetric environment is established along the backbone. When the counterion is close to the molecular center of the streptocyanine backbone, the streptocyanine experiences a symmetric electric environment, with the electric field magnitudes being similar at the molecular ends. As the counterion is displaced from the center towards one molecular end, the streptocyanine experiences an increasingly asymmetric environment, the asymmetry of which increases with increasing backbone length.

Ultimately, the calculated degree of BLA depends on both the intrinsic polarizability of the backbone and the effective counterion electric field. The localized counterion electric field induces localized geometry distortions along the streptocyanine backbone. The interactions among these three effects effectively compensate one another to produce similar degrees of BLA among the streptocyanine backbones at the same counterion displacements. As the degree of BLA is an indicator of ground-state polarization, the various degrees of BLA as a function of counterion displacement further suggest that cyanines in thin films with counterions at various displacements along the backbone (see Chapter 3) can have various degrees of polarization, and the cyanines most likely exist in a mixture of symmetric and symmetry-broken structures, depending on the strength of the cyanine-counterion interactions.

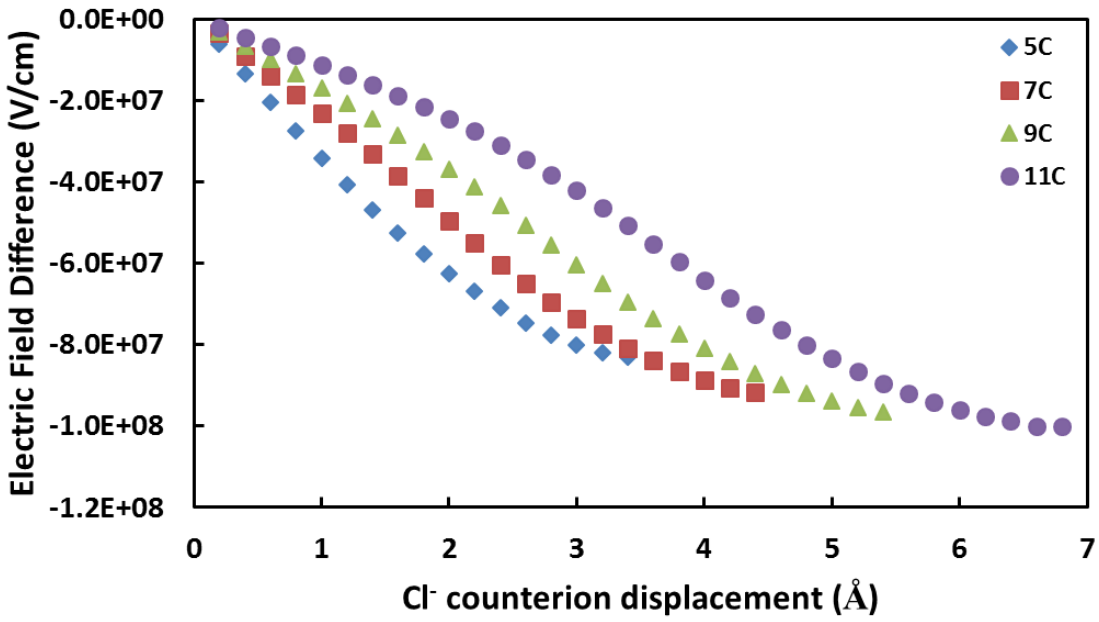

Figure 4.6: Difference in electric field magnitude (V/cm) between molecular ends of each streptocyanine backbone length as a function of increasing Cl^- counterion displacements from molecular center, as calculated at the ωB97X/cc-pVDZ level.

The effective counterion electric field as felt along the streptocyanine backbone is diminished for larger counterions, such as BF_4^-, that are large and chemically soft, with charge distributed throughout the molecule. The small, hard, Cl^- counterion with its concentrated charge, is therefore able to exert a stronger effective electric field. The degree of BLA for the 5C streptocyanine as a function of BF_4^- displacement is reduced at each displacement compared to the Cl^- counterion (Figure 4.7). Although the maximum degree of BLA obtained is reduced when moving from the Cl^- counterion (BLA = 0.0524 Å) to the BF_4- counterion (BLA = 0.463 Å), the BLA is still significant compared to the isolated streptocyanine and when the counterion is near the molecular center of the backbone. The counterion, regardless of identity, has the largest contribution to symmetry breaking when it is localized near one end of the backbone.

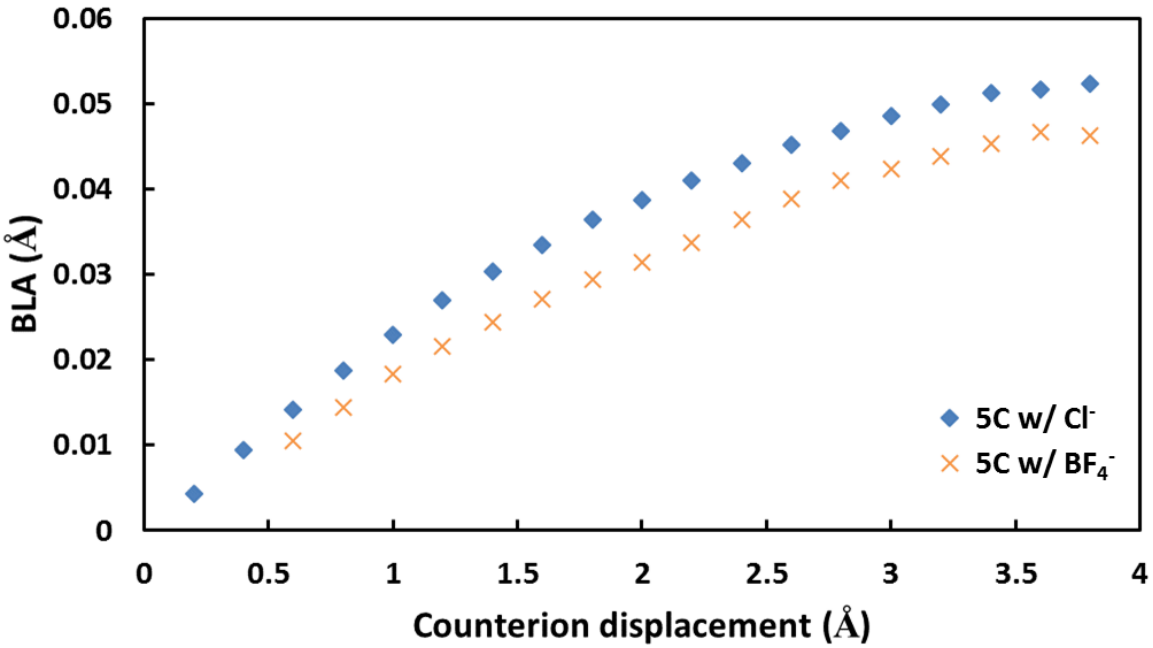

Figure 4.7: Degree of BLA (Å) as a function counterion displacement (Å) for the 5C streptocyanine with Cl^- and BF_4^- counterions, as calculated at the ωB97X/cc-pVDZ level.

As Re(γ) depends on the degree of BLA, we briefly consider Re(γ) as a function of counterion displacement for the 5C, 9C, and 11C streptocyanines (Figure 4.8). As to be expected, at displacements with small degrees of BLA, Re(γ) is negative and large (on the order of 10^{-33} esu), while at displacements corresponding to larger BLA, Re(γ) becomes positive (and large in the case of 11C streptocyanine). At displacements corresponding to and greater than the optimized counterion displacement from the molecular center, Re(γ) becomes saturated, which is consistent with the streptocyanine being in a fully symmetry-broken structure.[24] The crossover point from negative to positive Re(γ) occurs at displacement smaller than the optimized counterion location, and the crossover point decreases with increasing backbone length. The message here is that backbone-counterion interactions must be controlled to preserve the prototypical streptocyanine structure, as

once the counterion is displaced from near the molecular center (displacements > 1 Å), large reductions in the magnitude of Re(γ) occur, consistent with previously observations that small increases in BLA can significantly reduce the magnitude of Re(γ).[25-26]

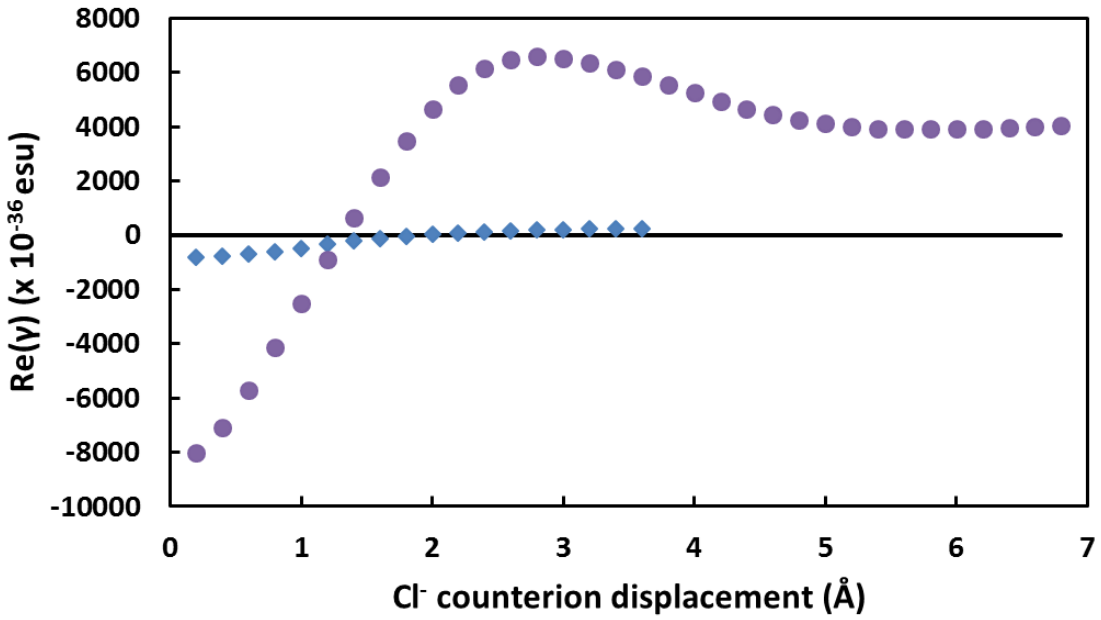

Figure 4.8: Evolution of Re(γ) as a function of counterion displacement for 5C and 11C streptocyanines.

As discussed in the previous Chapter, the most probable location for finding the counterion when paired with experimentally-synthesized cyanines is significantly further away from the molecular end of the backbone, especially for larger counterions. We recall that this is due to the increased steric bulk both along the backbone and on the counterion preventing the counterion from approaching closely. As the strength of the electric field generated by the counterion scales as $\frac{1}{r^2}$, we expect that the values presented here for the model streptocyanine/Cl^- complexes are the upper limit to those that can be obtained in thin films.

However, in thin films the degree of BLA and therefore extent of symmetry breaking depends on the total electrostatic interactions between all counterions and cyanines, and more work is needed to understand how multiple counterions near the backbone can influence the degree of BLA.

4.3.2. Binding Energy

To investigate the similarity in the preferred counterion positions among the streptocyanines, we next consider the binding, interaction, and deformation energies as a function of Cl^- counterion displacement. The binding energy for the streptocyanine backbones with the Cl^- counterion is shown in Figure 4.9.

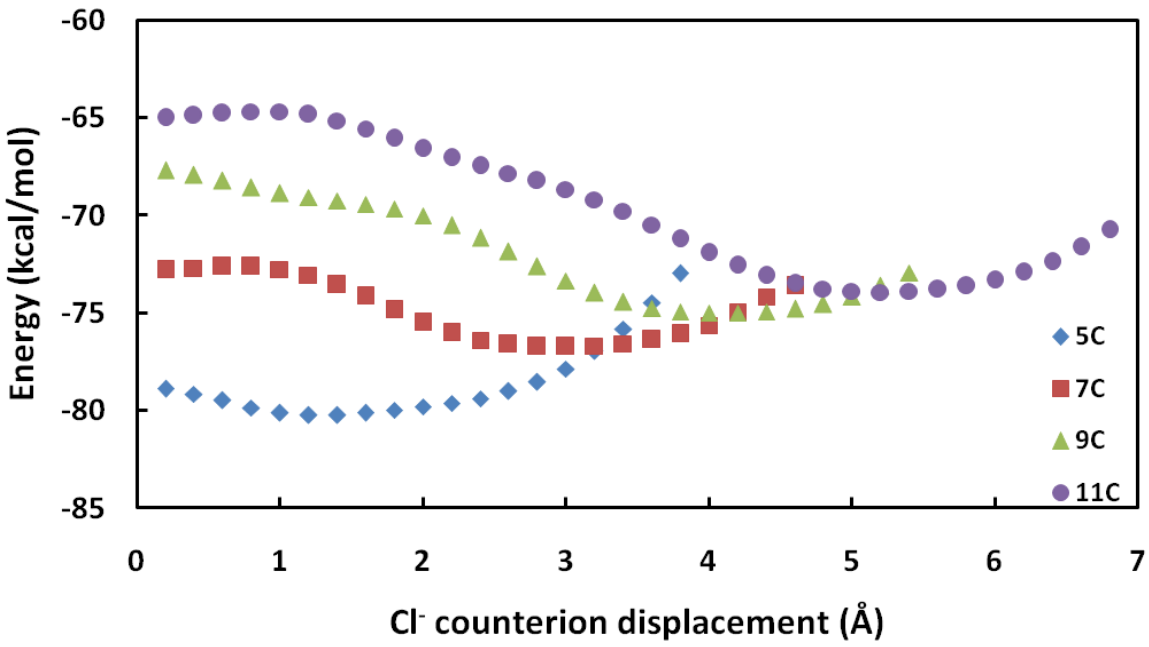

Figure 4.9: Binding energy for streptocyanine backbones as a function of Cl- counterion displacement, computed at the DF-MP2/jun-cc-pVDZ level from ωB97X/cc-pVDZ constrained optimized geometries.

The binding energy is most negative, and thus the streptocyanine-counterion complex is most stable, when the Cl^- counterion is near one molecular end of the streptocyanine backbone. The most stable configuration is at the Cl^- displacement which corresponds to the preferred location of the counterion in the unconstrained optimized geometry. At displacements near the molecular center of the backbone or at the terminal N atom or beyond, the binding energy decreases, indicating a weaker-bound complex. The binding energy decreases with increasing backbone length, indicating that the complexes of longer backbone lengths are less strongly bound than the complexes of shorter backbone lengths. We can understand this trend by considering the differences between the interaction energy (Figure 4.10) and deformation energy (Figure 4.11), as these two terms sum into the binding energy.

In general, at each displacement, the interaction energy is weaker for the longer backbone lengths. For backbones longer than 5C, the greatest interaction energy between the streptocyanine and counterion (which again occurs at the counterion displacement equal to the location of the counterion in the fully optimized complex) is similar (~-80 kcal/mol); the interaction energy for the 5C streptocyanine is greater at -83.5 kcal/mol. We recall that the shorter backbone length of the 5C backbone results in the preferred geometric position of the Cl^- counterion being closer to the molecular center of the streptocyanine backbone, resulting in a more equal charge distribution along the backbone and a smaller degree of BLA.

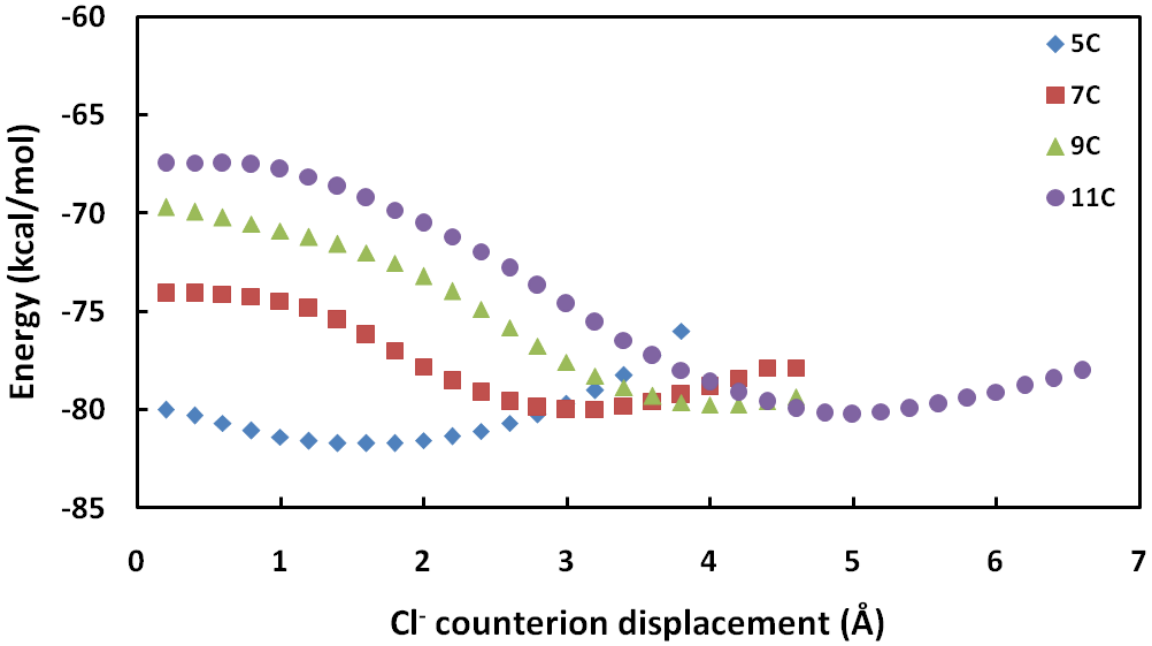

Figure 4.10: Interaction energy (kcal/mol) for various streptocyanine backbone lengths as a function of Cl^- counterion displacement (Å), as computed at the DF-MP2/jun-cc-pVDZ level from ωB97X/cc-pVDZ constrained optimized geometries.

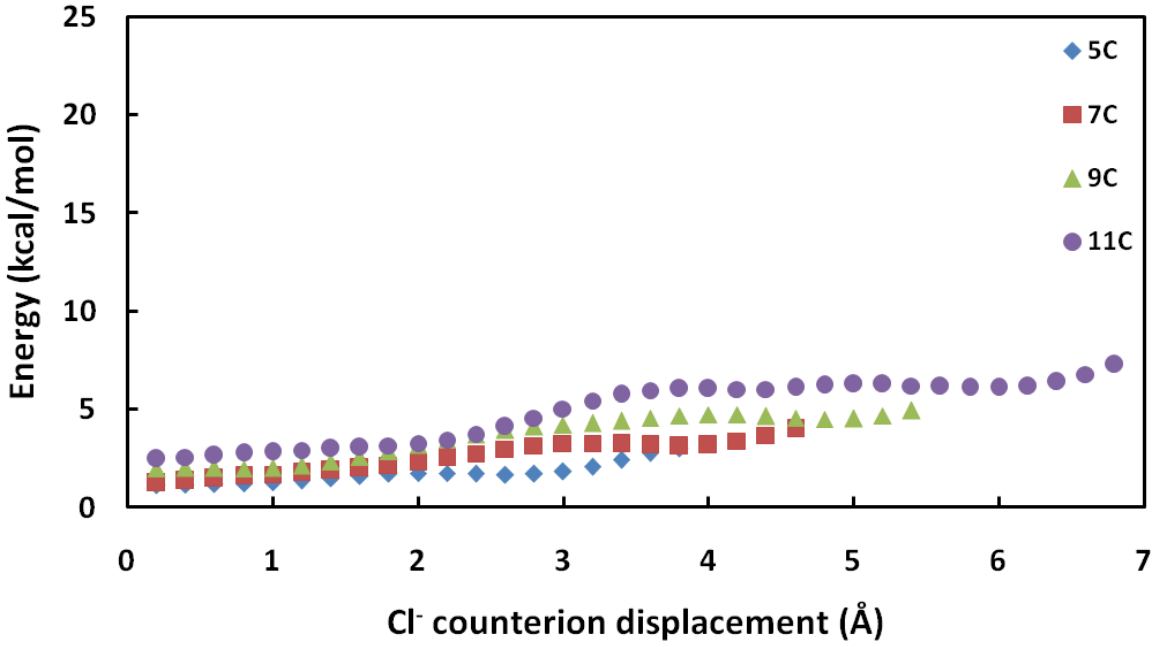

Figure 4.11: Deformation energy (kcal/mol) for various streptocyanine backbone lengths as a function of Cl^- counterion displacement (Å), as computed at the DF-MP2/jun-cc-pVDZ level from ωB97X/cc-pVDZ constrained optimized geometries.

Critically, the potential energy surface as a function of counterion displacement is flat enough near the preferred counterion displacement for each backbone length that thermal energy at room temperature is enough to allow counterion to move within a fairly large range of displacements. This potential for displacement is asymmetric from the preferred displacement: the Cl^- counterion can move up to 0.8 Å closer to the terminal nitrogen at the molecular end, while it can only move up to 0.4 Å back towards the molecular center. A similar situation is seen in the case of the BF_4^- counterion, where thermal energy affords displacements that allow it to become closer to the terminal N atom by up to 1 Å. As displacing the counterion towards the molecular end leads to an increased degree of BLA, this implies that at room temperature the streptocyanines may have a larger degree of BLA than suggested from their fully optimized geometries, particularly with regards to the 5C streptocyanine.

The largest changes between each streptocyanine backbone length occur for the deformation energy. When the counterion is near the molecular center of the streptocyanine backbone, the energetic cost for the localized geometry distortions is small (< 2.5 kcal/mol), as both molecular ends essentially "see" the same environment. This cost grows as a function of increasing displacement and backbone length, as the longer backbones experience an increasingly asymmetric environment compared to the shorter backbones. At similar displacements, the 11C streptocyanine incurs a larger energetic penalty for the localized geometry distortions along its backbone. The weaker binding energy of the longer backbones is therefore related to increased deformation energy of the longer backbones.

4.3.3. Non-Covalent Interactions

To understand the Cl^- counterion preferred location relatively close to the terminal nitrogen atom, we have decomposed the non-covalent interaction energy via SAPT(0) into the usual four terms corresponding to electrostatic (the energy of the Coulombic interaction between the streptocyanine and counterion), exchange (a quantum-mechanical effect), induction (the polarization of the streptocyanine by the counterion and *vice versa*), and dispersion (induced dipole-dipole interactions) energies. We first compare the limiting cases of the 5C and 11C streptocyanines as a function of Cl^- counterion displacement, then consider each of the fully optimized complex geometries for both the Cl^- and BF_4^- counterions. We note that the SAPT(0) total interaction energies for the 5C and 11C streptocyanines with Cl^- counterion displacements are expressed as differences relative to the first displacement of 0.2 Å; since the individual terms have large magnitudes at each displacement, we therefore focus on the changes in the terms upon increasing displacement from the molecular center.

We recall that the preferred Cl^- location from the terminal nitrogen atom is similar across all backbone lengths and that due to the reduced backbone length of the 5C streptocyanine the counterion sits closer to the molecular center than in the longer streptocyanines (7C, 9C, 11C). For the 5C streptocyanine (Figure 4.12), the total negative interaction energy reaches a minimum at the preferred Cl^- displacement before rapidly increasing at displacements beyond that. For the energetically preferred displacement, the electrostatic term dominates the total interaction energy, with some small cancellation from the exchange term which carries a sign opposite to that of the electrostatic term. When the counterion is at the molecular end, the magnitude of the electrostatic, induction, and

dispersion terms are reduced, while the exchange term is maximized and dominates the total interaction energy, leading to its positive difference compared to the first displacement. While it is a purely quantum-mechanic effect, the exchange term can be visualized as a manifestation of steric repulsion; when the counterion is at a displacement of ~3 Å, the counterion sits nearer to the backbone than in the center due to the curvature of the backbone. As the counterion also sits between two hydrogen atoms, this leads to the exchange term being maximized. The electrostatic interaction is responsible for the stabilization of the counterion at its preferred displacement, although for 5C the electrostatic stabilization responsible is not significantly different compared to the counterion at the molecular center. While in 5C most of the charge is near the end groups, the preferred displacement from the molecular center for 5C affords the counterion a slightly stronger electrostatic interaction with one terminal N, without losing too much of the interaction with the other molecular end.

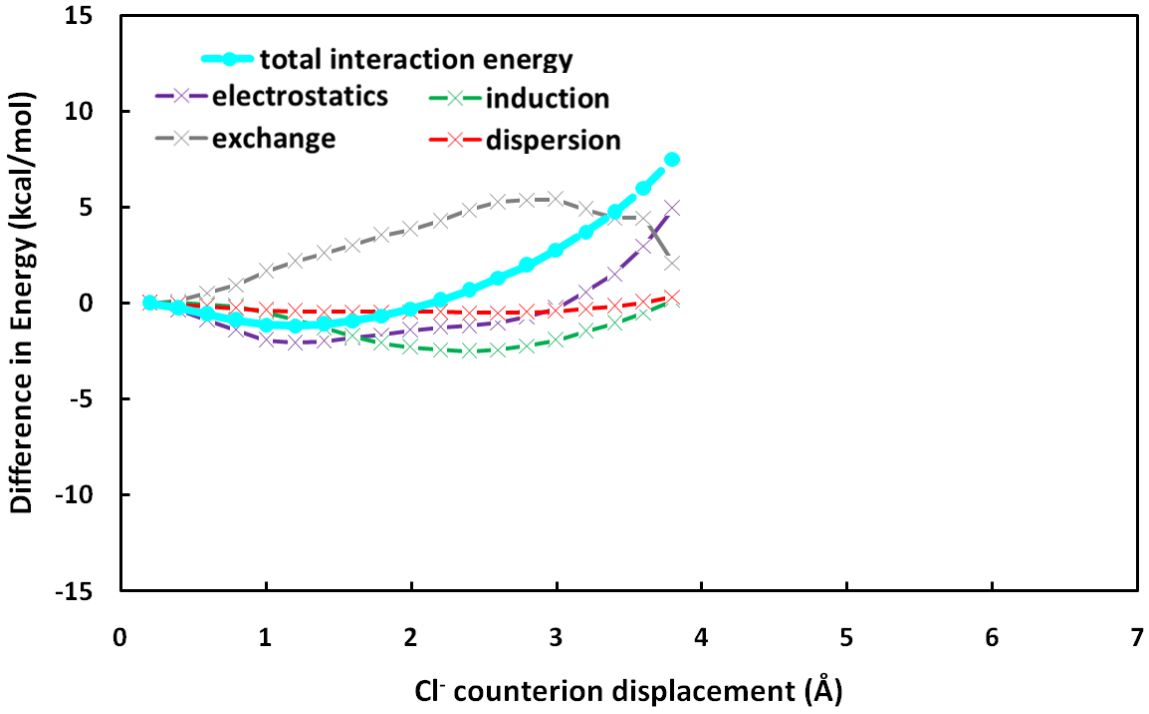

Figure 4.12: Differences in energy from the first displacement for SAPT(0)/jun-cc-pVDZ total energies and their components in the 5C streptocyanine/Cl^- complex, as a function of Cl^- counterion displacement.

As the length of the streptocyanine backbone grows, the differences in the electrostatic terms between the displaced and center counterion positions increase. For the 11C streptocyanine, this difference amounts to ~12.5 kcal/mol (Figure 4.13) at the preferred counterion displacement. Electrostatic and induction (polarization) are again responsible for the stabilization of the counterion at the preferred displacement, where the electrostatic term dominates the interaction energy; some cancellation from the exchange term occurs, while dispersion plays a relatively minor role. The dispersion term is maximized when the counterion is near the terminal N for the same reason as in the 5C case: the counterion sits between two hydrogen atoms nearer to the backbone than when it is near the center, due to the pronounced curvature in the 11C streptocyanine. When the counterion is displaced

closer to and beyond the terminal N atom, the stabilization from the electrostatic and induction terms diminish while the exchange term increases. We note that the electrostatic term is relatively flat near its energetic minimum, consistent with our earlier discussion concerning the accessible displacements at room temperature. As the counterion moves towards one end of the streptocyanine backbone, more of the streptocyanine backbone charge migrates towards that end of the molecule, increasing the electrostatic interaction between it and the backbone. At the preferred position, most of the backbone charge is localized near one molecular end, affording the greatest stabilization to the counterion charge.

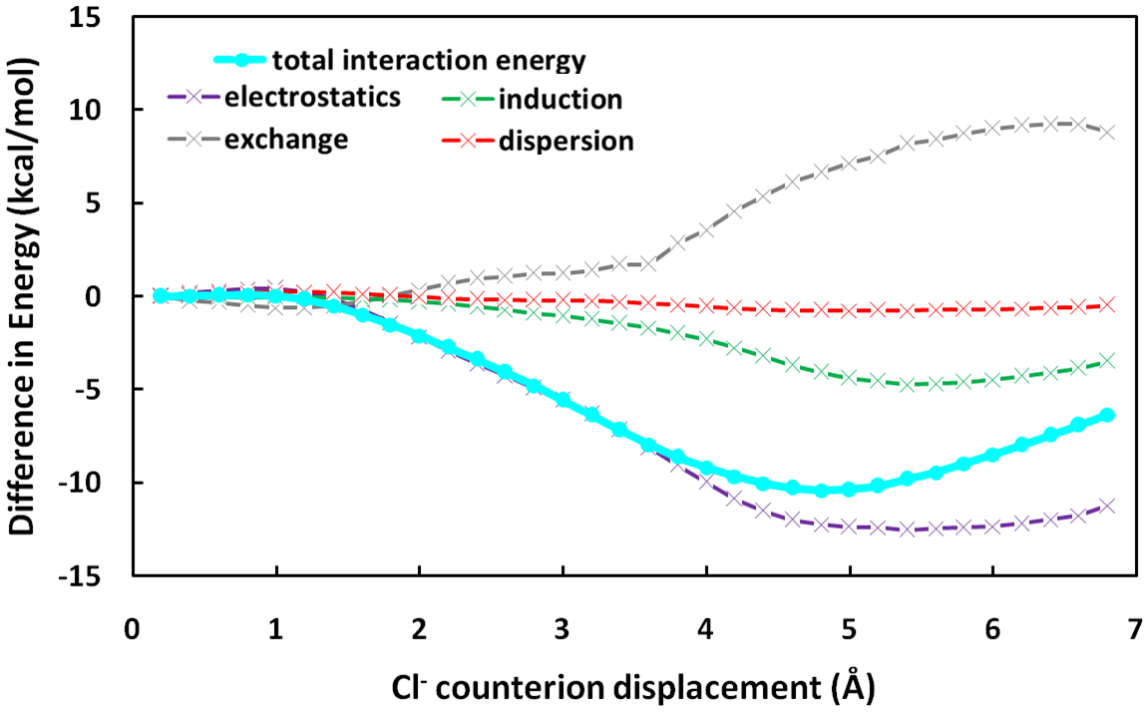

Figure 4.13: Differences in energy from the first displacement of SAPT(0)/jun-cc-pVDZ total energies and their components in the 11C streptocyanine/Cl^- complex, as a function of Cl^- counterion displacement.

The absolute values for SAPT(0) energies and their components (*i.e.*, not the relative differences among each backbone length) for the fully optimized streptocyanine/Cl^- and streptocyanine/BF_4^- complexes is presented in Figure 4.14 and as a function of backbone length. The total energy and energies of the individual terms are similar regardless of the number of carbon atoms within the backbone. At each backbone length, the electrostatic term dominates, with contributions from the induction (polarization) term, and a reduction in magnitude from the exchange term. Dispersion plays a minor role. The energetics between the Cl^- and BF_4^- counterions are broadly similar, although the terms are slightly smaller in the case of BF_4^-. As the stabilization of the counterion and total interaction energies are independent of the backbone length, these results illustrate that the interaction between the streptocyanine and counterion is highly localized.

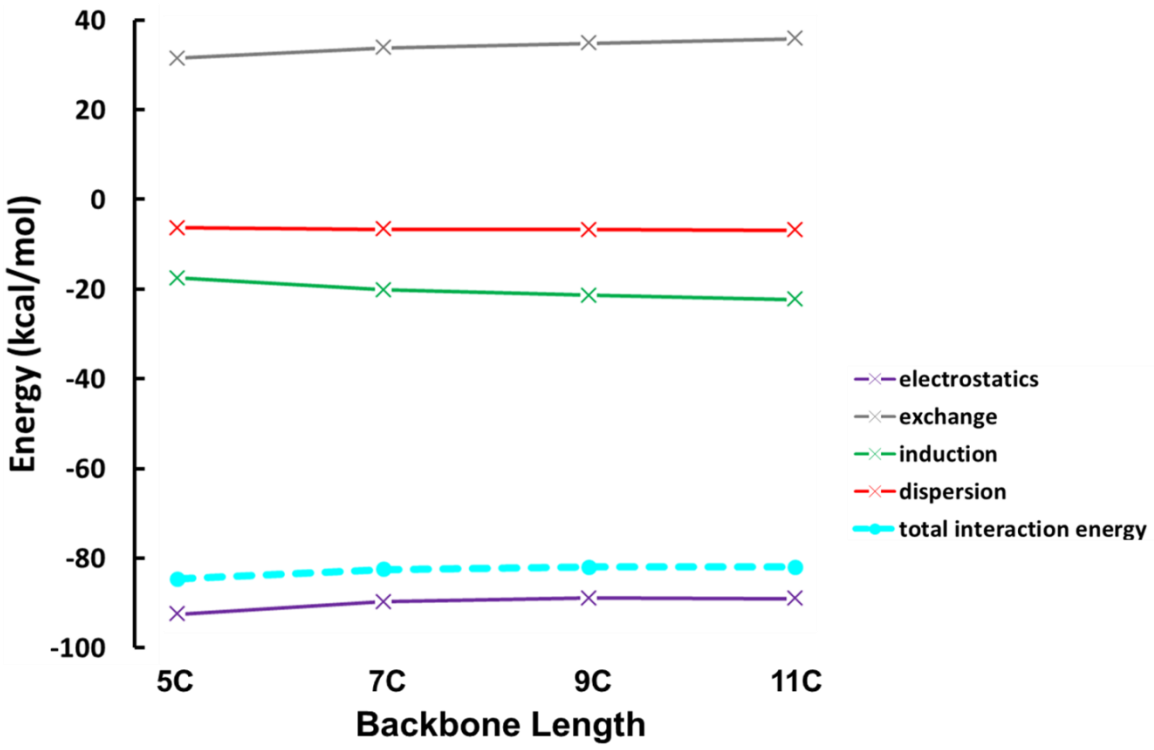

Figure 4.14: SAPT(0)/jun-cc-pVDZ total energies and their components in streptocyanine/Cl^- complexes as a function of backbone length, with the complexes fully optimized the at ωB97X/cc-pVDZ level.

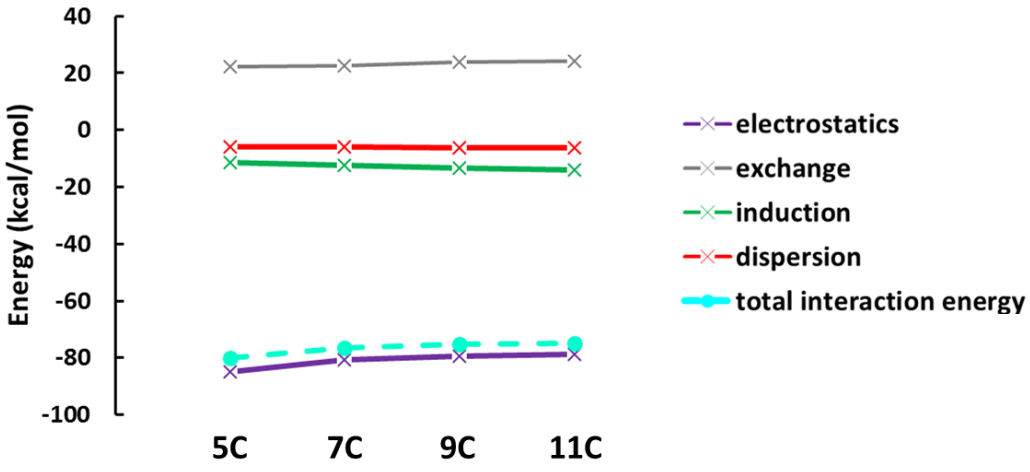

Figure 4.15: SAPT(0)/jun-cc-pVDZ total energies and their components in streptocyanine/BF_4^- complexes as a function of backbone length, with complexes fully optimized at the ωB97X/cc-pVDZ level.

4.4. Conclusions

In this Chapter, we have used a variety of computational techniques to investigate the non-covalent interactions between a series of streptocyanines of different backbone lengths (5C, 7C, 9C, 11C) and counterions of different sizes (Cl^- and BF_4^-). Potential energy surfaces were generated as a function of Cl^- counterion displacement along the backbone, and SAPT(0) was employed to study the evolution of the interactions over these displacements.

As expected, the degree of BLA as a function of increasing counterion displacement from the molecular center evolves in a smooth fashion from cyanine-like (BLA = 0.0 Å) to near polyene-like (BLA = 0.1 Å). However, at each counterion displacement the BLA is similar regardless of the length of the streptocyanine backbone, a situation markedly different from the BLA seen when a uniform electric field is applied. As the electric field of the counterion is highly localized and non-uniform, the molecular ends of the longer streptocyanine can see very different environments than shorter streptocyanines at the same displacement, and localized geometry distortions occur at the counterion location. Thus, the BLA depends on the counterion electric field and intrinsic polarizability of the streptocyanines, and both effects largely compensate one another to lead to the appearance of similar BLA. The differences between displacements near the energetic minimum along the potential energy surface are small enough that at room temperature the counterion has the freedom to move up to ~1 Å (in the case of BF_4^-) closer to the molecular end. The range of accessible displacements increases as the counterion size is increased, suggesting that the large tetraaryl counterion $[BAr^F{}_4]^-$ used experimentally can access many displacements along the backbone at room temperature. Thus, the degree of BLA in thin films can be larger than what is to be expected from consideration of the fully optimized complexes only.

The counterion contributes the most to symmetry breaking when it is near one molecular end of the streptocyanine. The SAPT(0) results confirm that electrostatics are largely responsible for the non-covalent interactions between the streptocyanine and counterion. The counterion is stabilized near one end of the backbone due to the increased localization of backbone charge by the counterion at that position. Comparison of the SAPT(0) energy analysis for each backbone length with the Cl^- and BF_4^- counterions reveals broad similarities and highlights that the interaction between the streptocyanine and counterion is a local effect. As the length of the streptocyanine backbone is increased, the binding energy between the streptocyanine and counterion decreases due to the an increased energetic penalty incurred by the backbone geometry distortions at the longer backbone lengths, suggesting that larger, bulkier cyanines may be more weakly bound to their counterions.

4.5. References

1. Bouit, P.-A.; Aronica, C.; Toupet, L.; Le Guennic, B.; Andraud, C.; Maury, O. Continuous symmetry breaking induced by ion pairing effect in heptamethine cyanine dyes: beyond the cyanine limit. *J. Am. Chem. Soc.* **2010**, *132*, 4328-4335.

2. Barlow, S.; Henling, L. M.; Day, M. W.; Marder, S. R. Effect of the end-groups upon delocalisation in polymethines: the first crystallographically characterised bond-alternated cyanine. *Chem. Commun.* **1999**, *16*, 1567-1568.

3. Dahne, L.; Reck, G. Deformation of polymethine structures by intermolecular interactions. *Angew. Chem. Int. Ed. Engl.* **1995**, *34*, 690-692.

4. Lepkowicz, R. S.; Przhonska, O. V.; Hales, J. M.; Fu, J.; Hagan, D. J.; Van Stryland, E. W.; Bondar, M. V.; Slominsky, Y. L.; Kachkovski, A. D. Nature of the electronic transitions in thiacarbocyanines with a long polymethine chain. *Chemical Physics* **2004**, *305*, 259-270.

5. Tolbert, L. M.; Zhao, X. Beyond the cyanine limit: peierls distortion and symmetry collapse in a polymethine dye. *J. Am. Chem. Soc.* **1997**, *119*, 3253-3258.

6. Mukhopadhyay, S.; Risko, C.; Marder, S. R.; Brédas, J.-L. Polymethine dyes for all-optical switching applications: a quantum-chemical characterization of counter-ion and aggregation effects on the third-order nonlinear optical response. *Chem. Sci.* **2012**, *3*, 3103-3112.

7. Wheately, P. J. 659. The crystallography of some cyanine dyes. *J. Chem. Soc.* **1959**, *0*, 3245-3250

8. Wheately, P. J., 821. The crystallography of some cyanine dyes. part ii. the molecular and crystal structure of the ethanol solvate of 3,3'-diethylthiacarbocyanine bromide. *J. Chem. Soc.* **1959**, *0*, 4096-4100

9. Honda, M.; Katayama, C.; Tanaka, J. Charge density distribution of a polymethine cyanine dye: (5-dimethylamino-2,4-pentadienylidene)dimethylammonium perchlorate. *Acta Crystallogr., Sect. B: Struct. Sci.* **1986**, *B42*, 90-95.

10. Gieseking, R. L.; Mukhopadhyay, S.; Shiring, S. B.; Risko, C.; Brédas, J.-L. Impact of bulk aggregation on the electronic structure of streptocyanines: implications for the solid-state nonlinear optical properties and all-optical switching applications. *J. Phys. Chem. C* **2014**, *118*, 23575-23585.

11. Gieseking, R. L.; Mukhopadhyay, S.; Risko, C.; Marder, S. R.; Brédas, J.-L. effect of bulky substituents on thiopyrylium polymethine aggregation in the solid state: a theoretical

evaluation of the implications for all-optical switching applications. *Chem. Mater.* **2014**, *26*, 6439-6447.

12. See also Chapter 3 of this Thesis.

13. Jacquemin, D. New cyanine dyes or not? theoretical insights for model chains. *J. Phys. Chem. A* **2011**, *115*, 2442-2445.

14. Jacquemin, D.; Chibani, S.; Le Guennic, B.; Mennucci, B. Solvent effects on cyanine derivatives: a PCM investigation. *J. Phys. Chem. A* **2014**, *118*, 5343-5348.

15. Jacquemin, D.; Zhao, Y.; Valero, R.; Adamo, C.; Ciofini, I.; Truhlar, D. G. Verdict: Time-dependent density functional theory "not guilty" of large errors for cyanines. *J. Chem. Theory Comput.* **2012**, *8*, 1255-1259.

16. Chai, J.-D.; Head-Gordon, M. Long-range corrected hybrid density functionals with damped atom–atom dispersion corrections. *Phys. Chem. Chem. Phys.* **2008**, *10*, 6615-6620.

17. Dunning, T. H. Gaussian basis sets for use in correlated molecular calculations. i. the atoms boron through neon and hydrogen. *J. Chem. Phys.* **1989**, *90*, 1007-1023.

18. Chai, J.-D.; Head-Gordon, M. Systematic optimization of long-range corrected hybrid density functionals. *J. Chem. Phys.* **2008**, *128*, 084106.

19. Gieseking, R. L.; Risko, C.; Bredas, J. L. Distinguishing the effects of bond-length alternation versus bond-order alternation on the nonlinear optical properties of pi-conjugated chromophores. *J. Phys. Chem. Lett.* **2015**, *6*, 2158-2162.

20. Boys, S. F.; Bernardi, F. The calculation of small molecular interactions by the differences of separate total energies. Some procedures with reduced errors. *Mol. Phys.* **1970**, *19*, 553-566.

21. Gaussian 09, Revision B.01, M. J. Frisch, G. W. Trucks, H. B. Schlegel, G. E. Scuseria, M. A. Robb, J. R. Cheeseman, G. Scalmani, V. Barone, B. Mennucci, G. A. Petersson, H. Nakatsuji, M. Caricato, X. Li, H. P. Hratchian, A. F. Izmaylov, J. Bloino, G. Zheng, J. L. Sonnenberg, M. Hada, M. Ehara, K. Toyota, R. Fukuda, J. Hasegawa, M. Ishida, T. Nakajima, Y. Honda, O. Kitao, H. Nakai, T. Vreven, J. A. Montgomery, Jr., J. E. Peralta, F. Ogliaro, M. Bearpark, J. J. Heyd, E. Brothers, K. N. Kudin, V. N. Staroverov, T. Keith, R. Kobayashi, J. Normand, K. Raghavachari, A. Rendell, J. C. Burant, S. S. Iyengar, J. Tomasi, M. Cossi, N. Rega, J. M. Millam, M. Klene, J. E. Knox, J. B. Cross, V. Bakken, C. Adamo, J. Jaramillo, R. Gomperts, R. E. Stratmann, O. Yazyev, A. J. Austin, R. Cammi, C. Pomelli, J. W. Ochterski, R. L. Martin, K. Morokuma, V. G. Zakrzewski, G. A. Voth, P. Salvador, J. J. Dannenberg, S. Dapprich, A. D. Daniels, O. Farkas, J. B. Foresman, J. V. Ortiz, J. Cioslowski, and D. J. Fox, Gaussian, Inc., Wallingford CT, 2010.

22. Papajak, E.; Zheng, J.; Xu, X.; Leverentz, H. R.; Truhlar, D. G. Perspectives on basis sets beautiful: seasonal plantings of diffuse basis functions. *J. Chem. Theory Comput. 2***011,** 7, 3027-3034.

23. "Psi4: An open-source ab initio electronic structure program," J. M. Turney, A. C. Simmonett, R. M. Parrish, E. G. Hohenstein, F. Evangelista, J. T. Fermann, B. J. Mintz, L. A. Burns, J. J. Wilke, M. L. Abrams, N. J. Russ, M. L. Leininger, C. L. Janssen, E. T. Seidl, W. D. Allen, H. F. Schaefer, R. A. King, E. F. Valeev, C. D. Sherrill, and T. D. Crawford, WIREs Comput. Mol. Sci. 2, 556 (2012). (doi: 10.1002/wcms.93).

24. Wernke, W.; Pfeiffer, M.; Johr, T.; Lau, A.; Grahn, W.; Johannes, H.-H.; Dahne, L. Increase and saturation of the third order hyperpolarizabilities in homologous series of symmetric cyanines. *Chem. Phys.* **1997**, *216*, 337-347.

25. Marder, S. R.; Gorman, C. B.; Meyers, F.; Perry, J. W.; Bourhill, G.; Bredas, J. L.; Pierce, B. M. A Unified description of linear and nonlinear polarization in organic polymethine dyes. *Science* **1994**, *265*, 632-635.

26. Meyers, F.; Marder, S. R.; Pierce, B. M.; Bredas, J. L. Electric field modulated nonlinear optical properties of donor-acceptor polyenes: sum-over-states investigation of the relationship between molecular polarizabilites and bond length alternation. *J. Am. Chem. Soc.* **1994**, *116*, 10703-10714.

CHAPTER 5

ASSESSMENT OF FRONT-SUBSTITUTED ZWITTERIONIC CYANINE POLYMETHINES FOR ALL-OPTICAL SWITCHING APPLICATIONS

5.1. Introduction

Translating these promising molecular properties into useful materials with the large densities required for functional devices at the macroscale has, however, been challenging. We recall that in a thin film the charge of a cyanine unit must be balanced by the presence of a counterion. Environmental effects and cyanine-counterion interactions can induce geometric changes of the cyanine backbone which negatively impact NLO properties. The presence of the counterion can lead to ion-pairing, where the counterion and backbone charge tend to localize towards one end of the cyanine and induce symmetry breaking, which results in a molecular structure with large BLA.[1-4] Symmetry-broken molecules effectively become polyene-like, with substantial TPA, elimination the OPA-TPA energetic window, and a reduction in $\mathrm{Re}(\gamma)$.[1, 5-6] Thus, it is critical to minimize the counterion's ion-pairing effect and subsequent symmetry-breaking in order to preserve the molecular NLO properties of cyanines and to realize materials suitable for AOS applications.

Results from experimental and theoretical studies have suggested using bulky counterions, such as the tetraaryl-borate anion, as a strategy to mitigate the ion-pairing effect.[1-2, 7-8]

Another strategy is to covalently attach the counterion to the center of the cyanine backbone to create a zwitterionic cyanine-counterion structure. In this context, Li *et al.* have recently synthesized a zwitterionic cyanine-cyanine salt and found it to have reduced ion-pairing-induced charge localization compared to related complementary cyanine salts.[9] Here, our goal is to undertake a theoretical assessment of the performance of zwitterionic structures as a means to eliminate the need for a separate counterion and therefore eliminate the detrimental effects of ion-pairing. To that end, we examine a series of zwitterionic heptamethine cyanines, see Figure 5.1, based on a cationic heptamethine thiopyrylium backbone. As thin films of heptamethine thiopyrylium dyes have met or exceeded the required FOM,[10] they serve as an excellent molecular starting point to probe how modifications can lead to either enhancement or diminishment of their promising molecular properties. To further highlight our conclusions, we investigate additionally the effect of changing the backbone by studying a cationic pyridinium zwitterionic cyanine, as well as zwitterionic cyanines based on the anionic tricyanofuran backbone (**TCF**).

The zwitterionic cyanine structures investigated here (Figure 5.1) consist of a rigid π-conjugated substituent attached to the central carbon atom of the cyanine backbone, with a charge opposite to that on the backbone. The chemical makeup of the substituent has been selected to preserve the zwitterionic character of the molecule and to minimize any perturbation to the electronic structure of the heptamethine thiopyrylium backbone. This decoupling of the substituent and backbone is intended to be achieved by introducing an aromatic phenyl ring with electron withdrawing groups (**A**) to hold the negative charge. Side groups at the **R** and **R'** positions, see Figure 5.1, serve to introduce bulk to the

substituent to prevent it from attaining planarity (and thus increased electronic coupling) with the backbone.

We begin our discussion with an evaluation of how the addition of charged substituents as a function of the identity of **A** modifies the electronic structure of the backbone. We then characterize what effect this has on the excited-state spacing and $\mathrm{Re}(\gamma)$.

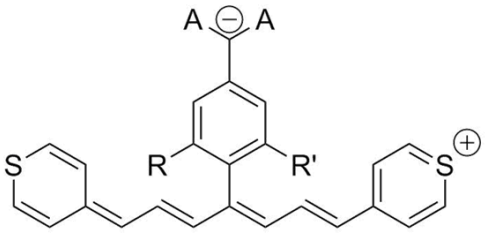

Compound	A	R	R'
1	no substituent		
2	F	CH_3	CH_3
3	Cl	CH_3	CH_3
4	Br	CH_3	CH_3
5	CF_3	CH_3	CH_3
6	COOH	CH_3	CH_3
7	COH	CH_3	CH_3
8	CN	CH_3	CH_3
9	COCl	CH_3	CH_3
10	CN	H	H
11	CN	CH_3	H
12	CN	^{t}bu	H
13	CN	^{t}bu	^{t}bu

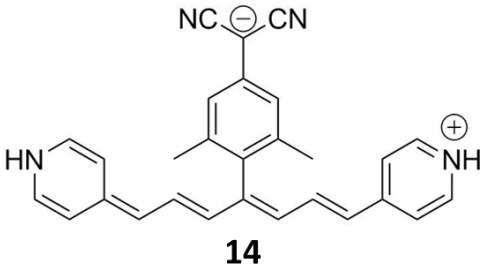

14

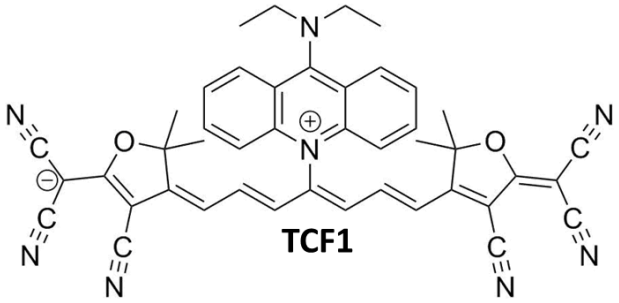

TCF1

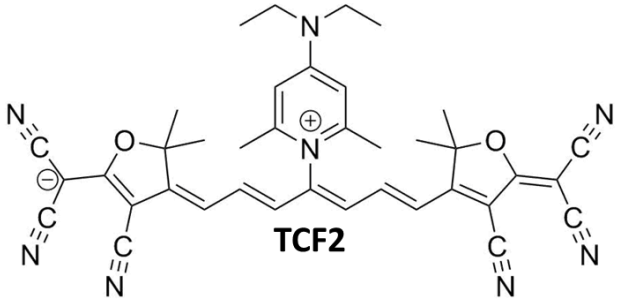

TCF2

Figure 5.1: Chemical structures of heptamethine thiopyrylium cyanine **1**, of zwitterionic cyanines **2 – 12,** of pyridinium zwitterionic cyanine **14,** and tricyanofuran zwitterionic cyanines **TCF1** and **TCF2**.

5.2. Computational Methodology

All geometry optimizations were performed in Gaussian 09 (revision B.01).[11] Isolated ground-state geometries were optimized with the long-range corrected ωB97X-D functional[12-13] at the default ω (ω = 0.2 $Bohr^{-1}$) value and the cc-pVDZ basis set[14]. Compound **8** was additionally re-optimized by considering an implicit dielectric medium within the polarizable continuum model for ε values ranging from corresponding to heptane (ε = 1.91) to corresponding to water (ε = 78.36), in order to approximate the surrounding effects. The absence of imaginary frequencies was used to confirm that the optimized geometries correspond to minima on the ground-state potential energy surface (PES). Atomic charges were calculated through natural bond order analysis. The linear and nonlinear optical properties were calculated using a methodology we have extensively and successfully applied to many π-conjugated systems;[5-8, 15-16] it is based on a configuration-interaction (CI) approach incorporating single and double excitations (SDCI) with the INDO Hamiltonian. The CI active space included all single-electron excitations within the 30 highest-lying occupied molecular orbitals (MOs) and 30 lowest-lying unoccupied MOs, and all double-electron excitations within the 4 highest-lying MOs and 4 lowest-lying unoccupied MOs. The bond-length alternation (BLA) was calculated as the average of the difference between adjacent carbon-carbon bonds along the backbone. Re(γ) were computed using a sum-over-states perturbation approach, summing over 950 excited states.[17]

5.3. Results and Discussion

5.3.1. Impact on Molecular Geometry

Since the third-order NLO properties depend strongly upon the molecular geometry of the cyanine, it is critical to evaluate the effect the addition of a charged substituent has on the molecular geometry. To do so, we consider several structural parameters evaluated from the optimized geometries, as identified in Figure 5.2. These include the torsion angle between the substituent and the backbone (θ), the dihedral angle between both ends of the backbone (φ), the BLA of the backbone, and the amount of charge on the substituent (δ_s). We note that in the unsubstituted thiopyrylium (compound **1**) the backbone is planar (ϕ = 0.01°), the charge (δ_s) is +1, and the thiopyrylium chain is symmetric (BLA = 0.004). The net charge on the backbone can in fact evolve as a function of the electron-acceptor strength of the substituent.

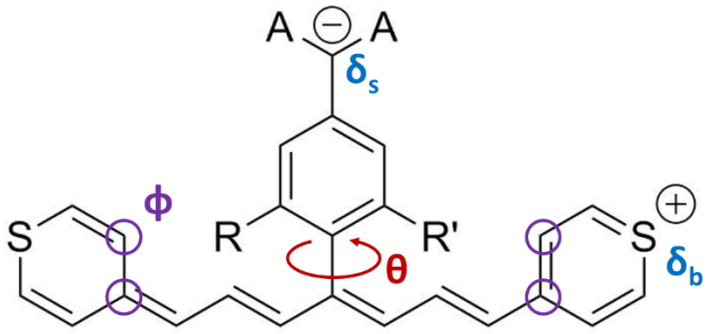

Figure 5.2: Model zwitterionic thiopyrylium, with the relevant geometric parameters indicated: substituent-backbone torsion angle (θ), backbone torsion angle (φ), and substituent and backbone charges (δ_s and δ_b, respectively).

We begin our discussion by considering the isolated compounds in vacuum (ε = 1). The molecular geometry and charge distribution depend strongly on the chemical nature of the substituent. A range of geometries and charge distributions is obtained as shown in Table 5.1, as a function of the identity of the acceptor **A** in substituents with **R** = **R'** = methyl groups (compounds **1**-**9**). We highlight that the BLA values span from polyene-like (BLA ~ 0.1 Å) for weak electron acceptors **A** to cyanine-like (BLA ~ 0 Å) for strong electron acceptors **A**. As the molecular NLO properties correlate to BLA, this suggests that the prototypical cyanine properties are lost for substituents that are weak electron acceptors, as they fail to preserve the zwitterionic charge of the molecule.

Table 5.1: Substituent-backbone torsion angle (θ), backbone dihedral angle (φ), BLA, and charge *remaining* on the substituent (δ_s) for the electron withdrawing groups investigated.

Compound	A	θ (°)	φ (°)	BLA (Å)	δ_s(|e|)
1	—	—	0.01	0.004	—
2	F	40.0	50.6	0.072	-0.026
3	Cl	41.6	47.7	0.067	-0.13
4	Br	41.9	46.7	0.066	-0.15
5	CF_3	45.6	35.9	0.056	-0.35
6	COOH	46.9	34.9	0.056	-0.35
7	COH	49.0	32.7	0.048	-0.44
8	CN	51.0	29.8	0.045	-0.49
9	COCl	90.0	0.64	0.01	-1.0

For substituents that are comparatively weak (*e.g.*, **A** = F in Figure 5.2), a negligible net charge remains on the substituent ($\delta_s \sim 0$). As the electron acceptor strength of **A** increases, more negative charge remains on the substituent and reaches unity in the case of the strong electron acceptor COCl in compound **9**. Weaker electron acceptors energetically favor charge recombination between cyanine backbone and substituent; the formal charges no longer remain localized on their respective moieties but partially or fully combine via electron transfer from the nominally anionic substituent to the nominally cationic thiopyrylium backbone. The changes in electron acceptor strength alter the charge distribution, which in turn drives geometric differences, as indicated by the BLA values.

This charge recombination provides a driving force for geometry distortions. As the strength of the electron acceptor is decreased and more charge recombines at the central backbone position, the C-C bond between the backbone and substituent shortens, as it takes on increased double-bond character (Table 5.2). Likewise, the bond between the electron acceptor moiety and the substituent increases in double-bond character, leading to the substituent phenyl ring to adopt a quinoidal-like geometry (QBC, Table 5.2). The quinoidal-benzene character, QBC, is defined as $\sum_i\left(\left|r_i - 1.4\ \text{Å}\right|\right)$, where r_i is the length of each C-C bond *i* in the phenyl ring (Figure 5.3). For the series of compounds investigated, the QBC ranges from large and quinoidal (0.33, **2**) to small and benzene-like (0.04, **9**). Accordingly, the dihedral angel θ between the backbone and substituent strongly decreases from 90° down to 40° as δ_s goes from -1.00 down to -0.03 (**A** = COCl to **A** = F), steric interactions preventing the whole molecule from becoming more coplanar.

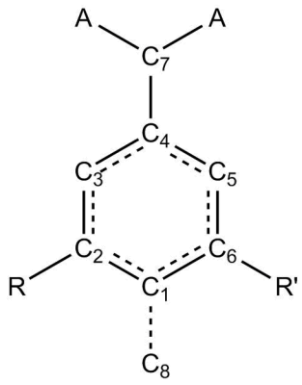

Figure 5.3: Molecular structure of substituent with atoms labeled. Atom C_8 corresponds to the central carbon atom of thiopyrylium backbone.

Table 5.2: Substituent phenyl bond lengths, in Angstroms. QBC denotes the quinoidal-benzene character.

Compound	**2**	**3**	**4**	**5**	**6**	**7**	**8**	**9**
$C_1 - C_2$	0.076	0.068	0.067	0.054	0.052	0.046	0.043	0.006
$C_2 - C_3$	0.044	0.041	0.041	0.035	0.033	0.029	0.027	0.008
$C_3 - C_4$	0.047	0.048	0.049	0.044	0.041	0.037	0.027	0.006
$C_4 - C_5$	0.047	0.048	0.049	0.044	0.040	0.037	0.027	0.006
$C_5 - C_6$	0.044	0.041	0.041	0.036	0.033	0.029	0.027	0.007
$C_6 - C_1$	0.076	0.068	0.066	0.055	0.053	0.046	0.044	0.006
QBC:	**0.33**	**0.31**	**0.31**	**0.27**	**0.25**	**0.22**	**0.20**	**0.04**
$C_1 - C_8$	1.40	1.41	1.41	1.42	1.42	1.43	1.44	1.50
$C_4 - C_7$	1.34	1.36	1.36	1.39	1.40	1.41	1.41	1.48

With these changes in bond lengths, the backbone becomes composed of essentially two short polyene-like segments, one on either side of the central carbon, which are cross-

conjugated through this central carbon and display pronounced double-single bond alternation (Figure 5.4). Thus, these short polyene-like segments have a symmetric pattern of single bond-double bond pattern emanating from the central carbon. It is worth nothing that a similar observation has been made experimentally, where a strong electron-donating substituent chemically bonded to the central carbon atom in a 5-carbon cyanine dye was found to profoundly modify he ground-state backbone BLA to favor a geometry similar to the right of Figure 5.4.[18]

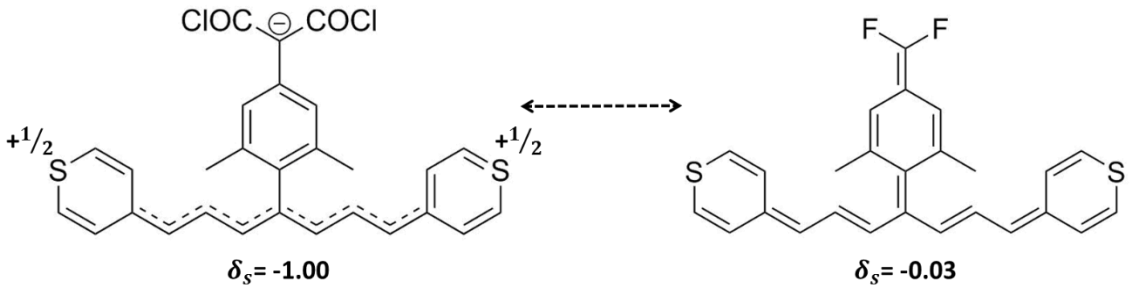

Figure 5.4: Illustration of the change in molecular geometry as δ_s decreases in magnitude.

As mentioned above, a consequence of the charge recombination and subsequent reduction in backbone-substituent bond length is a small backbone-substituent torsion angle (θ) as the substituent and backbone attempt to become co-planar. Weak electron acceptors **A** lead to a substituent-backbone torsion angle far from perpendicular. Smaller torsion angles have negative consequences for the NLO properties, as discussed in the following sections. Also, small θ angles bring the hydrogen atoms on the substituent's methyl groups close to the hydrogen atoms on the backbone. The backbone then distorts significantly by twisting (increase in φ) to minimize the steric repulsion. The result of these geometry changes is the

loss of C_{2V} symmetry and the adoption of a geometry that is not the prototypical cyanine geometry, a situation which becomes disadvantageous for AOS applications. A clear example of geometry differences can be seen by comparing compounds **2** and **9**. Compound **2**, with F as electron acceptor **A**, has essentially zero charge remaining on the substituent, leading to a torsion angle of only ~40° and a severely distorted backbone (φ ~ 50°), yielding polyene-like BLA. Although the dihedral angle θ reaches a minimum in the case of **2**, as mentioned earlier, the substituent is prevented from achieving full planarity with the backbone due to the bulky substituents at **R** and **R'**. The situation is markedly improved in **9**, where the COCl electron acceptor retains full charge separation, which maintains prototypical cyanine-like geometry (θ = 90°, φ ~ 0°, BLA cyanine-like) on the backbone.

The potential energy surfaces (PES) as a function of substituent torsion angle for **2** and **9** are significantly different from one another (Figure 5.5). The PES of **2,** centered at θ = 40°, is sharper and steeper than **9**, and reaches a maximum at θ = 90° of ~20 kcal/mol. Due to the substituent being unable to rotate any less than 30°, the PES of **2** is strongly asymmetric as it is easier to increase θ than it is to decrease it; at room temperature, thermal energy affords only ~5° of rotation. The PES of **9,** on the other hand, is broader and shallower; it is minimized at θ = 90° and reaches a maximum (~20 kcal/mol) when the substituent becomes much more parallel to the backbone (θ = 30° and θ = 150°). Importantly, thermal energy allows a rotation of only some 10° at room temperature, implying that the substituent remains mostly perpendicular.

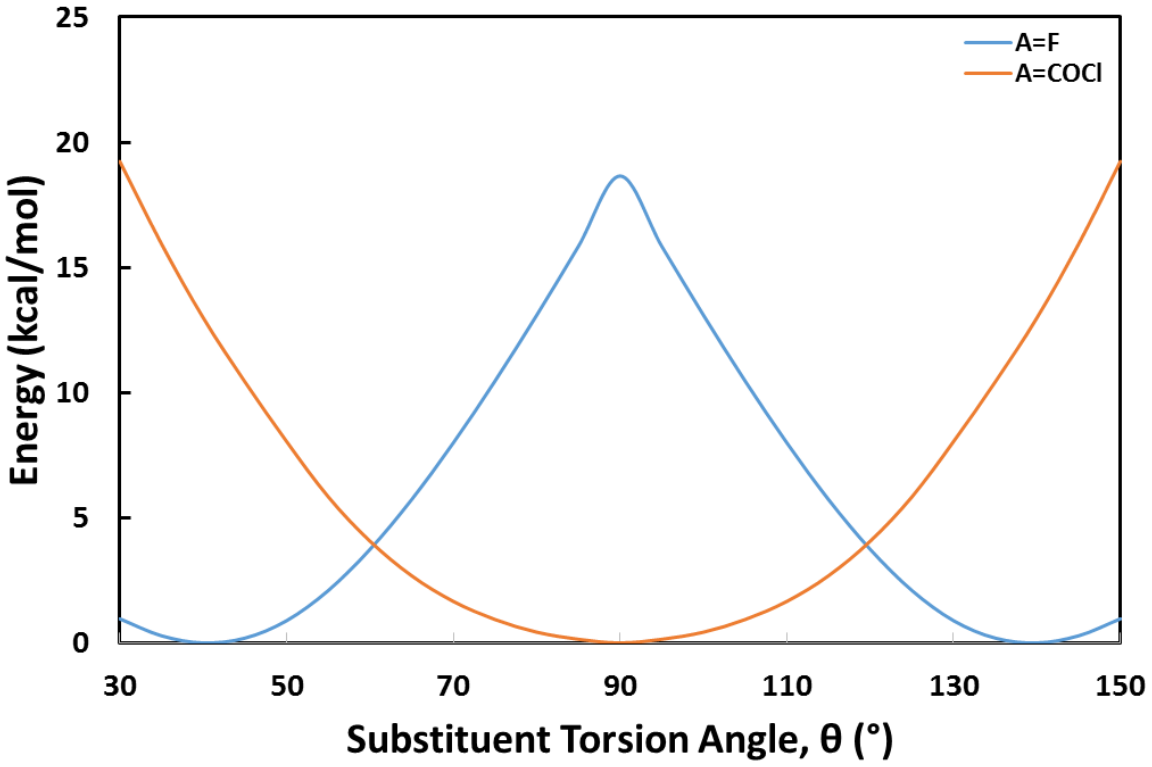

Figure 5.5: Potential energy surfaces as a function of substituent torsion angle (θ) for A=F (compound **2**) and A=COCl (compound **9**)

As sterics play a key role in determining the backbone geometry and aid in preventing the substituent from gaining full planarity with the backbone, we next consider to what extent changing the steric bulk of the substituent impacts the θ angle. Increasing or decreasing the steric bulk is a common strategy available to control molecular geometry. Compound **8**, with the cyano electron acceptor, was selected as it afforded, see Table 5.1, the largest torsion angle among the systems with θ not perpendicular; the substituent was modified at the R and R' positions by either decreasing its bulkiness (*e.g.*, removal of methyl side groups in **10**) or increasing its bulkiness (addition of t-butyl groups in **13**). The structural parameters corresponding to these modifications are collected in Table 5.3.

As expected, decreasing the steric bulk in the series **10**-**12** leads to a reduction in the torsion angle θ. When the methyl side groups on the substituent are replaced with H atoms, the fact that the substituent can approach more closely to the backbone in turn leads to a large backbone torsion φ. For compound **10**, containing the smallest sterically bulky substituent (**R** = **R'** = H), θ is about30°, which is nearly 20° less than in **8.** As the size of the **R** and **R'** side groups become larger across the series **10**-**13**, the minimum θ angle increases, φ decreases, and BLA is reduced. Substituent charge retention, δ_s, also correlates with side-group size: less charge is retained with H atoms (-0.41 |e|) at the side groups than with the largest t-butyl groups (-0.68 |e|). Across this series, the BLA values are smaller and occur over a narrower range compared to the series **2**-**9**. Across the series **10**-**13**, with the increase in bulkiness, θ increases, φ decreases, and BLA is reduced. The addition of the t-butyl groups in **13** brings θ the closest to perpendicular at $\theta \sim 70°$. While increasing the bulkiness does increase θ and lead to more charge retention, the substituent's steric bulkiness alone is not sufficient to force the substituent to become perpendicular when it is not electronically favorable to do so.

Table 5.3: Structural parameters for modified substituent sterics as determined at the ωB97X-D/cc-pVDZ level of theory.

Compound	A	R	R'	θ (°)	φ (°)	BLA (Å)	δ_s(|e|)
8	CN	Me	Me	51.0	29.8	0.045	-0.49
10	CN	H	H	29.9	46.4	0.058	-0.41
11	CN	Me	H	39.6	37.6	0.052	-0.44
12	CN	t-butyl	H	59.0	21.4	0.038	-0.62
13	CN	t-butyl	t-butyl	68.8	12.7	0.031	-0.68

We now turn to considering the impact of an implicit solvent to gain an understanding of what effect the medium plays. While ε in thin films of guest:host thiopyrylium:amorphous polycarbonate (APC) is expected to be around 2.72-2.89 depending on cyanine loading concentration, it is of interest to examine the impact of a full range of dielectric constants. Taking again **8** as a representative example compound, we optimized its geometry in a series of solvents of increasing dielectric strength (Table 5.4). Moving from vacuum to a heptane-like medium (ε = 1.91) results in an increase in θ by nearly 10°, with δ_s jumping in magnitude from -0.49 to -0.88 |e|. Increasing further the dielectric constant leads to θ approaching 90° and a reduction in $\varphi$and BLA, giving a nearly C_{2V} symmetric structure. A Chloroform-like medium (ε = 4.71) is enough to retain charge separation ($\delta_s \sim 1$) and promote a favorable cyanine-like geometry, while a DCM-like medium (ε = 8.93) leads to a near perpendicular θ torsion angle and a tiny ϕ backbone torsion. Dielectric constants stronger than a DCM (*e.g.*, ethanol and water) do not substantially improve upon the geometry obtained in a DCM-like medium. Strong dielectric constants contribute to screen the substituent and backbone charges from one another, and the charges remain localized on their respective moieties. Thus, the shielding afforded by the dielectric medium overcomes the charge recombination driving force and the substituent remains perpendicular. The importance message here is that the presence of a strong dielectric medium helps maintain the prototypical cyanine geometry.

Table 5.4: Structural parameters under implicit solvent as determined at the ωB97X-D/cc-pVDZ level of theory for compound **8** (A = CN, R = R' = Me).

Medium	ε	θ (°)	φ (°)	BLA (Å)	δ_s (|e|)
Vacuum	1	51.0	29.8	0.045	-0.49
Heptane	1.91	60.9	20.0	0.028	-0.88
Chloroform	4.71	82.7	4.8	0.012	-0.96
DCM	8.93	86.7	1.9	0.011	-0.96
Ethanol	24.85	87.4	1.2	0.0098	-0.96
Water	78.36	87.6	0.9	0.0095	-0.97

5.3.2. Effect on Molecular Orbitals

Having described the effect the addition of a charged substituent has on the molecular geometry, we now discuss its impact on the frontier molecular orbitals that are most relevant for the description of the optical properties. The degree of π-orbital mixing between the substituent and backbone naturally depends on the substituent-backbone torsion angle, with diminished π-orbital mixing when θ is large. As we discussed earlier, θ depends on the charge distribution and whether it is favorable for the zwitterionic charges to recombine. The driving force for charge recombination can be further understood by examining the frontier MOs of the isolated anionic substituent and cationic backbone. To illustrate this point, we examine in more detail the cases of compounds **2** and **9**, for which $\theta = 40°$ and $\theta = 90°$ in vacuum, respectively.

The amount of charge recombination (and concurrently the magnitude of θ) is in fact related to the energetic difference between the HOMO of the isolated substituent and the

LUMO of the isolated thiopyrylium ($\Delta E_{(H-L)}$ in Table 5.5). For **2**, the substituent HOMO lies much higher in energy than the thiopyrylium LUMO, nearly 3.9 eV higher. When $\Delta E_{(H-L)}$ is large, there is a strong driving force that can overcome the phenyl ring aromaticity and induce charge transfer from the electrons in the substituent HOMO to the lower lying thiopyrylium LUMO. When this charge transfer occurs, the substituent phenyl ring gains a quinoid character, and substituent rotates to become more coplanar with the thiopyrylium backbone (θ decreases), where it induces geometry distortions (φ increases). Indeed, as $\Delta E_{(H-L)}$ becomes larger, the molecule retains less zwitterionic character due to increased transfer of charge.

Table 5.5: Structural parameters correlated to difference in energy ($\Delta E_{(H-L)}$) between the HOMO of the isolated anionic substituent and the LUMO of the isolated cationic thiopyrylium, which is calculated to be -4.72 eV. All values evaluated at the ωB97X-D/cc-pVDZ level of theory with ε = 1.

Compound	**A**	**θ (°)**	**HOMO energy (eV)**	**$\Delta E_{(H-L)}$ (eV)**
2	F	40.0	-0.83	3.89
3	Cl	41.5	-1.68	3.04
4	Br	41.9	-1.90	2.82
5	CF3	45.9	-2.49	2.23
6	COOH	46.8	-2.67	2.05
7	COH	49.0	-2.63	2.09
8	CN	51.0	-2.61	2.11
9	COCl	90.0	-4.22	0.5

The HOMO and LUMO of **2** are thus found to be a mixture of the isolated anionic substituent HOMO and isolated cationic thiopyrylium LUMO (Figure 5.6). These MOs reflect the charge distribution discussed previously: cross-conjugation between the π-orbitals on the thiopyrylium backbone and the π-orbitals on the substituent can be observed at the central carbon atom. The substituent phenyl ring has lost its aromatic character, adopting quinoidal character with increased density across the carbon atoms which have taken on increased double-bond character. The isolated cationic thiopyrylium's HOMO becomes the HOMO-1 of the zwitterionic cyanine, while the LUMO+1 of the isolated cationic thiopyrylium becomes the LUMO+1 of the zwitterionic cyanine. These orbitals are essentially unmodified. The HOMO of the isolated substituent is the only MO to participate among the frontier MOs of the zwitterionic cyanine.

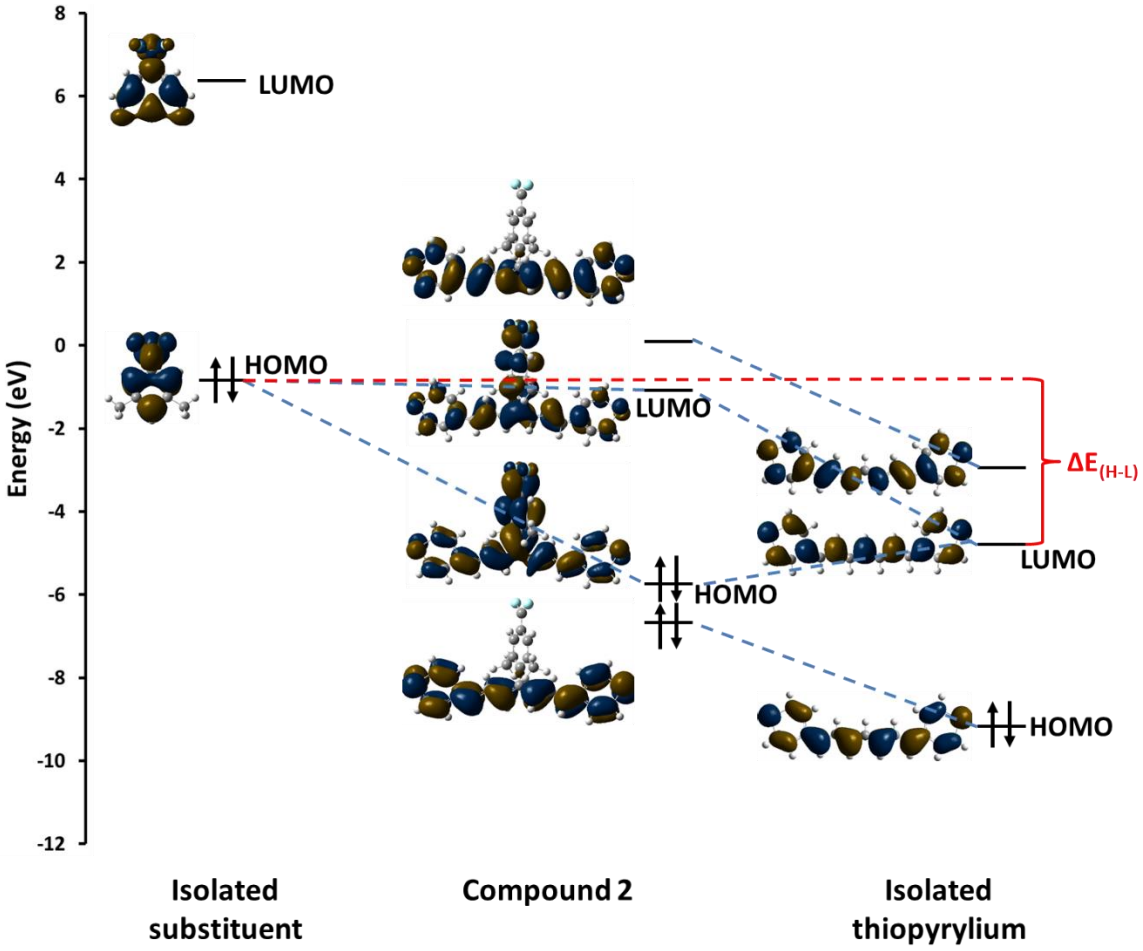

Figure 5.6: Molecular orbital correlation diagram for compound **2** (A = F), showing the formation of the whole-molecule orbitals from the isolated-moiety orbitals. $\Delta E_{(H-L)}$ indicates the energetic difference between the HOMO of the isolated anionic substituent and the LUMO of the isolated cationic thiopyrylium.

As the HOMO energy of the isolated anionic substituent approaches the LUMO energy of the isolated cationic thiopyrylium, charge recombination decreases and the substituent increasingly becomes more perpendicular. Thus, when this energetic difference, $\Delta E_{(H-L)}$, is small or negative, we can expect the zwitterionic cyanine to adopt a C_{2V} symmetric geometry with the substituent perpendicular. For charge separation to be maintained, however, $\Delta E_{(H-L)}$ does not have to be negative (*i.e.*, the isolated cationic thiopyrylium's

LUMO energy does not need to be greater than the isolated anionic substituent's HOMO energy) since electrostatic interactions and through-bond interactions between the two moieties significantly shift he orbital energies upon formation of the complex. As stronger electron acceptors are substituted onto the isolated anionic substituent, its HOMO energy approaches that of the isolated cationic thiopyrylium's LUMO. This situation is fulfilled in compound **9**, see Figure 5.7, where the $\Delta E_{(H-L)}$ is small (0.5 eV) and the isolated anionic substituent's HOMO is nearly isoenergetic with the isolated cationic thiopyrylium's LUMO (Figure 5.7). Since the driving force for recombination becomes small, the orbitals do not mix; instead the isolated anionic substituent's HOMO becomes the new HOMO of **9**. The isolated anionic substituent's HOMO has electron density centered on the electron withdrawing group, preserving the phenyl ring's aromaticity.

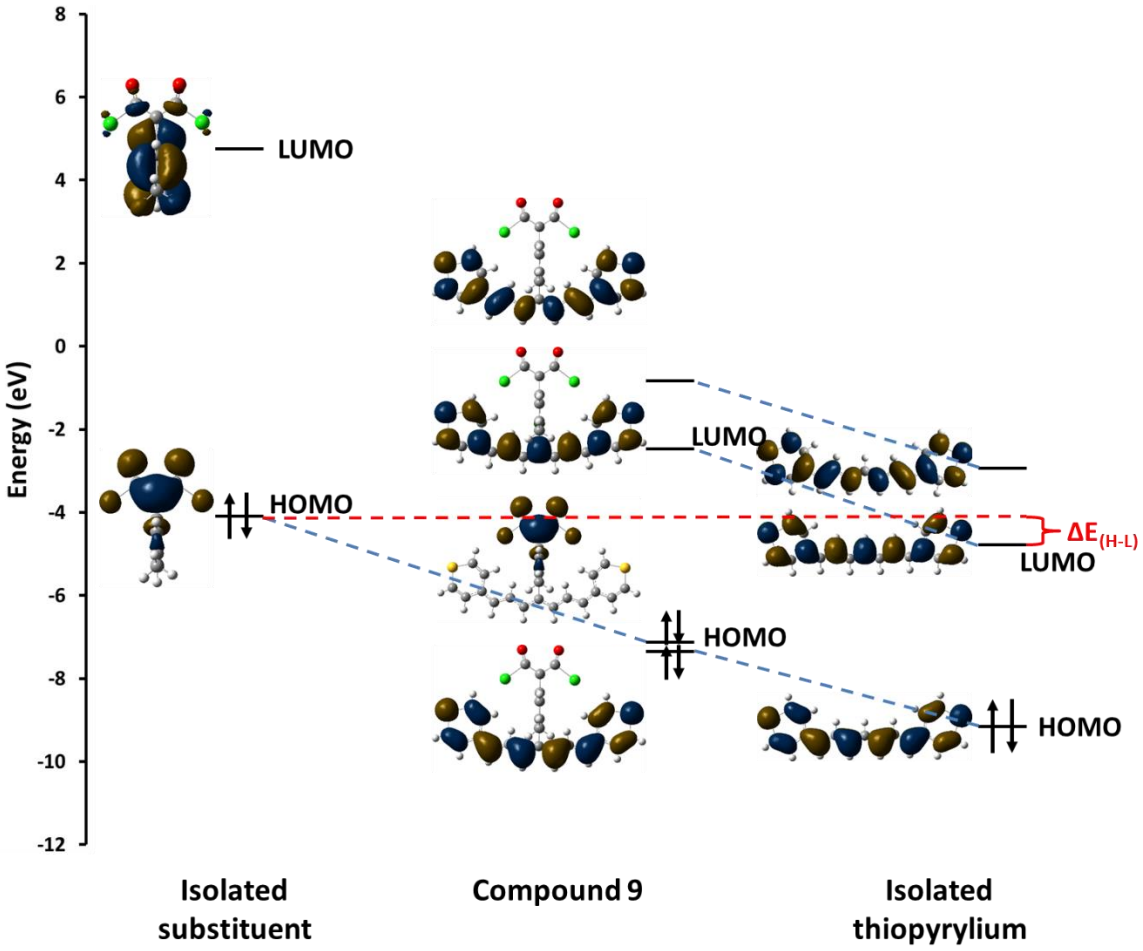

Figure 5.7: Molecular orbital correlation diagram for compound (**9**) (A = COCl), showing formation of new orbitals from isolated moiety orbitals. $\Delta E_{(H-L)}$ indicates the energetic difference between the HOMO of the isolated anionic substituent and the LUMO of the isolated cationic thiopyrylium.

The relationship between the torsion angle and $\Delta E_{(H-L)}$ is further demonstrated by considering another cationic (pyridium, **14**) and an alternate anionic (tricyanofuran **TCF**, Table 5.6) cyanine backbone. Table 5.6 collects structural data for both (**14**) and **TCF**-based zwitterionic cyanine.

For **14**, with an isolated pyridium LUMO of -3.87 eV, $\Delta E_{(H-L)}$ is 1.25 eV, leading to θ = 64.9° and φ = 14.9°. Compared to **8** with the same electron acceptor, the smaller $\Delta E_{(H-L)}$ increases the backbone-substituent torsion angle by over 10° and reduces the backbone dihedral angle by nearly 15°. In the zwitterionic tricyanofuran **TCF1** and **TCF2**, we must consider the energetic difference between the HOMO of the isolated anionic TCF backbone and LUMO of the isolated cationic substituent.

Table 5.6: Structural parameters for pyridium-based compound **14** and TCF-based zwitterionic cyanines, **TCF1** and **TCF2**. $\Delta E_{(H-L)}$ is difference in energy between HOMO/LUMO of isolated substituent and HOMO/LUMO of isolated backbone for pyridium/TCF-based zwitterions. "HOMO/LUMO energy" corresponds to HOMO/LUMO energy of isolated substituent for pyridium/TCF compounds. For reference, the isolated pyridium backbone LUMO energy is -3.87 eV and the isolated TCF backbone HOMO energy is -4.57 eV.

Compound	**θ (°)**	**φ (°)**	**BLA**	**δ_s**	**HOMO energy (eV)**	**$\Delta E_{(H-L)}$ (eV)**
14	-64.64	-14.94	0.019	-0.80	-2.61	1.25
Compound	**θ (°)**	**φ (°)**	**BLA**	**δ_s**	**LUMO energy (eV)**	**$\Delta E_{(H-L)}$ (eV)**
TCF1	89.58	-0.44	0.026	0.65	-4.96	0.39
TCF2	88.24	-1.02	0.026	0.67	-3.18	-1.38

$\Delta E_{(H-L)}$ in **TCF1** is small and positive (0.39 eV) and in **TCF2** is negative (-1.38 eV, *i.e.*, the isolated substituent LUMO lies below the isolated TCF backbone). In both compounds the substituent is perpendicular to the backbone and the backbone itself remains planar, and no mixing of the frontier molecular orbitals occurs (Figure 5.8). Thus, judicious

selection of backbone and substituent is required to ensure proper energetic matching to maintain the prototypical cyanine geometries.

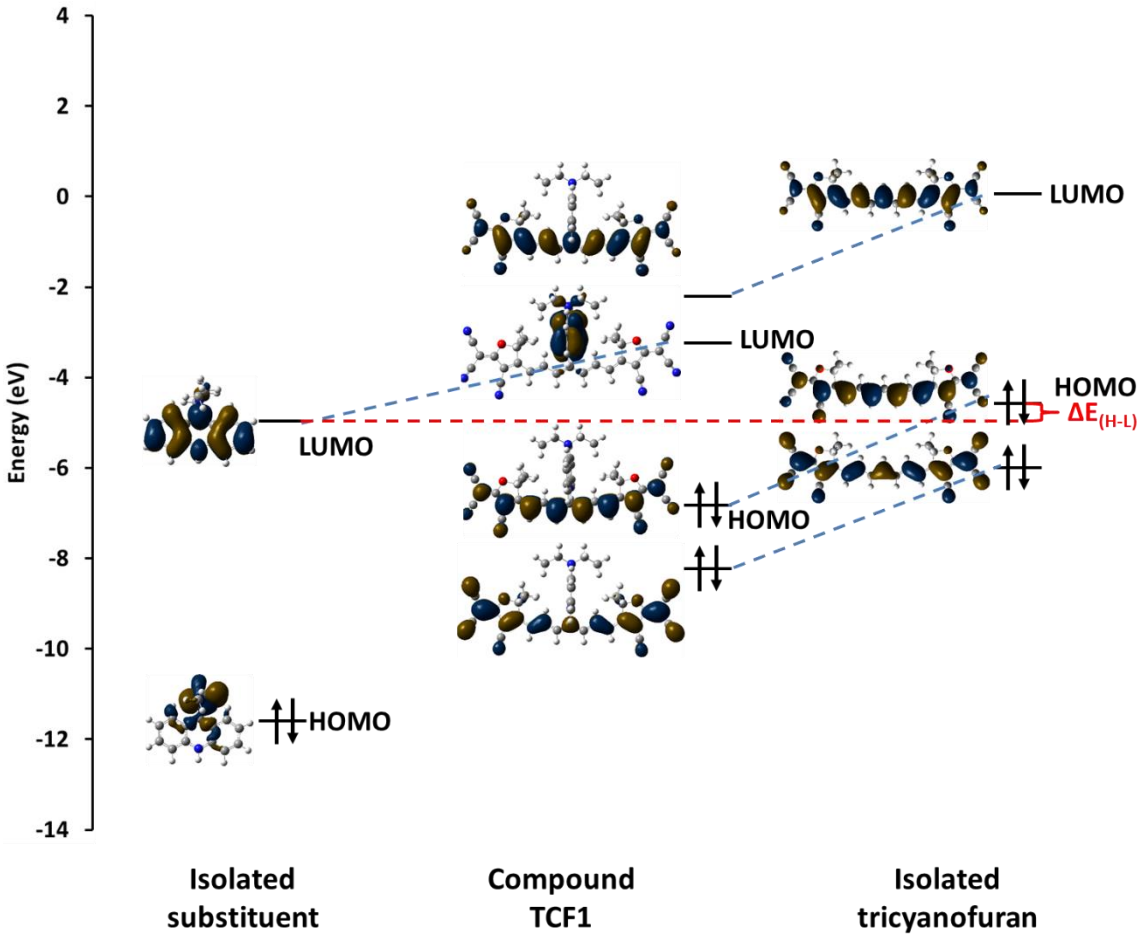

Figure 5.8: Molecular orbital correlation plot for compound **TCF1**.

5.3.3. Excited-States Properties and Third-Order Polarizability

As suggested by the wide range of BLA values upon the choice of electron acceptor **A**, the third-order NLO properties are diverse. Figure 5.9 presents the lowest lying excited states

and their character for selected compounds at specific angles of θ, while Table 5.7 collects the vertical excitation energies, transition dipole moments, differences in state dipole moments, and $\mathrm{Re}(\gamma_{\mathrm{static}})$ values at the static limit ($\hbar\omega$ = 0.0 eV) for all compounds considered in this chapter. The unsubstituted thiopyrylium **1** is included for comparison, and only its OPA and TPA states are listed; we note that due to its large transition dipole moment between the ground state and OPA state and low OPA state energy, the **N** term, in which μ_{ge}^4 appears, dominates the SOS expression and the static γ is thus large and negative. Understanding within the context of the SOS expression how these properties change with changes in molecular structure allows valuable chemical insight into γ.

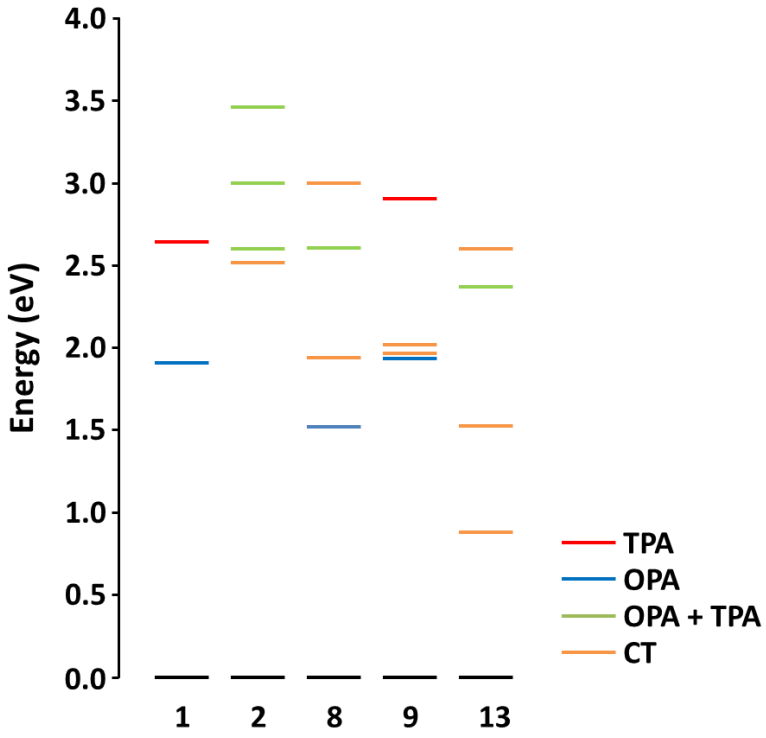

Figure 5.9: Lowest lying excited state energies and their state character.

In general, the addition of the charged substituent introduces low-lying charge transfer (CT) states for many systems. As the HOMO and LUMO of the zwitterionic cyanine is a mixture of the isolated anionic substituent HOMO and isolated cationic thiopyrylium LUMO, excitations among the frontier MOs involve transfers between substituent-based and thiopyrylium-based orbitals. In **9**, where the HOMO is localized on the substituent and the LUMO is localized on the thiopyrylium, the HOMO → LUMO transition is expected to be strongly charge transfer in character.

In compounds with small torsion angles (*e.g.*, **2**) and mixing of the backbone and substituent π-systems, several important changes occur to the excited states and properties of interest for NLO. The low-lying states are destabilized to higher energy relative to the unsubstituted thiopyrylium (**1**) and have reduced transition dipole moments. Differences in state dipole moments between the ground state and excited state enlarge, compared to the unsubstituted thiopyrylium. Given the lower symmetry, these states are no longer distinctly an OPA or TPA state, but take on a combination of OPA and TPA character; importantly, the optical transparency window is lost. In these compounds, the first excited state becomes a CT state, involving an excitation from HOMO to LUMO+1. As expected, the CT transition is optically weak, with a small transition dipole moment (μ_{ge}) of 1.12 Debye in **2**. The electronic transition of this CT state involves a change in state dipole moments ($\Delta\mu_{ge}$) of 2.11 Debye. The larger excited-state energies, reduced μ_{ge}, and increased $\Delta\mu_{ge}$ lead to a large and positive Re(γ_{static}) in these systems as the N term no longer dominates the three-term model.

For intermediate values of θ (*e.g.*, **6**, **7**, and **8**), cyanine-like NLO properties begin to be recovered. The first excited state regains OPA character with moderate transition dipole

moment strength, and the combination of OPA/TPA states begin to be dominated by a single CT excitation. However, since the geometry is distorted and the HOMO and LUMO are delocalized across the backbone and substituent, large changes in state dipole moments upon excitation to the excited states are still present. Compound **8**, with θ = 51.0°, has the largest positive $\mathrm{Re}(\gamma_{\mathrm{static}})$ (2.36 x10^{3} x10^{-36} esu), attributed to the large differences between state dipole moments, which leads to a large D term in the three-state model.

Prototypical cyanine-like NLO properties are regained with a strong electron acceptor. In compound **9**, with complete separation of the π-systems and θ = 90°, the states are distinctly OPA and TPA again. While the OPA state is comparable in energy to the OPA state of the unsubstituted thiopyrylium, the TPA state is destabilized, leading to a broadening of the optical transparency window. While two charge transfer states are located between the OPA and TPA states, they are not optically active, possessing negligible transition dipole moments. $\mathrm{Re}(\gamma_{\mathrm{static}})$ becomes again large and negative due to the large first excited-state transition dipole moment and low state energy.

Compounds **10** through **13** follow similar trends for their values of θ as described above. Without changing the chemical identity of the acceptor, increasing θ leads to a lowering of the first two excited-states energies. While increasing the substituent steric bulk drives θ closer to perpendicular, the character of the lowest excited states increasingly becomes a CT state, and the molecule adopts an increasing ground-state diradical character. The diradical character of the ground state is maximized in **13**, with t-butyl groups substituted at the R and R' positions, as the ground-state CI description includes not only the SCF determinant but also a determinant describing the HOMO→LUMO excitation, which is CT in character coupled through a doubly excited determinant with a small CI contribution.

The Re(γ_{static}) values in compounds **10** through **12** are positive, which is attributed to a large changes in state dipole moments, while in **13** it is small and negative. This reinforces the importance of selecting a chemical structure where the charge separation is electronically driven and not purely due to sterics to obtain cyanine-like NLO properties.

To round out the comparison, we finally consider **TCF1** and **TCF2**. Both **TCF1** and **TCF2** are similar in description to **9**, in that the selection of a substituent with a strong electron donor with the TCF backbone maintains electronic separation and thus θ is at 90°. Distinct OPA and TPA states are present, preserving the optical transparency window with a width of ~1 eV. Again, the charge substituent introduces a low-lying CT state and CT states within the optical transparency window, but these are not optically active. In both compounds, $\mathrm{Re}(\gamma_{\mathrm{static}})$ is large and negative.

Table 5.7: Vertical excitation energy E (eV), transition dipole moment μ_{ge} (Debye), and differences in state dipole moment $\Delta\mu_{ge}$ (Debye) between excited states and ground state. Real part of the static third-order polarizability $\mathrm{Re}(\gamma_{static})(10^{-36}$ esu).

compound	E_1 (μ_{01}) [$\Delta\mu_{01}$]	E_2 (μ_{02}) [$\Delta\mu_{02}$]	E_3 (μ_{03}) [$\Delta\mu_{03}$]	E_4 (μ_{04}) [$\Delta\mu_{04}$]	$\mathrm{Re}(\gamma_{stat})$
1	1.90 (18.67) [0.24]	2.64 (1.22) [2.22]	*	*	-7.76 x10^3
2	2.51 (1.12) [2.11]	2.59 (3.73) [1.09]	3.00 (5.40) [0.41]	3.45 (1.48) [2.78]	1.24 x10^3
3	2.44 (5.00) [2.20]	2.45 (0.81) [2.71]	2.60 (0.97) [8.91]	2.94 (4.57) [0.27]	1.34 x10^3
4	2.23 (0.90) [9.81]	2.42 (5.09) [2.38]	2.42 (0.88) [2.71]	2.92 (4.62) [0.11]	1.35 x10^3
5	2.06 (5.95) [3.47]	2.23 (0.56) [3.55]	2.78 (3.36) [1.39]	3.30 (12.43) [3.82]	1.74 x10^3
6	1.81 (7.74) [3.47]	2.23 (0.12) [4.90]	2.75 (3.20) [3.03]	3.13 (12.52) [5.56]	1.85 x10^3
7	1.50 (9.27) [2.10]	2.09 (0.06) [7.07]	2.69 (3.28) [5.32]	2.90 (12.78) [7.25]	0.925 x10^3
8	1.52 (8.31) [4.66]	1.94 (0.76) [5.58]	2.60 (3.17) [4.12]	3.00 (12.81) [6.81]	2.36 x10^3
9	1.95 (16.34) [0.18]	1.97 (0.01) [8.93]	2.01 (0.55) [25.10]	2.90 (1.34) [2.16]	-7.76 x10^3
10	2.03 (8.05) [2.52]	2.39 (0.10) [4.76]	2.82 (4.12) [1.92]	3.23 (12.27) [5.81]	1.72 x10^3
11	1.80 (8.13) [3.02]	2.19 (0.41) [5.38]	2.73 (3.70) [3.07]	3.13 (12.52) [5.97]	1.88 x10^3
12	1.30 (7.18) [1.00]	1.96 (1.15) [7.27]	2.61 (3.56) [5.49]	2.82 (12.07) [3.47]	0.883 x10^3
13	0.88 (9.00) [5.41]	1.52 (1.49) [6.78]	2.37 (1.86) [6.67]	2.60 (11.09) [8.66]	-0.594x10^3
14	0.83 (7.76) [10.18]	1.78 (1.73) [14.62]	2.12 (15.37) [2.81]	2.64 (0.67) [16.02]	-0.738x10^3
TCF1	0.73 (0.27) [15.75]	1.78 (19.30) [1.95]	2.00 (0.04) [14.47]	2.25 (0.51) [14.54]	-17.9 x10^3
TCF2	1.62 (1.08) [14.85]	1.73 (20.08) [2.14]	2.48 (0.71) [13.84]	2.51 (1.77) [3.22]	-13.9 x10^3

5.4. Conclusions

Developing novel materials for AOS applications requires an understanding of how modifying chemical structures impacts properties of interest to NLO and subsequently $Re(\gamma_{static})$. Here, we investigated the suitability of zwitterionic cyanines that are designed to eliminate the need for a counterion and prevent counterion-pairing interactions for use in AOS devices. The ability of the charged substituent to retain its charge and maintain the zwitterionic structure is critical to preserve the advantageous third-order NLO properties inherent to cationic cyanines upon formation of a zwitterion.

For substituents with weak electron acceptors, anionic charge leaks from the substituent into the cyanine backbone. This modified ground-state charge distribution introduces electronic coupling between the backbone and substituent. This is reflected by the substituent-backbone torsion angle: for compounds where less charge is retained on the substituent, the substituent becomes increasingly planar with the backbone. This leads to mixing between the frontier orbitals, and geometric distortions along the backbone become pronounced, together with an increase in BLA. This charge recombination can be further rationalized by considering the energy difference between the LUMO of the isolated cationic backbone and the HOMO of the isolated anionic substituent; a small energetic difference between these orbitals is essential to minimize charge recombination. The substituent's steric bulkiness alone is not sufficient to keep the substituent perpendicular for substituents with weaker electron acceptors.

Structures that show significant charge recombination have excited states that are markedly different from the unsubstituted thiopyrylium: the states are no longer distinctly OPA or

TPA, but a combination of both, with the consequence that the optical transparency window has vanished. Re(γ_{static}) in these compounds is large and positive. For zwitterionic structures where the charges remain separate and the substituent is perpendicular to the backbone, the charged substituent introduces CT states between the OPA and TPA states, but these are not optically active. As these systems resemble the unsubstituted thiopyrylium, Re(γ_{static}) remains large and negative.

We find that compound **9**, with its substituent containing a strong electron acceptor and moderate bulk, leads to the positive charge remaining on the thiopyrylium backbone and the negative charge remains on the substituent (δ_s= 1). No coupling between the frontier orbitals of the cyanine and substituent occurs, and the substituent remains perpendicular to the backbone. The ground-state geometry, excited-state, and NLO properties resemble those of the unsubstituted thiopyrylium. Charge separation between backbone and substituent must be favored electronically to preserve the unsubstituted thiopyrylium properties valuable for AOS applications; and that failure to do so can have profound, detrimental effects upon these properties.

5.5. References

1. Mukhopadhyay, S.; Risko, C.; Marder, S. R.; Brédas, J.-L. Polymethine dyes for all-optical switching applications: a quantum-chemical characterization of counter-ion and aggregation effects on the third-order nonlinear optical response. *Chemical Science* **2012,***3*, 3103-3112.

2. Bouit, P.-A.; Aronica, C.; Toupet, L.; Le Guennic, B.; Andraud, C.; Maury, O. Continuous symmetry breaking induced by ion pairing effect in heptamethine cyanine dyes: beyond the cyanine limit. *J. Am. Chem. Soc.* **2010,** *132*, 4328-4335.

3. Bambgelu, A.; Wang, J.; Leszczynski, J. TDDFT study of the optical properties of cy5 and its derivatives. *J. Phys. Chem. A* **2010,** *114*, 3551-3555.

4. Karaman, R.; Menger, F. M. Electrostatic effects on the energetics and geometry of a cyanine dye. *Journal of Molecular Structure: THEOCHEM* **2010,** *959*, 87-91.

5. Marder, S. R.; Gorman, C. B.; Meyers, F.; Perry, J. W.; Bourhill, G.; Bredas, J. L.; Pierce, B. M. A unified description of linear and nonlinear polarization in organic polymethine dyes. *Science* **1994,** *265*, 632-635.

6. Meyers, F.; Marder, S. R.; Pierce, B. M.; Bredas, J. L. Electric field modulated nonlinear optical properties of donor-acceptor polyenes: sum-over-states investigation of the relationship between molecular polarizabilites and bond length alternation. *J. Am. Chem. Soc.* **1994,** *116*, 10703-10714.

7. Gieseking, R. L.; Mukhopadhyay, S.; Shiring, S. B.; Risko, C.; Brédas, J.-L. Impact of bulk aggregation on the electronic structure of streptocyanines: implications for the solid-state nonlinear optical properties and all-optical switching applications. *J. Phys. Chem. C* **2014,** *118*, 23575-23585.

8. Hales, J. M.; Matichak, J.; Barlow, S.; Ohira, S.; Yesudas, K.; Bredas, J. L.; Perry, J. W.; Marder, S. R. Design of polymethine dyes with large third-order optical nonlinearities and loss figures of merit.*Science* **2010,** *327*, 1485-1488.

9. Li, Z.; Zhao, P.; Tofighi, S.; Sharma, R.; Ensley, T. R.; Jang, S.-H.; Hagan, D. J.; Van Stryland, E. W.; Jen, A. K.-Y. Zwitterionic cyanine-cyanine salt: structure and optical properties. *J. Phys. Chem. C* **2016,** *120*, 15378-15384.

10. Barlow, S.; Brédas, J.-L.; Getmanenko, Y. A.; Gieseking, R. L.; Hales, J. M.; Kim, H.; Marder, S. R.; Perry, J. W.; Risko, C.; Zhang, Y., Polymethine materials with solid-state

third-order optical susceptibilities suitable for all-optical signal-processing applications. *Mater. Horiz.* **2014,** *1*, 577-581.

11. Gaussian 09, Revision B.01, M. J. Frisch, G. W. Trucks, H. B. Schlegel, G. E. Scuseria, M. A. Robb, J. R. Cheeseman, G. Scalmani, V. Barone, B. Mennucci, G. A. Petersson, H. Nakatsuji, M. Caricato, X. Li, H. P. Hratchian, A. F. Izmaylov, J. Bloino, G. Zheng, J. L. Sonnenberg, M. Hada, M. Ehara, K. Toyota, R. Fukuda, J. Hasegawa, M. Ishida, T. Nakajima, Y. Honda, O. Kitao, H. Nakai, T. Vreven, J. A. Montgomery, Jr., J. E. Peralta, F. Ogliaro, M. Bearpark, J. J. Heyd, E. Brothers, K. N. Kudin, V. N. Staroverov, T. Keith, R. Kobayashi, J. Normand, K. Raghavachari, A. Rendell, J. C. Burant, S. S. Iyengar, J. Tomasi, M. Cossi, N. Rega, J. M. Millam, M. Klene, J. E. Knox, J. B. Cross, V. Bakken, C. Adamo, J. Jaramillo, R. Gomperts, R. E. Stratmann, O. Yazyev, A. J. Austin, R. Cammi, C. Pomelli, J. W. Ochterski, R. L. Martin, K. Morokuma, V. G. Zakrzewski, G. A. Voth, P. Salvador, J. J. Dannenberg, S. Dapprich, A. D. Daniels, O. Farkas, J. B. Foresman, J. V. Ortiz, J. Cioslowski, and D. J. Fox, Gaussian, Inc., Wallingford CT, 2010.

12. Chai, J.-D.; Head-Gordon, M. Systematic optimziation fo long-range corrected hybrid density functionals. *J. Phys. Chem.* **2008**, *128,* 084106.

13. Chai, J.-D.; Head-Gordon, M.Long-range corrected hybrid density functionals with damped atom–atom dispersion corrections. *Phys. Chem. Chem. Phys.* **2008**, *10,* 6615-6620.

14. Dunning, T.H. Gaussian basis sets for use in correlated molecular calculations. I. The atoms boron through neon and hydrogen. *J. Chem. Phys.* **1989**, *90,* 1007-1023.

15. Albota, M.; Beljonne, D.; Bredas, J. L.; Ehrlich, J. E.; Fu, J. Y.; Heikal, A. A.; Hess, S. E.; Kogej, T.; Levin, M. D.; Marder, S. R.; McGord-Maughon, D.; Perry, J. W.; Rockel, H.; Rumi, M.; Subramaniam, C.; Webb, W. W.; Wu, X. L.; Xu, C. Design of organic molecules with large two-photon absorption cross sections. *Science* **1998**, *281,* 1653-1656.

16. Kogej, T.; Beljonne, D.; Meyers, F.; Perry, J. W.; Marder, S. R.; Bredas, J. L. Mechanisms for enhancement of two-photon absorption in donor–acceptor conjugated chromophores. *Chem. Phys. Lett.* **1998**, *298,* 1-6.

17. Orr, B. J.;Ward, J. F. Perturbation theory of the non-linear optical polarization of an isolated system. *Mol. Phys.* **1971**, *20,* 513-526.

18. Pascal, S.; Haefele, A.; Monnereau, C.; Charaf-Eddin, A.; Jacquemin, D.; Le Guennic, B.; Andraud, C.; Maury, O. Expanding the polymethine paradigm: evidence for the contribution of a bis-dipolar electronic structure. *J. Phys. Chem. A* **2014**, *118*, 4038-4047.

CHAPTER 6

THE THIRD-ORDER NONLINEAR OPTICAL PROPERTIES OF MIXED-STACK ORGANIC CHARGE-TRANSFER COMPLEXES

6.1. Introduction

Interest in organic materials for use in NLO applications, particularly with regard to their third-order optical response, has been focused primarily on linear π-conjugated systems, such as cyanines[1-5] and (donor-acceptor) polyenes.[1-2, 6] Although cyanines possess the largest γ among linear π-conjugated systems, at long chain lengths cyanines break symmetry and γ is reduced. Recently, investigation of multicomponent organic systems such as binary charge-transfer (CT) complexes has suggested that these materials could afford new opportunities for organic electronics.[7-8] Early experimental studies of CT complexes reported large third-order susceptibilities;[9] in particular, large nonreasonant γ values on the order of 10^{-32} esu were measured for crystals of perylene tetracyanoethylene (Pe/TCNE) and pyrene tetracyanoethylene (Py/TCNE).[10]

Binary CT complexes are composed of two components: one molecule which acts as a donor (D) and another molecule which acts as an acceptor (A). For complexes with 1:1 stoichiometry, two crystal structure motifs are observed: segregated-stack and mixed-stack (left and right, Figure 6.1). In segregated-stack systems, there are separate, adjacent stacks of the donor and acceptor molecules; in mixed-stack systems, the donor and acceptor molecules stack alternatively along the stacking direction.

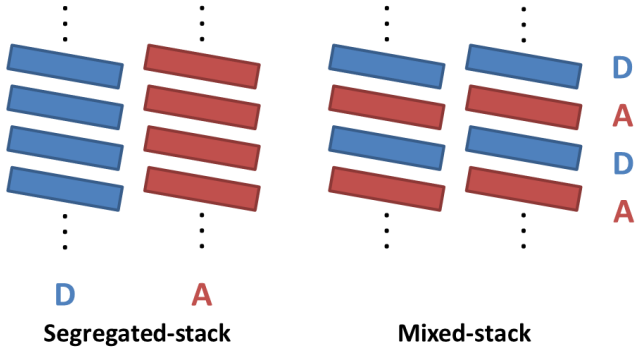

Figure 6.1: Cartoon illustrating segregated-stack (left) and mixed-stack (right) structures in 1:1 stoichiometry CT complexes.

These bimolecular crystals possess potential advantages that make them attractive to consider for NLO applications such as AOS:

1. The ability to form crystalline materials in which the component molecules are arranged in a highly ordered manner; as discussed in the Introduction, cyanines are known to strongly aggregate often uncontrollably at high concentrations, which severely modifies their molecular properties and limits their utility for AOS.
2. Low excited-state energies, due to their CT nature; small excited-state energies lead to smaller denominators in the SOS expression, which enhances γ.
3. A very long long-axis; an electron could be delocalized over several repeat units along the CT axis within the crystal, leading to a substantial induced dipole moment (recall $\mu = er$, where r is the displacement), without worrying about symmetry-breaking effects.

While limited experimental studies on the third-order optical response of CT complexes have been performed, the only computational work reported to date has focused on

understanding the second-order NLO response of a few complexes (which we are not considering here). A molecular understanding of γ in these systems has not been discussed, yet it is desirable when designing systems for device applications. To gain such an understanding and to benefit from the features listed above, we have chosen to investigate the seven following mixed-stack CT complexes: DBTTF-TCNQ (dibenzotetrathiafulvalene tetracyanoquinodimethane)[11], DMQtT-F4TCNQ (dimethylquaterthiophene tetracyanoquinodimethane)[12], Pe-TCNE (perylene tetracyanoethylene)[13], Py-TCNE (pyrene tetracyanoethylene)[14], TTF-CA HT (the high temperature phase of tetrathiafulvalene p-chloranil)[15], TTF-CA LT (the low temperature phase of tetrathiafulvalene p-chloranil)[15], and Py-TCNQ (pyrene tetracyanoquinodimethane)[16]. We have selected Pe/TCNE, Py/TCNE, and Py-TCNQ as the long-axis third-order molecular polarizabilities or electric susceptibilities ($\chi^{(3)}$) have been previously measured for these complexes;[9-10] DBTTF-TCNQ and DMQtT-F4TCNQ were chosen because crystals of these have shown good charge transport properties both experimentally and theoretically.[17-20] TTF-CA has been included as a good benchmark, since it undergoes a neutral-to-ionic phase transition with a lowering of symmetry at low temperature.

The chemical structures of the investigated complexes are presented below (Figure 6.2). We begin with a discussion of the NLO response of the individual monomer units, then build towards small clusters by considering dyads composed of one D and A component, triads composed of D-A-D or A-D-A components, and a parallel stack composed of two adjacent D-A stacks in order to understand the magnitude and sign of γ.

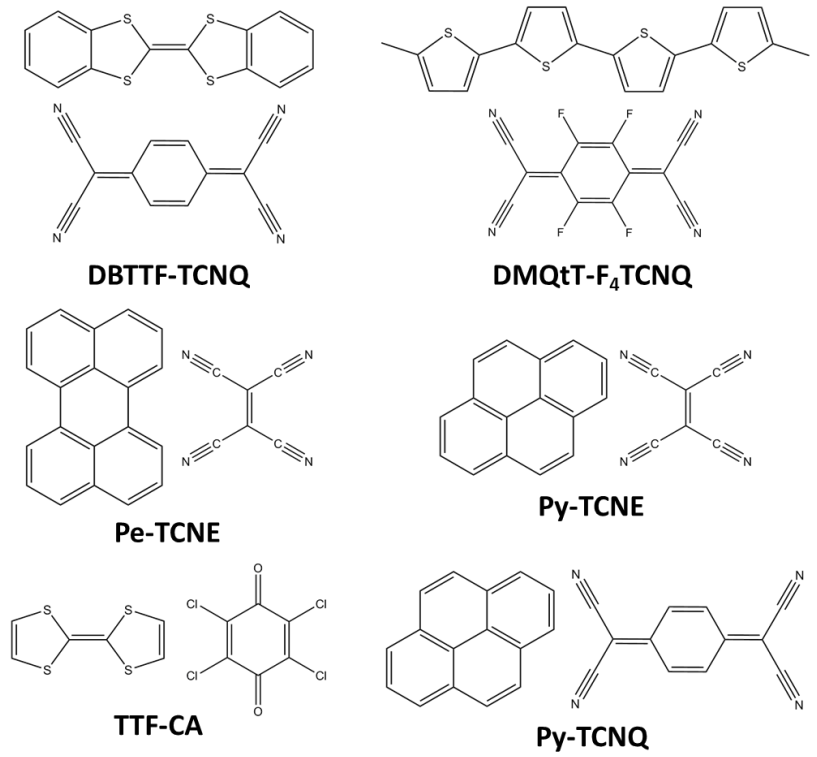

Figure 6.2: Molecular structures of the investigated CT complexes and abbreviations for the names.

6.2. Theoretical Methodology

The excited-state properties (*e.g.*, transition energies and dipole moments) to serve as input for the SOS calculations of γ were evaluated at the TD-DFT level. These calculations were performed on the isolated molecules. The 50 lowest singlet excited states were calculated using the B3LPY[21-22] functional with the 6-31G basis set. All TD-DFT calculations were performed with Gaussian 09, Revision D.01.[23] The transition dipole moments between all excited states of interest were obtained at the end of the TD-DFT calculation with the Multiwfn code (version 3.3.7).[24]

The geometries for the excited-state calculations were taken from the Crystallographic Information File (.cif) obtained from the Cambridge Structural Database files for each CT complex. Geometries include the individual monomers, the D-A dyad, D-A-D and A-D-A triads, and a parallel stack of 2 D-A dyads (see Figure 6.3). For the D-A dyad configuration, the geometries of molecules from the unit cell were taken. For the triads, the additional D or A molecule was stacked along the CT direction. For the parallel stack configurations, the unit cell was expanded until a D-A pair from an adjacent stack was obtained.

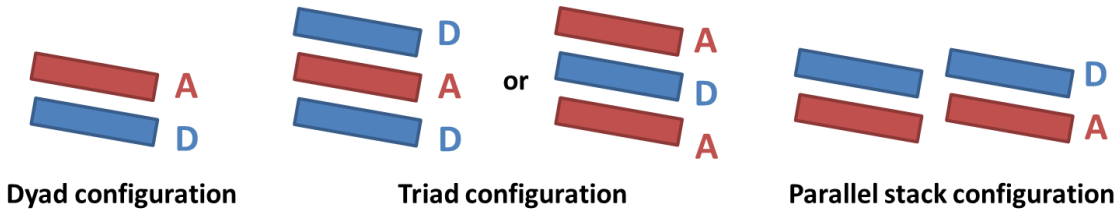

Figure 6.3: Schematics depicting configurations of dyads, triads, and parallel stacks.

A minimum state model was used to calculate the static γ values via the SOS formalism; the γ values were decomposed into their axial tensor components ($\gamma_{xxxx}, \gamma_{yyyy}, \gamma_{zzzz}$) and into contributions from the **D**, **T**, and **N** terms corresponding to the three-state model (see eq. 1.4 in Chapter 1). The number of excited states considered within the SOS procedure for each CT complex was chosen to ensure γ to converge. We define an internal set of coordinates (Figure 6.4) such that the *x* direction corresponds to the CT direction, the *y* direction corresponds to the molecular long axes, and the *z* direction corresponds to the molecular short axis.

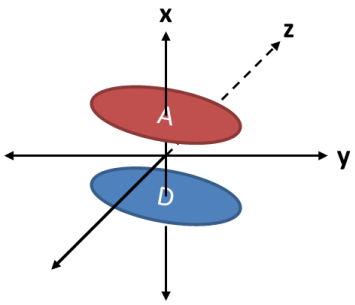

Figure 6.4: Illustration of the internal coordinate system.

As we evaluate γ at the static limit (ħω=0), Im(γ) is zero and thus we focus on Re(γ) (reported as γ). The orientationally averaged γ is computed from the tensor components as:

$$\gamma_{avg} = \frac{1}{5}\left(\gamma_{xxxx} + \gamma_{yyyy} + \gamma_{zzzz}\right) + \frac{1}{15}\left(\gamma_{xxyy} + \gamma_{yyxx} + \gamma_{xyyx} + \gamma_{xyxy} + \gamma_{yxyx} + \gamma_{yxxy} + \gamma_{xxzz} + \gamma_{zzxx} + \gamma_{xzzx} + \gamma_{xzxz} + \gamma_{zxzx} + \gamma_{zxxz} + \gamma_{zzyy} + \gamma_{yyzz} + \gamma_{zyyz} + \gamma_{zyzy} + \gamma_{yzyz} + \gamma_{yzzy}\right) \quad (6.1)$$

6.3. Results

6.3.1. Third-Order Optical Response of Monomers

In order to assess whether the third-order optical response in the CT complexes arises from the intermolecular interactions between donor and acceptor molecules in the complex/crystal or from the third-order response of the individual monomers, the responses

of the individual monomers were calculated for later comparison with the dyads and triads (Table 6.1).

Table 6.1: Average γ values (γ_{avg}) and tensorial components γ_{xxxx}, γ_{yyyy}, and γ_{zzzz} for the individual monomers involved in the CT complexes. All values reported in 10^{-36} esu.

CT complex	Monomer	γ_{avg}	γ_{xxxx}	γ_{yyyy}	γ_{zzzz}
DBTTF-TCNQ	DBTTF	137	0.144	128	211
	TCNQ	127	0.622	146	60.3
DMQtT-F_4TCNQ	DMQtT	2.90×10^3	0.0	1.45×10^4	8.48×10^{-3}
	F_4TCNQ	94.1	34.1	96.1	78.0
Pe-TCNE	Pe	120	6.44	319	68.2
	TCNE	5.03	0.704	7.36	3.20
Py-TCNE	Py	19.1	1.81	42.1	23.5
	TCNE	5.29	1.91	6.71	0.232
Py-TCNQ	Py	19.1	1.81	42.1	23.5
	TCNQ	131	2.05	350	26.1
TTF-CA HT	TTF	7.35	7.88	12.6	0.423
	CA	6.51	8.71	0.369	9.95
TTF-CA LT	TTF	7.10	6.37	29.4	0.00
	CA	6.40	3.79	0.00	24.7

Many of the individual monomers possess a calculated γ_{avg} on the order of 10^{-36} esu. For those with an appreciable response at 10^{-34} esu (DBTTF, TCNQ, DMQtT, and Pe), the tensor along the molecular long-axis contributes the most to γ_{avg}; indeed, γ_{avg} of DMQtT can be attributed to its longer long axis, which affords the largest distance among the monomers to delocalize charge across. The third-order response of many of the monomers is on the same order as many other organic materials. For those with an appreciable response, the response is orientated along the molecular long axis.

Rationalization of γ_{avg} in these systems can be obtained by briefly considering the properties of the monomer first dipole-allowed ($\mu_{ge} > 3$ Debye) excited state. The first excited state energy sits high at an average of 3.76 eV, with DMQtT the lowest at 2.57 eV and TCNE (from Py/TCNE) the highest at 5.21 eV. The average of the transition dipole moments (μ_{ge}) is moderate at 6.1 Debye, with DBTTF possessing the smallest at 3.5 Debye and DMQtT possessing the largest at 12.1 Debye; in the case of DMQtT, the long-axis component dominates the transition dipole moment. Due to high degrees of symmetry, the ground-state state dipole moments are zero for all monomers except for the monomers of TTF-CA LT, leading changes in state dipole moments ($\Delta\mu_{eg}$) to be 0. The individual monomers of TTF-CA LT have non-zero ground-state dipole moments due to the lowered symmetry of the crystal at lower temperature.[15] We note that our results for pyrene are consistent in sign and magnitude with previous finite-field calculations,[25] and consistent with experimental measurements of TCNE and TCNQ which showed values of γ on the order of 10^{-36} esu.[26] Comparison of the long-axis component of DMQtT to previous work at the MRDCI level shows that the B3LYP-derived excited-state properties lead to an overestimation of γ by nearly 100, due to differences in excited state energies (3.06 eV *vs.* 2.88 eV, for MRDCI and B3LYP, respectively).[27-28]

6.3.2. Third-Order Optical Response of CT Complexes

6.3.2.1. Physical Properties

The physical parameters of the CT complex dyad configurations, as obtained from the experimental unit cell, are collected in Table 6.2. To characterize the various dyad

configurations, we consider three geometric parameters: the intermolecular distance, measured as the distance between the center-of-mass centroid of the donor and acceptor; the intermolecular angle, the angle between the center-of-mass centroid of a terminal aromatic ring on the donor, the center-of-mass centroid of the whole donor, and the center-of-mass centroid of the acceptor; and the angle made between the plane containing the donor and the plane containing the acceptor. The intermolecular angle serves as a measure of displacement between the donor and acceptor; for large angles (*e.g.*, 90°) the displacement is small, while smaller angles lead to a larger amount of displacement between the donor and acceptor molecules.

The physical parameters among the dyads studied here are varied. DMQtT-F_4TCNQ and Py-TCNQ are the opposite extremes among the physical parameters of the dyads: the intermolecular distance between the center-of-mass centroids of the donor and acceptor molecules is largest for DMQtT-F_4TCNQ (5.09 Å) and shortest for Py-TCNQ (3.57 Å), while the intermolecular angle is the smallest for DMQtT-F_4TCNQ (40.59°) and largest for Py-TCNQ (77.12°). DMQtT-F_4TCNQ possesses the largest ground-state dipole moment (8.77 D) and largest amount of electron transfer (0.36 |e|), while Py-TCNQ possess the smallest ground-state dipole moment at 1.94 D with 0.11 |e| transferred. The physical parameters of the selected complexes thus span a wide range. The amount of charge transferred between the donor and acceptor correlates with a variety of observed properties of the CT complexes, particularly for electrical transport.[29]

Table 6.2: Physical parameters of the CT complex dyad configurations. The intermolecular distances are measured between the centroids of the donor and acceptor; the intermolecular angles are defined as the angle between the centroid of a terminal aromatic ring on the donor, the centroid of the donor, and the centroid of the acceptor; the angles between planes are the angle between the plane of the donor and plane of the acceptor. The ground-state dipole moment and charge transferred were obtained at the B3LYP/6-31G level of theory.

Complex	Intermolecular distance (Å)	Intermolecular angle (°)	Angle between planes (°)	Ground-state dipole moment (D)	Charge transferred (|e|)
DMQtT-F_4TCNQ	5.09	40.59	2.17	8.77	0.36
TTF-CA LT	3.69	72.46	1.02	5.02	0.28
DBTTF-TCNQ	4.61	48.67	4.38	4.54	0.21
TTF-CA HT	3.62	72.39	1.55	3.87	0.22
Pe-TCNE	4.12	51.34	1.80	3.29	0.17
Py-TCNE	3.99	54.50	3.41	2.23	0.12
Py-TCNQ	3.57	77.12	6.86	1.94	0.11

6.3.2.2. Dyad Configurations of D-A Units

We take the CT complex exhibiting the strongest interaction, DMQtT-F_4TCNQ, as a representative example and discuss in detail its electronic structure, excited-state properties, and γ_{avg} before turning to the general trends among the remaining CT complexes. The electronic structure and excited-state properties are broadly similar among the compounds investigated. As discussed in the Introduction, the highly polarizable nature and large negative γ_{avg} of the ground state in cyanines can be attributed to the cyanine being in a geometry defined by two main resonance forms. It will be shown that the origin of the third-order response in CT complexes is different from the origin of the third-order response in cyanines.

As can be expected for the frontier orbitals of a compound with pronounced CT character, the HOMO resides on the donor molecule and the LUMO resides on the acceptor molecule (Figure 6.5). The remaining orbitals alternate being localized on the donor or acceptor molecule. In cyanines, the excitations describing the lowest two excited states involve excitations among the HOMO-1, HOMO, LUMO, and LUMO+1 orbitals. Likewise, the excitations describing the lowest CT complexes excited states involve the same orbitals, plus a lower lying occupied orbital (typically HOMO-2, as in the case of DMQtT-F_4TCNQ). Among the five lowest excited states, there are three types of excitations: a charge transfer $\mathrm{HOMO} \rightarrow \mathrm{LUMO}$ excitation, a local excitation centered on the donor molecule (here DMQtT) ($\mathrm{HOMO} \rightarrow \mathrm{LUMO} + 1$ and $\mathrm{HOMO} - 1 \rightarrow \mathrm{LUMO} + 1$), and a local excitation centered on the acceptor molecule (here F_4TCNQ) ($\mathrm{HOMO} - 2 \rightarrow \mathrm{LUMO}$). This in turn gives rise to excited states that are either local excitation in character or CT in character.

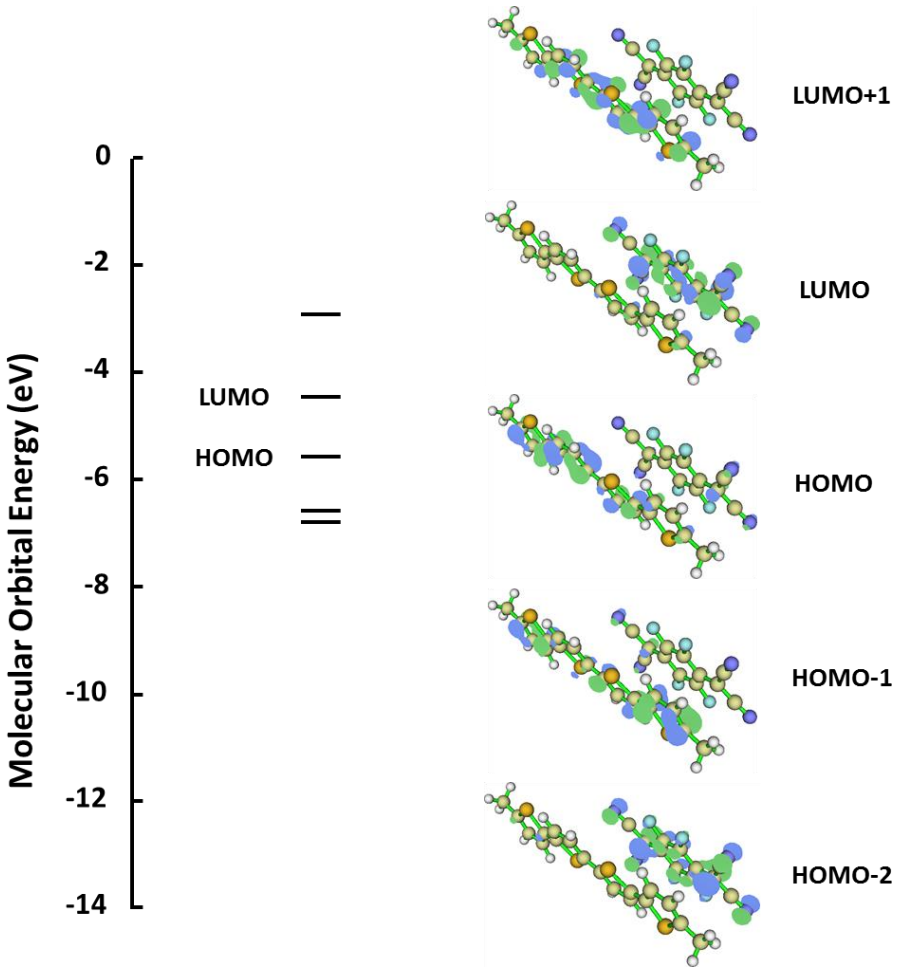

Figure 6.5: Molecular orbital energies (left) and illustration of the frontier molecular orbitals (right) for DMQtT-F_4TCNQ at the B3LYP/6-31G level.

The excited-state situation is different in the CT complexes compared to cyanines. The CT nature of the intermolecular interaction affords many low-lying excited states; for DMQtT-F4TCNQ, there are 11 excited states whose energies are equal to or less than 3 eV. However, due to the CT nature of many of these states, they are not significantly dipole-coupled to the ground state. Indeed, for the 50 lowest excited states in DMQtT-F_4TCNQ, only 6 have μ_{ge} > 3 Debye (Table 6.3), while the remaining states have small transition dipole moments (0 – 2 Debye). For DMQtT-F_4TCNQ the first excited state is low in energy

and is moderately dipole-coupled to the ground state. The remaining excited states which are coupled to the ground state have moderate transition dipole moments (3 – 4 Debye). For excited states that are CT in character, the *x*-component of the transition dipole moment, which corresponds to the CT direction, provides the largest contribution to the magnitude of μ_{ge}. For excited states with local character, however, the *y*-component is largest. In general, the combination of low excited-state energies and at least moderate transition dipole moment are favorable properties to promote a large magnitude of γ.

Table 6.3: State energies, transition dipole moments, change in state dipole moments (total change), and CI composition for all excited states of DMQtT-F_4TCNQ with $\mu_{ge} > 3$ Debye within the first 50 states as calculated at the B3LYP/6-31G level.

Excited State	Energy (eV)	$\boldsymbol{\mu_{ge}}$ (Debye)	$\boldsymbol{\Delta\mu_{eg}}$ (magnitude) (Debye)	CI Composition
1	1.07	$6.53x + 3.27y + 1.28z$	$-25.96x - 6.73y - 2.61z$ **(26.48)**	$+0.73\|H \rightarrow L\rangle$
2	1.82	$0.39x - 2.90y - 1.10z$	$-9.08x - 8.29y - 3.37z$ **(12.70)**	$+0.67\|H - 1 \rightarrow L\rangle$
5	2.62	$-11.77x + 2.09y + 0.42z$	$-6.22x - 0.57y + 0.35y$ (**5.64**)	$-0.37\|H - 2 \rightarrow L\rangle$ $+0.52\|H \rightarrow L + 1\rangle$
7	2.69	$-3.94x + 0.95y + 0.29z$	$+2.69x - 9.86y - 4.86z$ **(8.04)**	$+0.58\|H - 6 \rightarrow L\rangle$
11	3.21	$3.05x - 0.30y - 0.11z$	$+6.18x + 2.76y - 1.14z$ **(-6.33)**	$+0.52\|H - 1 \rightarrow L + 1\rangle$ $+0.42\|H \rightarrow L + 2\rangle$
14	3.78	$4.49x - 0.77y + 0.30z$	$-17.17x - 6.31y - 2.38z$ **(18.23)**	$+0.55\|H \rightarrow L + 3\rangle$

Due to the lack of symmetry in the D-A dyad, S_1 can have a strong TPA response. Additionally, the few excited states that are dipole coupled to the ground state are in turn strongly coupled to many other excited states ($\mu_{ee'}$ > 4 Debye). S_1 is coupled to 7 excited

states, S_2 to 8, and S_5 to 10, while S_{14} is only coupled to 3. Similar to the contributions to μ_{ge}, the *x*-component is the largest contributor to $\mu_{ee'}$, and in many excited states is effectively the single contributor. These observations suggest that significant TPA can occur the dyad configuration, and with their low first excited-state energy, their use in AOS applications at telecommunications wavelengths (0.8 – 0.95 eV) is potentially limited.

In molecular systems such as cyanines that maintain C_{2v} symmetry, the differences between the ground state and OPA state dipole moments ($\Delta\mu_{eg}$) are vanishingly small: a promotion of an electron from HOMO to LUMO simply shifts electron density from the odd-numbered to the even-numbered carbon atoms without altering much the backbone geometry due to the nodal pattern of the cyanine frontier MOs. In contrast to the situation in cyanines, in the CT complexes a $\mathrm{HOMO} \rightarrow \mathrm{LUMO}$ transition moves an electron from an occupied orbital on the donor molecule to an unoccupied orbital on the acceptor molecule, which results in a significant difference between state dipole moments. In DMQtT-F_4TCNQ, the magnitude of $\Delta\mu_{eg}$ for the first excited state is 26.5 Debye and 12.7 Debye for the second excited state. The *x*-component of $\Delta\mu_{eg}$ has the largest change in magnitude. Additionally, the change in magnitude of the *y*-component for most states is moderate; as the monomers in the dyad configuration are not in a face-on geometry rather but in a slipped geometry from one another, we should expect changes of $\Delta\mu_{eg}$ to be mostly between the *x*- and *y*- components.

Table 6.4: γ and its decomposition into axial and three-state terms for DMQtT-F_4TCNQ, reported in 10^{-36} esu.

	$\boldsymbol{\gamma}$ **x10^3**	**D x10^3**	**T x10^3**	**N x10^3**
xxxx	114	133	18.4	-37.7
yyyy	2.72	2.79	1.13	-1.20
zzzz	0.0775	0.0645	0.0370	-0.0240
avg.	29.4	36.0	2.49	-9.09

γ_{avg} for DMQtT-F_4TCNQ is positive and significantly enhanced over the individual monomers composing the complex (Table 6.4). As anticipated by the discussion on the state and transition dipole moments, the γ_{xxxx} tensor dominates γ. γ_{yyyy} and γ_{zzzz} are several orders of magnitude smaller, suggesting that the individual monomer response does not appreciably contribute to γ. To rationalize the sign and magnitude of γ, we consider the simplified three-term model. We recall that in this equation, each term contains a factor of μ_{ge}^2 in the numerator and each denominator is composed of E_{ge}^3 ($E_{ge}^2 E_{ee'}$ in the case of the **T** term). The **D** term, which has an additional dependence on $\Delta\mu_{eg}$ in the numerator, dominates the three-term decomposition for DMQtT-F_4TCNQ, since the states that are significantly coupled to the ground state have large changes in their state dipole moments upon excitation. While the many couplings among excited states in DMQtT-F_4TCNQ with large transition dipole moments should lead to a large **T** term (in which there is also a dependence on $\mu_{ee'}$ in the numerator), the larger excited-state energies (> 3 eV) which enter into the expression lead to larger denominators which decrease the magnitude of the **T** term. As the **T** and **N** terms are of similar magnitudes but opposite sign, the **N** term is partially cancelled by the **T** term; the remainder of the **N** term decreases the magnitude of the **D** term. γ is thus attributable to the **D** term through the significant changes in state

dipole moments. The earlier implication that DMQtT-F_4TCNQ has significant TPA is further strengthened by examining the TPA cross-sections for several of the lowest excited states. The TPA cross-section of S_1 is 804 GM, while both S_2 and S_3 have TPA cross-sections of ~5,000 GM, indicating that these states are strongly TPA. The TPA cross-sections of S_4 and S_5 are 470 and 680 GM, respectively. It is anticipated that S_1 in the centrosymmetric triad configurations will not be TPA active due to symmetry considerations.

Having discussed in detail the NLO properties and response of DMQtT-F_4TCNQ, we now turn our attention to the complete series of CT complexes. The first 5 lowest excited states and transition dipole moments are collected in Table 6.5, in which the first several excited states are low lying (< 3 eV) and have moderate μ_{ge}. The energies of the first excited states (S_1) are similar with respect to one another (~1 – 1.4 eV). There are many low-lying excited states below 3 eV, but only a handful of states are strongly dipole-coupled ($\mu_{ge} > 3$ Debye) to the ground state. These excited states which are strongly coupled to the ground state are in turn coupled to many more excited states. TTF-CA HT and LT have the least number of excited states coupled to the ground state (2 and 1, respectively), and subsequently have the fewest couplings between excited states.

Table 6.5: Excited-state energies in E_n (eV), transition dipole moments μ_{0n} (Debye), and difference in state dipole moments $\Delta\mu_{n0}$ (Debye) among the 5 lowest excited states for the series of CT complexes at the B3LYP/6-31G level. Complexes are ranked in descending order by calculated amount of charge transferred in the ground state.

Complex	$\mathbf{E_1}$ $(\boldsymbol{\mu_{01}})$ $[\boldsymbol{\Delta\mu_{10}}]$	$\mathbf{E_2}$ $(\boldsymbol{\mu_{02}})$ $[\boldsymbol{\Delta\mu_{20}}]$	$\mathbf{E_3}$ $(\boldsymbol{\mu_{03}})$ $[\boldsymbol{\Delta\mu_{30}}]$	$\mathbf{E_4}$ $(\boldsymbol{\mu_{04}})$ $[\boldsymbol{\Delta\mu_{40}}]$	$\mathbf{E_5}$ $(\boldsymbol{\mu_{05}})$ $[\boldsymbol{\Delta\mu_{50}}]$
DMQtT-F_4TCNQ	1.07	1.82	2.39	2.53	2.62
	(7.41)	(3.12)	(1.64)	(0.87)	(11.9)
	[26.5]	[26.48]	[7.88]	[29.8]	[5.64]
TTF-CA LT	1.37	2.67	2.75	2.82	2.97
	(5.02)	(0.37)	(0.70)	(0.23)	(1.31)
	[12.4]	[-1.67]	[-1.60]	[-1.41]	[9.89]
DBTTF-TCNQ	1.08	2.31	2.34	2.54	2.82
	(5.76)	(2.88)	(0.56)	(0.61)	(6.53)
	[24.1]	[19.6]	[26.3]	[14.4]	[1.71]
TTF-CA HT	1.12	2.72	2.78	2.84	2.95
	(4.71)	(0.88)	(0.67)	(0.69)	(0.33)
	[14.6]	[5.26]	[1.22]	[3.67]	[-0.847]
Pe-TCNE	1.21	2.49	2.65	2.77	2.83
	(4.0)	(0.36)	(0.26)	(0.78)	(4.42)
	[18.9]	[18.6]	[18.5]	[17.4]	[5.89]
Py-TCNE	1.27	2.82	2.65	3.33	3.59
	(2.20)	(2.29)	(0.30)	(1.47)	(3.67)
	[6.13]	[18.4]	[18.2]	[16.9]	[6.13]
Py-TCNQ	0.97	1.68	2.39	2.75	3.03
	(3.06)	(0.71)	(0.78)	(4.81)	(5.25)
	[15.9]	[16.1]	[16.2]	[9.10]	[5.42]

Among the excited states with CT character, the largest component of μ_{ge} is the x-component. The magnitude of the transition dipole moment for S_1 is more varied than its excited-state energy among the complexes; with the exception of Py-TCNE, S_1 is coupled to the ground state ($\mu_{g1} > 3$ Debye). The trend in transition dipole moment magnitudes roughly correlates with the amount of charge transferred in the CT complex (*i.e.*, the more

charge transferred the larger μ_{ge} is). Due to the reduced symmetry of low temperature TTF-CA compared to its high temperature analog, the S_1 energy and μ_{g1} are both larger in TTF-CA LT. Large changes (~20 Debye) between the ground-state and excited-state state dipole moments are seen upon excitation to the first excited state (with the exception of Py-TCNE).

The excited-state properties of Py-TCNE differ from those complexes within the rest of the series. In Py-TCNE, the first several excited states are not strongly coupled to the ground state, possessing $\mu_{ge} <$ ~2 Debye. Subsequently, the first excited state with a transition dipole moment greater than 3 Debye is the fifth excited state (S_5). The energy of S_5 is at 3.59 eV, some 2.5 eV higher than S_1 energy (1.16 eV). The CI description of S_5 contains a HOMO → LUMO+1 transition, which corresponds to a local excitation on the donor molecule. Due to S_5 being a local excitation, $\Delta\mu_{eg}$ is comparatively small at ~6 Debye. As to be discussed shortly, the different excited-state properties of Py-TCNE lead to a substantially smaller response compared to the rest of the CT complexes.

The trends in γ broadly follow the trends in amount of charge transferred in the CT complex: the greater amount of charge transferred, the larger γ_{avg} is (Table 6.6). γ_{avg} for the CT complexes is greatly enhanced over the responses of the individual monomers; γ_{xxxx} largely determines γ_{avg}. The **D** term dominates the three-term expression, for the same reasons discussed previously in the case of DMQtT-F_4TCNQ. We note that γ_{avg} for DMQtT-F_4TCNQ and DBTTF-TCNQ is similar to γ_{avg} calculated for a polyene with 30 π-electrons;[30] however, since DMQtT-F_4TCNQ and DBTTF-TCNQ contain 38 and 48 π-electrons, respectively, this implies that the CT complexes are not as efficient as polyenes

at the same number of π-electrons. This further highlights that third-order response originates from the intermolecular interaction between the monomer units and does not scale with the number of π-electrons.

Table 6.6: Calculated γ_{avg} and its decomposition into axial tensors (top) and the three-state model (bottom) for CT complexes, reported in 10^{-36} esu. γ_{avg} repeated for both decompositions for ease of comparison. Complexes are ranked in descending order of calculated amount of charge transferred in the ground state.

complex	γ_{avg} **x10^3**	γ_{xxxx} **x10^3**	γ_{yyyy} **x10^3**	γ_{zzzz} **x10^3**
DMQtT-F_4TCNQ	29.4	114	2.72	0.0776
TTF-CA LT	1.68	1.65	1.65	0.329
DBTTF-TCNQ	10.1	19.9	5.29	0.0665
TTF-CA HT	3.58	3.42	3.39	0.530
Pe-TCNE	3.34	7.27	0.414	1.03
Py-TCNE	0.0368	0.138	6.79×10^{-4}	7.95×10^{-3}
Py-TCNQ	3.01	10.1	0.618	4.99×10^{-3}
complex	γ_{avg} **x10^3**	**D x10^3**	**T x10^3**	**N x10^3**
DMQtT-F_4TCNQ	29.4	36.0	2.49	-9.09
TTF-CA LT	1.68	1.72	0.249	-0.283
DBTTF-TCNQ	10.1	11.4	0.275	-1.67
TTF-CA HT	3.58	3.74	0.259	-0.418
Pe-TCNE	3.34	3.62	0.0303	-0.310
Py-TCNE	0.0368	9.12×10^{-3}	0.0375	-9.90×10^{-3}
Py-TCNQ	3.01	3.02	0.459	-0.471

The differences in γ between the CT complexes can be explained in light of the variations among their excited-state properties. While the first excited-state energies are within ~0.4 eV of one another, the transition dipole moments for the first coupled state vary by about 4 Debye from the weakest to the strongest transition. The sign and magnitude of the CT

complexes is determined by the **D** term, as the **T** and **N** terms largely cancel one another out. Differences between the **D** term among the CT complexes are primarily responsible for the different magnitudes of γ.

The larger energy of the first dipole-allowed excited state and corresponding smaller transition dipole moment in Py-TCNE leads to its smaller γ_{avg}. The **D** term is small and is cancelled by the **N** term. γ_{avg} is then determined by the **T** term; even though there are many couplings among excited states in Py-TCNE, the couplings are to comparatively energetic higher-lying excited states ($E_{e'} > \sim 4$ eV), so the larger denominators of the e' states reduce the magnitude of the **T** term.

Again, the asymmetry of the dyad configuration leads to TPA cross-sections for S_1 to be on the order of ~600-800 GM. In addition, several of the lowest excited states contain large TPA cross-sections. For DMQtT-F4TCNQ, DBTTF-TCNQ, Pe-TCNE, and TTF-CA LT, several of the low-lying excited states have moderate (100's GM) to significant (1,000's GM) TPA cross-sections. The low-lying states in Py-TCNE and Py-TCNQ are not strongly TPA.

6.3.2.3. Triad Configurations of D-A-D and A-D-A units

The previous section focused on dyads composed of one donor and one acceptor molecule, which were shown to undergo a substantial change between state dipole moments for excited states of CT excitation character. As stated in the introduction of this Chapter, crystals of the CT complexes are centrosymmetric, so $\Delta\mu_{eg} = 0$ should be zero by symmetry within the crystal environment. The dyad configuration is asymmetric with

respect to the crystal symmetry, and may lead to an artificially large $\Delta\mu_{eg}$, which enhances the **D** term to inflate γ. As we expect the CT state to delocalize over several units within the crystal and to gain a more detailed understanding of the physicality of a large **D** term and its impact on γ_{avg}, we now move to larger systems and investigate γ in centrosymmetric triad configurations composed of D-A-D or A-D-A units. We consider both configurations due to the triad asymmetry, as the number of D and A units is not equal. Within these configurations, $\Delta\mu_{eg}$ is 0 by symmetry. The triad configurations largely follow the trends established by the dyad configurations; the following discussion will briefly highlight the differences incurred by the addition of another donor or acceptor unit.

In the triad configurations, the HOMO and LUMO are now symmetrically on both donor (in the D-A-D configuration) and acceptor (in the A-D-A) molecules, respectively. Excitations now involve transitions from orbitals on both donor molecules to the acceptor (in the D-A-D configuration) or from the donor to both acceptors (in the A-D-A configuration). In many of the MOs, the electron density is distributed over one half of each repeated monomer but at opposite ends on each repeat monomer.

The addition of the third molecule introduces several pairs of degenerate excited states with energies. As we have doubled the number of donor or acceptor units within the triad, this doubles the number of donor or acceptor states and also introduces new degenerate CT states. These states come as linear combinations, with only one component of the transition dipole moment optically coupled to the ground state (with $\mu_{ge} < 1$ Debye for the states not optically coupled). The number of excited states coupled to the ground state is similar between dyad and triad configurations. Importantly, while the x-component of the transition dipole moment is still the largest in magnitude, it no longer solely dominates μ_{ge}.

In some excited states, the y-component approaches the x-component in magnitude. As the frontier orbitals are partially distributed across both repeat molecules within the triad configuration, moving from the occupied orbital to the unoccupied orbital involves a transition not only along the x-coordinate but also along the y-coordinate.

Table 6.7: Normalized γ and its decomposition for triads of CT complexes in donor-acceptor-donor (D-A-D) and acceptor-donor-acceptor (A-D-A) configurations, reported in 10^{-36} esu. CT complexes ranked in descending order of amount of charge transferred.

complex	γ_{avg} **x10^3**	γ_{xxxx} **x10^3**	γ_{yyyy} **x10^3**	γ_{zzzz} **x10^3**	**D x10^3**	**T x10^3**	**N x10^3**
			D-A-D				
DMQtT-F_4TCNQ	35.0	150	1.84	1.73 x10^{-4}	0.00	54	-18.8
TTF-CALT	7.05	30.1	0.236	0.0286	8.20	0.575	-1.71
DBTTF-TCNQ	12.5	59.5	0.166	2.41 x10^{-4}	0.00	15.3	-2.81
TTF-CAHT	5.15	24.6	-0.00725	-1.96 x10^{-3}	0.00	6.55	-1.43
Pe-TCNE	2.81	13.2	0.0895	2.59 x10^{-3}	0.00	3.31	-0.505
Py-TCNE	0.745	3.67	-2.68x10^{-5}	-0.00535	0.00	0.845	-0.0995
Py-TCNQ	2.22	10.4	3.64x10^{-3}	-0.00860	0.00	2.50	-0.287
			A-D-A				
DMQtT-F_4TCNQ	19.8	99.5	-0.121	1.33 x10^{-3}	0.00	28.4	-8.55
TTF-CALT	7.70	33.9	0.133	0.0420	8.90	0.444	-1.67
DBTTF-TCNQ	9.75	49.9	-0.134	1.55 x10^{-4}	0.00	13.6	-3.59
TTF-CAHT	5.50	25.9	0.965 x10^{-3}	4.47 x10^{-3}	0.00	6.75	-1.31
Pe-TCNE	2.66	12.9	0.0625	-1.72 x10^{-3}	0.00	3.12	-0.457
Py-TCNE	0.143	0.685	-3.57 x10^{-3}	4.79 x10^{-4}	0.00	0.149	-0.00
Py-TCNQ	1.64	8.05	4.17 x10^{-3}	-0.163	0.00	2.19	-05620

The normalized values for the triads are presented in Table 6.7. To account for the doubling in size by the addition of a second donor or acceptor molecules, we normalize by dividing the triad γ_{avg} by 2. γ continues to correlate with the amount of charge transferred and the tensor corresponding to the CT direction (γ_{xxxx}) dominates the response, and the trends ordering of the response follows those established by the dyads. This normalized γ_{avg} still leads to an enhancement over the dyads; for Pe-TCNE and Py-TCNE, γ_{avg} is closer to the experimentally-measured value. This suggests the need to look at larger clusters in order to obtain a more quantitative result with experiment.

Importantly, while in the dyads the **D** term was responsible for γ, in the triads the **T** term is responsible. The **D** term is 0 due to the triad symmetry, and the magnitude of γ is now determined by the relative magnitudes of the **T** and **N** terms. The exception is TTF-CA LT, where the **D** term is non-zero due to the reduced symmetry of the crystal at the lower temperature and is responsible for γ.

There are several couplings among the excited states that possess large excited-state transition dipole moments, leading to the **T** term being larger than the **N** term. Of the triads, DMQtT-F_4TCNQ has a significant number of couplings among the excited states, particularly for the D-A-D triad, leading to a large **T** term. In this centrosymmetric configuration, this suggests significant TPA. The relative differences in γ values between the D-A-D and A-D-A triads can be rationalized in light of the differences in their excited-state properties: the smaller excited-state energies and larger transition dipole moments of the D-A-D configurations lead to a larger γ compared to the A-D-A configuration. Furthermore in the triads, there are many degenerate states with large TPA cross-sections

(δ_{2P}), particularly at higher excited states which are double in energy of the lower excited states (see **Table 6.8**). In all cases, the first excited state is an OPA state.

Table 6.8: Excited state number (#), energy (eV), and TPA cross-section δ_{TPA} (GM) for the several states with the largest δ_{TPA}. The first excited state is included for comparison.

complex	# (eV) [δ_{TPA}]	# (eV) [δ_{TPA}]	# (eV) [δ_{TPA}]	# (eV) [δ_{TPA}]
D-A-D				
DMQtT-F_4TCNQ	1 (0.96) [0.0]	2 (1.19) [4940]	5 (1.95) [858000]	
TTF-CA LT	1 (0.87) [0.0]	2 (1.37) [769]		
DBTTF-TCNQ	1 (1.01) [0.0]	2 (1.20) [1320]	4 (2.45) [2070]	
TTF-CA HT	1 (0.98) [0.0]	2 (1.23) [749]		
Pe-TCNE	1 (1.27) [0.0]	2 (1.45) [449]	4 (2.73) [218]	6 (2.76) [554]
Py-TCNE	1 (1.47) [0.0]	6 (2.91) [2130]	10 (3.54) [154]	
Py-TCNQ	1 (1.04) [0.0]	2 (1.10) [120]		
A-D-A				
DMQtT-F_4TCNQ	1 (1.11) [0.0]	2 (1.26) [2250]	3 (1.68) [1290]	6 (2.028) [6010]
TTF-CA LT	1 (0.83) [0.0]	2 (1.33) [789]		
DBTTF-TCNQ	1 (1.06) [0.0]	2 (1.23) [1140]	3 (2.06) [4570]	5 (2.33) [6370]
TTF-CA HT	1 (0.95) [0.0]	2 (1.18) [694]	3 (2.56) [194]	
Pe-TCNE	1 (1.31) [0.0]	3 (2.54) [4010]	7 (2.83) [1820]	10 (3.08) [1060]
Py-TCNE	1 (1.37) [0.0]	12 (3.95) [206]	24 (4.88) [4040]	
Py-TCNQ	1 (1.08) [0.0]	2 (1.15) [110]	7 (2.16) [104]	

6.3.2.4. Parallel Stacks of D-A Dyads

We consider a parallel stack of D-A dyads to investigate if in the four molecule configuration any interchain interactions impact γ. Non-centrosymmetric configurations composed of two parallel D-A dyads follow similar trends in excited-state energies, transition dipole moments, and state dipole moments to those discussed for the dyad and

triad configurations. We briefly focus in this section on DBTTF-TCNQ, as this complex was demonstrated to have one of the largest γ at the previous configurations.

As seen in the case of the triads, the addition of a parallel stack introduces several low-lying degenerate states as compared to the dyad configuration. Similarly, only a few of these excited states are coupled to the ground state. The largest components of the transition dipole moments are along the CT direction, and analogously to the triad configurations, some of the other components in the transition dipole moment can be large due to orbitals being localized on the different parts of the molecules within the stack. Compared to the dyad configurations, the first few excited states coupled to the ground state possess similar excited-state energies but larger transition dipole moments. Since the parallel stacks configurations consist of D-A dyads, a large change between state dipole moments occurs for the CT excitations.

We can understand the third-order response of the parallel stacks configurations in light of the discussion of the dyad and triad configurations. γ is on the order of 10^{-33} esu (Table 6.9), similar in magnitude to γ in the previous sections. At this configuration, the **D** term is large. Although there are a large number of couplings among the excited states with large excited-state transition dipole moments (6–10 Debye in magnitude), the larger excited state energies reduce the magnitude of the **T** term. Again for these two complexes, there are several excited-states with large TPA cross-sections in this configuration.

Table 6.9: Normalized γ_{avg} and its decomposition for DBTTF-TCNQ in a parallel stack of donor and acceptor molecules, reported in 10^{-36} esu.

complex	γ_{avg} x10^3	γ_{xxxx} x10^3	γ_{yyyy} x10^3	γ_{zzzz} x10^3	D x10^3	T x10^3	N x10^3
DBTTF-TCNQ	9.2	17.9	4.39	0.367	10.3	0.96	-2.08

We normalize γ_{avg} by dividing by 2 to compare to the dyad configuration. The normalized values for the parallel stacks configuration are essentially the same as in the dyad configuration (recall that for DBTTF-TCNQ γ_{avg} = 10.1 x10^{-33} esu and γ_{xxxx} = 19.9 x10^{-33} esu in the dyad). The total response can be considered as the sum of the two dyad configurations, and thus interactions between stacks do not contribute to the third-order response, an observation further supported by the small values for the γ_{yyyy} and γ_{zzzz} tensors.

6.4 Conclusions

In this Chapter, we have focused on understanding the sign and magnitude of seven CT complexes. We have investigated the third-order response of the CT complexes at four configurations: the individual monomers comprising the CT complex, a dyad consisting of one D-A unit, triads consisting of D-A-D and A-D-A units, and a parallel stack configuration composed of two D-A dyads in non-centrosymmetric configurations. With the exception of DMQtT, the monomers of the CT complexes do not show a calculated γ_{avg} larger than 10^{-36} esu. The significant enhancement of γ_{avg} (to the order of 10^{-33} esu) in the CT complexes in the dyad, triad, and parallel stack configurations is thus attributable

to the intermolecular interactions between the D and A units, and not due to the intrinsic third-order response of the individual monomers themselves. γ_{avg} is correlated to the amount of charge transferred in the CT complex, with larger calculated γ_{avg} demonstrated by complexes with a greater amount of charge transfer.

The CT interaction between the D and A units affords a long molecular axis, and many of the transition dipole moments are dominated by the component pointing along the CT direction. Thus, the third-order response is strongly anisotropic, with γ_{avg} being determined by the γ_{xxxx} tensor. The molecular properties of the CT complexes, in particular the moderate magnitudes of the transition dipole moments and the low excited-state energies of the CT states, are favorable to promote a large γ_{avg}. γ_{avg} is rationalized in the dyad configuration by the presence of large changes between state dipole moments due to the asymmetry of the D-A configuration, which leads to the **D** term dominating the three-term model. For the configurations consisting of triads of D-A-D and A-D-A units, the **D** term is negligible and the **T** term is responsible for the sign and magnitude of γ_{avg}, due to the many couplings among the excited states with large excited-state transition dipole moments. Interchain interactions do not contribute to the total response. In general, the many low-lying degenerate states and many strong couplings among the excited states suggest that these complexes are strongly TPA, especially DMQtT-F4TCNQ and DBTTF-TCNQ that present the largest calculated γ_{avg} values, greater than those of the experimentally-measured complexes.

6.5. References

1. Meyers, F.; Marder, S. R.; Pierce, B. M.; Bredas, J. L. Electric field modulated nonlinear optical properties of donor-acceptor polyenes: Sum-over-states investigation of the relationship between molecular polarizabilites and bond length alternation. *J. Am. Chem. Soc.* **1994,** *116*, 10703-10714.

2. Marder, S. R.; Perry, J. W.; Bourhill, G.; Gorman, C. B.; Tiemann, B. G.; Mansour, K. Relation between bond-length alternation and second electronic hyperpolarizability of conjugated organic molecules. *Science* **1993,** *261*, 186-189.

3. Wernke, W.; Pfeiffer, M.; Johr, T.; Lau, A.; Grahn, W.; Johannes, H.-H.; Dahne, L. Increase and saturation of the third order hyperpolarizabilities in homologous series of symmetric cyanines *Chem. Phys.* **1997,** *216*, 337-347.

4. Mukhopadhyay, S.; Risko, C.; Marder, S. R.; Brédas, J.-L. Polymethine dyes for all-optical switching applications: a quantum-chemical characterization of counter-ion and aggregation effects on the third-order nonlinear optical response. *Chem. Sci.* **2012,** *3*, 3103-3112.

5. Gieseking, R. L.; Mukhopadhyay, S.; Risko, C.; Brédas, J.-L. Impact of the nature of the excited-state transition dipole moments on the third-order nonlinear optical response of polymethine dyes for all-optical switching applications. *ACS Photonics* **2014,** *1*, 261-269.

6. Marder, S. R.; Gorman, C. B.; Meyers, F.; Perry, J. W.; Bourhill, G.; Bredas, J. L.; Pierce, B. M. A unified description of linear and nonlinear polarization in organic polymethine dyes. *Science* **1994,** *265*, 632-635.

7. Horiuchi, S.; Hasegawa, T.; Tokura, Y. Molecular donor-acceptor compounds as prospective organic electronics materials. *J. Phys. Soc. Jpn.* **2006,** *75*, 051016-051029.

8. Hasegawa, T.; Takeya, J. *J. Sci. Technol. Adv. Mater.* **2009,** *10*.

9. Gotoh, T.; Kondoh, T.; Egawa, K. Exceptionally large third-order optical nonlinearity of the organic charge-transfer complex. *J. Opt. Soc. Am. B* **1989,** *6*, 703-706.

10. Gong, Q.; Xia, Z.; Zou, Y. H.; Meng, X.; Wei, L.; Li, F. Large nonresonant third-order hyperpolarizabilities of organic charge-transfer complexes. *Appl. Phys. Lett.* **1991,** *59*, 381-383.

11. Emge, T. J.; Wiygul, F. M.; Chappell, J. S.; Bloch, A. N.; Ferraris, J. P.; Cowan, D. O.; Kistenmacher, T. J. Crystal structures for the electron donor dibenzotetrathiafulavalene, DBTTF, and its mixed-stack charge-transfer salts with the electron acceptors 7,7,8,8-tetracyano-p-quinodimethane, TCNQ, and 2,5-difluoro-7,7,8,8-tetracyano-p-

quinodimethane, 2,5-TCNQF2. *Molecular Crystals and Liquid Crystals* **1982,** *87*, 137-161.

12. Hotta, S.; Kobayashi, H. *Synth. Met.* **1994,** *66*, 117.

13. Ikemoto, I.; Yakushi, K.; HKuroda, H. The refinement of the crystal structure of the perylene-tetracyanoethylene complex. *Acta Crystallographica, Section B: Struct. Crystallogr. Cryst. Chem.* **1970,** *26*, 800.

14. Ikemoto, I.; Kuroda, H. The refinement of the crystal structure of the pyrene-tetracyanoethylene complex. *Acta Crystallographica, Section B: Struct. Crystallogr. Cryst. Chem.* **1968,** *24*, 383.

15. García, P.; Dahaoui, S.; Katan, C.; Souhassou, M.; Lecomte, C. On the accurate estimation of intermolecular interactions and charge transfer: the case of TTF-CA. *Faraday Discuss.* **2007,** *135*, 217-235.

16. Prout, C. K.; Tickle, I. J.; Wright, J. D. Molecular complexes. Part XVI. Crystal structure of 1:1 molecular complex of pyrene and 7,7,8,8-tetracyanoquinodimethane. *J. Chem. Soc., Perkin Trans. 2* **1973,** *48*, 528-530.

17. Sakai, M.; Sakuma, H.; Ito, Y.; Saito, A.; Nakamura, M.; Kudo, K. Ambipolar field-effect transistor characteristics of (bedt-ttf)-(tcnq) crystals and metal-like conduction induced by a gate electric field. *Phys. Rev. B* **2007,** *76*, 045111-045115.

18. Takahashi, Y.; Hasegawa, T.; Abe, Y.; Tokura, Y.; Saito, G. Organic metal electrodes for controlled p- and n-type carrier injections in organic field-effect transistors. *Appl. Phys. Lett.* **2006,** *88*, 073504-073506.

19. Takahashi, Y.; Hasegawa, T.; Abe, Y.; Tokura, Y.; Nishimura, K.; Saito, G. tuning of electron injections for n-type organic transistor based on charge-transfer compounds. *Appl. Phys. Lett.* **2005,** *86*, 063504-063506.

20. Zhu, L.; Yi, Y.; Li, Y.; Kim, E.-G.; Coropceanu, V.; Bredas, J. L. Prediction of remarkable ambipolar charge-transport characteristics in organic mixed-stack charge-transfer crystals. *J. Am. Chem. Soc.* **2012,** *134*, 2340-2347.

21. Lee, C.; Yang, W.; Parr, R. G., Development of the colle-salvetti correlation-energy formula into a functional of the electron density. *Phys. Rev. B* **1988,** *37*, 785-789.

22. Becke, A. D. Density-functional thermochemistry III: The role of exact exchange. *J. Chem. Phys.* **1993,** *98*, 5648-5652.

23. Gaussian 09, Revision D.01, M. J. Frisch, G. W. Trucks, H. B. Schlegel, G. E. Scuseria, M. A. Robb, J. R. Cheeseman, G. Scalmani, V. Barone, B. Mennucci, G. A. Petersson, H. Nakatsuji, M. Caricato, X. Li, H. P. Hratchian, A. F. Izmaylov, J. Bloino, G. Zheng, J. L.

Sonnenberg, M. Hada, M. Ehara, K. Toyota, R. Fukuda, J. Hasegawa, M. Ishida, T. Nakajima, Y. Honda, O. Kitao, H. Nakai, T. Vreven, J. A. Montgomery, Jr., J. E. Peralta, F. Ogliaro, M. Bearpark, J. J. Heyd, E. Brothers, K. N. Kudin, V. N. Staroverov, T. Keith, R. Kobayashi, J. Normand, K. Raghavachari, A. Rendell, J. C. Burant, S. S. Iyengar, J. Tomasi, M. Cossi, N. Rega, J. M. Millam, M. Klene, J. E. Knox, J. B. Cross, V. Bakken, C. Adamo, J. Jaramillo, R. Gomperts, R. E. Stratmann, O. Yazyev, A. J. Austin, R. Cammi, C. Pomelli, J. W. Ochterski, R. L. Martin, K. Morokuma, V. G. Zakrzewski, G. A. Voth, P. Salvador, J. J. Dannenberg, S. Dapprich, A. D. Daniels, O. Farkas, J. B. Foresman, J. V. Ortiz, J. Cioslowski, and D. J. Fox, Gaussian, Inc., Wallingford CT, 2013.

24. Lu, T.; Chen, F. Multiwfn: A multifunctional wavefunction analyzer. *J. Comp. Chem.* **2012**, *33,* 580-592.

25. Matsuzawas, N.; Dixon, D. A. Semiempirical calculations of the polarizability and second-order hyperpolarizability of C60, C70, and model aromatic compounds. *J. Phys. Chem.* **1992**, *96*, 6241-6247.

26. Nalwa, H. S. Organic materials for third-order nonlinear optics. *Adv. Mater.* **1993**, *5*, 341-358.

27. Beljonne, D.; Shuai, Z.; Bredas, J. L. Theoretical study of thiophene oligomers: Electronic excitations, relaxation energies, and nonlinear optical properties. *J. Chem. Phys.* **1993**, *98,* 8819-8826.

28. Beljonne, D.; Shuai, Z.; Bredas, J. L. Theoretical evolution of the third-order molecular polarizabilities as a function of chain length in thiophene and pyrrole oligomers. *Int. J. Quan. Chem.* **1994**, *52,* 39-48.

29. Goetz, K. P.; Vermeulen, D.; Payne, M. E.; Kloc, C.; McNeil, L. E.; Jurchescu, O. D. Charge-transfer complexes: new perspectives on an old class of compounds. *J. Mater. Chem. C* **2014**, *2*, 3065-3076.

30. Shuai, Z.; Bredas, J. L., Static and dynamic optical nonlinearities in conjugated polymers: Third-harmonic generation and the dc Kerr effect in polyacetylene, polyparaphenylene vinylene, and polythienylene vinylene. *Phys. Rev. B* **1992**, *46,* 4395-4404.

CHAPTER 7

CONCLUSIONS AND OUTLOOK

7.1. Conclusions

All-optical switching (AOS) has the potential to realize the faster switching speeds demanded by an ever-increasing amount of data transmission, particularly as greater numbers of users integrate the Internet more into their daily lives and rely on it for their entertainment needs. One of the challenges to overcome before AOS devices see widespread adoption is the paucity of suitable materials. Linear π-conjugated organic materials, particularly cyanine-like polymethines, have shown to date the greatest promise; however, intermolecular cyanine-cyanine and cyanine-counterion interactions must be limited to prevent substantial modification of the cyanine properties. In this Thesis, we have explored from a quantum-mechanics and molecular-dynamics standpoint promising molecular design strategies to minimize these deleterious intermolecular interactions. We have stressed how changes to molecular structure can impact the molecular properties critical for AOS and shown how modifications between cyanine and counterion structures can impact aggregation in the bulk. A running theme is the importance of minimizing cyanine-counterion interactions, and what effect the counterion or strategies to minimize it has on a cyanine.

Maintaining the promising isolated cyanine NLO properties at high chromophore number densities required for AOS devices is challenging due to cyanine-cyanine and cyanine-counterion interactions, which lead to aggregation and ion-pairing, respectively. We have

shown that thiopyryliums with a large, bulky, $Pd(PPh_3)_2Cl$ group in the molecular center containing out-of-plane substituents is effective at reducing overall aggregation compared to the unsubstituted thiopyrylium. Whereas the $Ni(PPh_3)_2Cl$ substituent modified the thiopyrylium backbone and introduced a new TPA state in the middle of the transparency window, the $Pd(PPh_3)_2Cl$ and $Pt(PPh_3)_2Cl$ substituents did not disturb the thiopyrylium backbone. In experimentally relevant cyanines designed to minimize aggregation, increasing the counterion size can aid in reducing the uncontrolled cyanine-cyanine aggregation, however, once a bulky cyanine is paired with a moderately bulky counterion, no further reduction in aggregate geometry reduction is gained by increasing the counterion size. The size of the counterion can impact the type of aggregation observed, limiting uncontrolled aggregation but also promoting aggregate configurations inherent to the specifics of the molecular geometry. Importantly, the size of the counterion determines how closely the counterion can approach the backbone and the degree of localization near the cyanine molecular end. Medium-sized counterions can occur at a broad range of positions along the cyanine backbone, suggesting that cyanines in the solid state exist in various degrees of symmetry-brokenness. These results underscore how molecular-dynamics simulations can aid in rationally choosing cyanines and counterions to control the extent of aggregation in thin films.

Having shown that counterions can occupy a broad range of positions along the cyanine backbone in thin films, we then investigated the potential energy surface and non-covalent interactions of streptocyanine/counterion (Cl^- and BF_4^-) complexes as a function of counterion displacement along the streptocyanine backbone. As expected, the degree of BLA as a function of increasing counterion displacement from the molecular center

evolves in a smooth fashion from cyanine-like to near polyene-like. However, we showed that between streptocyanines of different backbone lengths, the degree of BLA is similar at each counterion displacement. This evolution in BLA is different compared the evolution of BLA as a function of an applied uniform electric field. The counterion electric field is highly localized and non-uniform across the streptocyanine backbone, such that shorter streptocyanines experience a more asymmetric environment as the counterion is nearer to one molecular end than in a longer streptocyanine at the same displacement. The counterion electric field and intrinsic polarizability of the streptocyanines compensate one another, leading to the appearance of similar degrees of BLA at the same counterion displacement. We showed that the interaction between the streptocyanine and counterion is largely electrostatic in nature and is a local effect, and that the localization of the counterion near one molecular end of the streptocyanine is due to the increased localization of backbone charge which leads to a stronger electrostatic interaction. While increasing the backbone length does not impact the electrostatic interaction, it does lead to a reduction in the binding energy of the streptocyanine/counterion complex due to an increased energetic penalty from the backbone geometry distortions at the longer backbone lengths. Critically, when taking account of thermal energy at room temperature, the counterion can occupy a range of displacements, up to 1 Å closer to the molecular end and increasing with increasing counterion size, leading to a larger degree of BLA than expected from considering only the fully optimized geometries. These results stress that the interactions between counterion and cyanine can strongly modify the ground-state cyanine properties, and that these interactions must be controlled; our results underline that bulkier cyanines can lead to less strongly bound cyanine/counterion complexes.

One way to potentially control and mitigate cyanine-counterion interactions is to covalently tether the counterion to the cyanine backbone. We investigated zwitterionic cyanines for such a purpose, in which a substituent bearing a charge opposite to that on the backbone is attached to the molecular center of a thiopyrylium cyanine. We showed that the molecule must maintain a high degree of zwitterionic character to avoid charge recombination that leads to a modification of the ground-state charge distribution and electronic coupling between the substituent and backbone orbitals. This mixing between frontier orbitals leads to an increase of BLA and geometric distortions in the backbone, as well as to excited states that are not distinctly OPA or TPA and the loss of the transparency window. Strong electron acceptors are able to fully retain the anionic charge on the substituent, leading to a small energy difference between the LUMO of the isolated cationic backbone and the HOMO of the isolated anionic substituent, which is essential to minimize charge recombination and avoid coupling between the frontier molecular orbitals. This understanding that charge separation between the backbone and substituent must be favored electronically to maintain the unsubstituted thiopyrylium properties provides guidance for designing new cyanine-based materials for AOS applications.

Among linear π-conjugated organic molecules γ is largest in cyanines and increases with increasing cyanine backbone length. However, at a critical backbone length, cyanines undergo a symmetry-breaking transition and the inherent advantageous properties of cyanines for AOS are lost. Binary charge transfer (CT) complexes analogously have a long axis along which they stack and show large nonresonant γ without suffering from symmetry breaking. We examined the origin of the third-order response of mixed-stack binary CT complexes and showed that the strong directionality of the intermolecular charge transfer

interaction along the charge transfer axis between the donor and acceptor molecules is responsible for the enhancement of γ over the individual isolated molecules composing the CT complex. The magnitude of γ correlates with the amount of charge transferred in the ground state, with complexes exhibiting a greater amount of charge transfer displaying larger values of γ. After investigating the CT complexes for which experimental measures show a strong response, we identified two additional CT complexes that are predicted to have an even larger response.

7.2. Outlook

In this Thesis, we have investigated promising strategies for limiting cyanine-cyanine and cyanine-counterion interactions, however, a number of strategies remain unexplored. Our molecular-dynamics simulations focused on understanding the interplay between cyanine structure and increasing counterion size. Given the observation that counterion size can trigger and promote aggregation inherent to the cyanine molecular structure, further work is needed in understanding how much this interplay can be exploited to favor controlled aggregation in thin films. Although the counterions investigated here were of a roughly spherical geometry, this is only a limited sampling of the available counterions. Linear counterions such as CN^- or planar counterions based on benzene or proton sponges may trigger the inherent aggregation to a different extent. While ultimately the cyanine molecular structure is responsible for the type of aggregation observed, a more detailed understanding as a function of cyanine molecular structure is needed to understand the ability of the cyanines to self-assemble and the geometries obtained. This methodology can

be applied to areas of research such as that or more broadly to understand counterion positioning in systems where the cyanine is relatively immobilized (*e.g.*, affixed to a substrate) in order to design new cyanines.

A cyanine-counterion complex in a thin film is not in isolation, but rather is surrounded by many other cyanines and counterions. Although we have shown that the interaction between a counterion and streptocyanine is highly localized, a more complete picture of how a cyanine responds to its local environment can be obtained by considering the impact of multiple counterions or a counterion with multiple charges near a cyanine. Molecular-dynamics simulations can also be of use, by selecting a cyanine and its nearest counterion neighbors from a trajectory to run further quantum-mechanical calculations on. Understanding the binding energies and potential energy surfaces of more complex cyanines with different end groups or substitution patterns could provide a strategy for minimizing the interaction between cyanines and counterions in thin films.

A reoccurring message throughout this Thesis was that cyanines, by virtue of their molecular structure or environment, could exist in various degrees of symmetry-brokenness. In the example of zwitterionic cyanines, the identity of the central substituent electron acceptors can provide another route to control the degree of ground-state polarization, potentially as a strategy to design cyanines that are "on the edge," at the limit between symmetrical and symmetry-broken structures. Further work is needed to determine the shape of the potential energy surface as a function of substituent molecular structure and cyanine backbone to determine how closely a zwitterionic cyanine can approach the edge without thermal energy leading to a complete symmetry-broken situation (or visa versa, leading to a dynamic symmetry-breaking process). The degree of

coupling between the cyanine backbone and substituent can be tuned by the strength of the substituent electron acceptor, and for moderate electron acceptor strengths an investigation into the response of the molecular in an applied electric field could provide a deeper understanding of the dynamic symmetry-breaking process. Further work is needed to understand if such “on-the-edge” cyanines can transition between symmetric and symmetry-broken structures depending on their environment.